2009-2010 AIAA Foundation

Team Aircraft Design Competition

-Proposal-

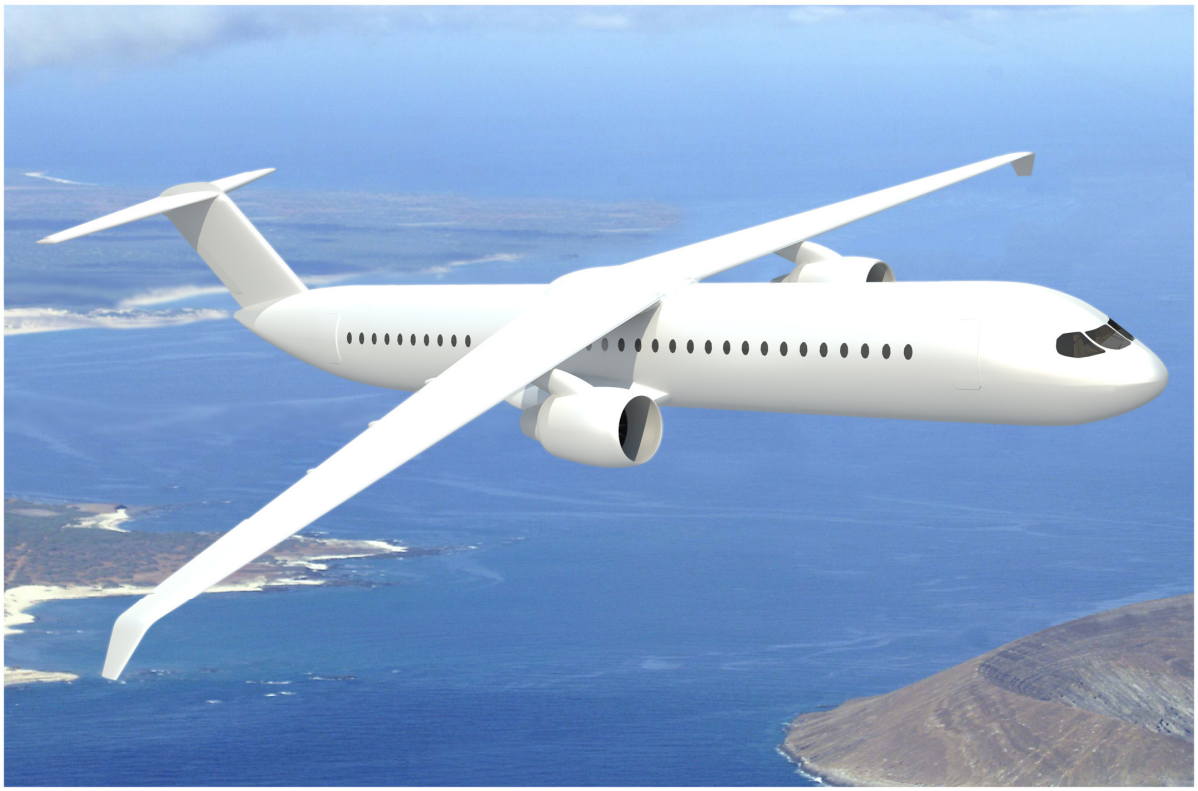

USC Advanced Commercial Concepts Presents:

Levant

University of Southern California

Devin Lewis
Member # 307714
Payload
Aesthetics
Ground Operations

Todd Erickson
Member # 421648
Propulsion
Configuration
Alternative Fuels

Sina Golshany
Member # 281677
Lead Designer
Propulsion
Configuration

Chris Nvavu
Invoice # 721079
Configuration
Structures
Ergonomics

Keith Holmlund
Member # 413045
High Speed Aerodynamics
Low Speed Aerodynamics
Aircraft Performance

Kristina Larson
Member # 306306
Management
High Speed Aerodynamics
Configuration

Phillip Adkins
Invoice # 715137
Acoustics
Numerical Analysis
Tool Development

Michael Zarem
Member # 416621
Systems Integration
Environmental Impact
Cost Analysis

Darin Gaytan
Member # 279164
Aircraft Performance
Configuration
Flight Dynamics

John Roehrick
Member # 421593
Weights
Acoustics
Systems

Dr. Ron Blackwelder
Faculty Advisor
Member # 1460

Dr. Oussama Safadi
Project Advisor
Member # 283128

Aaron Chang
Industrial Advisor
Invoice # 716176

Table of Contents

Nomenclature:

α	Angle of attack
AR_W	Wing aspect ratio
$\bar{\gamma}$	Average flight path angle
C_a/C_w	Aileron chord to wing chord ratio
C_{D_0}	Parasite drag coefficient
$C_{D0_{TO}}, C_{D0_{clean}}$	Airplanes zero-lift drag coefficient at takeoff, clean configuration
C_{ENVTAX}	Cost associated with environmental taxation
$C_{L_{max_{S(Clean)}}}$	Maximum lift coefficient for clean stall configuration
$C_{L_{max_{TO}}}$	Maximum lift coefficient at takeoff
$C_{L_{opt,MaxR}}$	Lift coefficient correspond to the optimum range performance
C_{l_a}	Airplane rolling-moment-coefficient due to ailerons deflection
$C_{m_{a,}}$	Airplane pitching-moment-coefficient-due-to-AOA derivative
C_{l_β}	Airplane rolling-moment-coefficient-due-to-yaw rate-derivative
C_{n_β}	Airplane yawing-moment-coefficient-due-to-side-slip-derivative
d/D	Ratio of the radome diameter to the average diameter of the mid fuselage
Δ_n	Correction factor due to pilot technique and handling qualities
$\Delta W_{F_{usedi}}$	Fuel weight used in the i'th segment
$\Delta c_{l_{\delta/TO}}, \Delta c_{l_{\delta/L}}$	Change of sections airfoil coefficient due to flaps deflection
$\Delta C_{L_{W\delta/TO}}, \Delta C_{L_{W\delta/L}}$	Change in wing lift coefficient due to flap deflection
$\zeta_{P,long}$	Longitudinal phugoid mode damping ratio
ζ_{SP}	Short period mode damping ratio
η_{i_f}	Flap inboard station, in term of wing half span
η_{O_f}	Flap outboard station, in term of wing half span
I_{xx_B}, I_{yy_B}, I_{zz_B}	Moment of inertia along the body axis
$Level_P$	Level for phugoid stability
$Level_{\xi_{SP}}$	Level for short period damping
$L/D\|_{TO}$	Lift-to-Drag ratio at takeoff
λ_w	Wing taper ratio
Λ_w	Wing sweep angle
Λ_{LE}	Leading edge wing sweep
M_{DD}	Drag divergence Mach number
M_i	Normalized emission multiplier

M_{ff}	Fuel Fraction: 1- (Fuel Weight/Takeoff Weight)
NP_{free}	Free stick neutral point
P_3	Combustor inlet pressure
Π_{TO}	Engine setting at takeoff
ϱ_F	Fuel density
Re_{tr}	Reynolds number corresponding to the chordwise transition to turbulence
S_{air}	Distance from the obstacle height to the point of touchdown
S_L	Landing distance
S_{LG}	Ground roll landing distance
S_{NO_x}	NOx severity index
S_{TO}	Total field length
S_{TOG}	Take-off ground run distance
S_W	Wing surface area
SM	Static margin
T_3	Combustor inlet temperature
$T_{1/2_P}$	Time to half amplitude in phugoid mode
T_{2_P}	Time to double amplitude in phugoid mode
T_{avail}	Thrust available
T_{req}	Thrust required
V_A	Approach speed
$V_{Cr_{Max}}$	Maximum cruise velocity
V_{LOF}	Speed at liftoff
V_{S_L}	Landing stall speed
$V_{S_{TO}}$	Takeoff stall speed
war	Water-to-air ratio
W_E	Empty weight
$W_{F\ \text{used}}$	Weight of fuel used
W_{TO}	Takeoff weight
$\left(W/S\right)_{TO_{max}}$	Maximum take-off wing loading
$\left(W/T\right)_{TO_{max}}$	Maximum take-off power loading
φ_T	Thrust vector inclination with respect to freestream airflow
X_{apex_W}	X coordinate of the wing apex (i.e. distance b/w wing quarter chord station and the nose reference point)
$\bar{x}_{ac}, \bar{x}_{ac_{wf}}, \bar{x}_{ac_h}$	X coordinate of aerodynamic center in terms of mean aerodynamic chord
X_{CG}, Y_{CG}, Z_{CG}	Location of center of gravity

$\bar{x}_{cg}$	X coordinate of center of gravity in terms of mean aerodynamic chord
$\omega_{n_{P,long}}$	Longitudinal phugoid mode undamped natural frequency
$\omega_{n,S.P}$	Short period undamped natural frequency

Acronyms:

AAA	Advanced Aircraft Analysis
AIAA	American Institute of Aeronautics and Astronautics
AIC	Aviation Induced Cloudiness
AIMC	Aircraft Information Management Computer
ACE	Actuator Control Electronics
APU	Auxiliary Power Unit
ASM	Air Separation Module
BPR	Bypass Ratio
CAROC	Cash Airplane-Related Operating Costs
CFD	Computational Fluid Dynamics
CG	Center of Gravity
DLU	Data Localizing Units
DOC	Direct Operating Cost
DSM	Design Structure Matrix
EPNdB	Effective Perceived Noise in Decibels
ESDU	Engineering Sciences Data Unit
ECS	Environmental Control System
E/E	Electrical/Electronics
EIS	Entry into Service Date
FAR	Federal Air Regulation
GTF	Geared Turbo Fan
HRJ	Hydrotreated Renewable Jet
HUD	Head Up Display
ICA	Initial Cruise Altitude
ISA	International Standard Atmosphere
L/D	Lift-to-Drag Ratio
MIDU	Multi-Function Interactive Display Unit
MLW	Maximum Landing Weight
NLF	Natural Laminar Flow
OEI	One Engine Inoperative
PFCC	Primary Flight Control Computers
RDTE	Research Development Testing and Evaluation
RFP	Request for Proposal
RMPU	Remote Power Management Unit
SAR	Specific Air Range
SFC	Specific Fuel Consumption
TSFC	Thrust Specific Fuel Consumption
UACC	University of Southern California Advanced Commercial Concepts
ULD	Unit Load Device

Acknowledgement:

Having completed this project, we would like to express our appreciation of the help and support given by the faculty of USC's aerospace and mechanical engineering department. First of all, we wish to thank the people who were integral to the creation of this project: *Dr. Ron Blackwelder, Mr. Blaine Rawdon,* and *Mr. Mark Page.* With their experience in the field of aircraft design, they have been very supportive in all the phases of this project. During the first months of his retirement, *Dr. Ron Blackwelder* contributed greatly to all aspects of this project, including technical and organizational support for team members. *Dr. R.J. Huyssen*, managing director of Diomedes Innovations, Ltd. also contributed greatly to by providing well needed advice and feedback, mostly in relation to configuration design and engine integration. Special thanks are also due to Marc Aubertine in USC's writing program for his contribution to the organization and composition of this proposal.

Several people have been instrumental in allowing this project to be completed, but above all, we are indebted to our editorial supporters: Professors *Larry Redekopp, Oussama Safadi, Fokion Egolfopoulos,* and *David Wilcox* who backed our efforts over the past year. We would also like to thank two individuals within the Boeing Company who provided encouragement to begin this project: *Dr. David J. Paisley,* and *Mr. Perry Rea.* Throughout this project we have received funding, as well as feedback and encouragement, from individuals in charge of the Los Angeles Professional Chapter of AIAA and the USC's Office of Undergraduate Research. Among many others we would like to thank *Dr. David Glasgow* at the University of Southern California and the Los Angeles branch of the AIAA chaired by Dean Davis for providing us with the essential funding for this research project to proceed. Last but not least, we wish to give thanks to all our friends and family for being there, providing both an understanding and supportive attitude in a multitude of ways.

May 2010, Los Angeles
USC's Advanced Commercial Concepts Team

Executive Summary:

The next generation of medium range commercial transport aircraft is considered to be the focal point of present-day research in the commercial aviation industry. The expected increase in oil price, the possible introduction of a carbon tax, and stricter environmental constraints have made the development of more efficient and environmentally compatible commercial aircraft necessary to replace the aging fleets of Boeing 737 and Airbus A320. This has created a substantial demand for viable successors to some of the most produced and commercially successful aircraft development projects in the history of aviation. This has resulted in the initiation of significant development in the fields of aircraft propulsion, systems, and structure to ameliorate the shortcomings of conventional configurations in the areas of fuel economy, carbon footprint, and aerodynamic efficiency. Echoing the needs of today's commercial aviation industry, the request for proposal issued by the American Institute of Aeronautics and Astronautics presents challenges, such as an increase in cruise L/D by 25%, use of alternative fuels, incorporation of modern subsystem technology, and utilization of novel configuration concepts to reduce the cost and environmental effects of future commercial transports.

Levant attempts to address these issues by integrating revolutionary and evolutionary concepts, such as Natural Laminar Flow (NLF), bleedless Geared Turbofan (GTF) engines that use alternative fuels, fully electric systems architecture, composite load bearing structure, and ultra-high aspect ratio swept forward wings that provide compatibility with current airport infrastructure while increasing overall aerodynamic efficiency. Using a GTF engine that reflects projections for state-of-the-art engine technology for 2020, Levant presents extreme improvements in fuel economy and emission levels produced by the engine; however, as will be presented in this proposal, the fan diameter and mass properties influence the installation of the engines and therefore determine the general aircraft configuration. As a result, Levant employs a twin, under-the-wing mounted Pratt & Whitney PW1000G turbofan engine installation. Emphasis is placed on obtaining a fail-safe

configuration that complies with industry and federal regulations for commercial aviation. In order to support the validity of the assumptions made, highly detailed analyses in the fields of transonic aerodynamics, propulsion, aero-acoustics, and weight were performed and these results were compared to values presented in literature. The resulting design presents tremendous improvements over today's state-of-the-art commercial aircraft technology as a result of integrating these novel concepts into the aircraft. It is realized, however, that by incorporating a substantial amount of new technology, a certain increase in project risk may occur. Efforts are therefore made to ensure that the increase in risk is financially justified and, in case of a delay or failure in any step of the relevant technological development, the adverse effects are minimized, considering both the changes of the future market, speculated to be dominated by aircraft with lower fuel burn, and emission levels, given the ever rising price of aviation fuel and the introduction of a carbon tax in the years to come.

Given the performance increase achieved and the relatively high order analytical tools, it is the unilateral belief of the USC Advanced Commercial Concepts (UACC) that Levant represents a configuration with the greatest potential as a replacement for presently operational, mid-haul commercial jetliners.

Requirements Matrix

Table 1. Selected design parameters

Parameter	Requirement	Levant	Section
RFP			
Take-Off Distance	8,200 *ft.*	7,323 *ft.*	11.1
Landing Speed	< 140 KCAS	140 KCAS	11.5
Cruise Speed	Mach 0.8	Mach 0.8	13.1
Max Operating Speed	Mach 0.83/ 340 KCAS	Mach 0.8/ 467 KCAS	11.3
Initial Cruise Altitude	>35,000 *ft.*	39,000 *ft.*	13.1
Max Cruise Altitude	>41,000 *ft.*	42,000 *ft.*	13.1
Max Range	3,500 *nm*	3,500 *nm.*	11.4
Nominal Range	1,200 *nm.*	1,200 *nm.*	11.4
Payload Capability	37,000 *lbs.*	37,000 *lbs.*	2.7
Alternative Fuel Capabilities	Compatible	HRJ related algae based biofuel	10.1
Passengers	~175	174	2.2,2.7
Seating Pitch	32 *in.*	32 *in.*	2.7
Seating Width	17.2 *in.*	17.2 *in.*	2.2
Cabin Height	>7.25 *ft.*	7.25 *ft.*	2.2
Cabin Width	>12.5*ft.*	12.6 *ft.*	2.2
Cargo Volume	1,240 $ft.^3$	1,410 $ft.^3$	2.2
Materials	Composites 787	Carbon laminated composites	8.1
Cruise L/D	18.2 (737-800) (used as baseline)	22.8	4.7
FAR			
§25.810 & §25.117 Emergency Egress	Emergency door sizing	Satisfied	2.2
§25.121 Climb Performance	1.2%	1.9%	11.2
§25.111 OEI Climb Gradient	1.2%	1.9%	11.2
§25.105 Transition Phase Climb	2.4%	2.8%	11.2
§25.335 Gust Loading	50 *ft./sec.* max	50 *ft./sec.* max	8.2

1. Design Process

1.1 Design Methodology

The general design philosophy of Levant has been substantially influenced by methodology presented by *Jan Roskam*[1] and *Ed Heinemann*[2]. It should be noted that these methods are often quite extensive and cover technical aspects of the analysis in great detail. The majority of calculations performed and referenced within the proposal use published graphs and tables in order to determine the constants and parameters, often consisting of multiple time-consuming permutations. While the theoretical backgrounds of these methods are discussed in various parts of this proposal, many of the mathematical models and statistical data used in the design process are not presented in their entirety in the interest of brevity.

Design Structure Matrix (DSM), a modern method of development management, was used in order to determine the optimum design process. This method, described by *Eppinger et al.*[3], is used to organize interrelated tasks in the design process in a way that minimizes feedback cycles and determines possible parallel analyses. The PSM 32 code, developed by Blitzkrieg Software, was utilized to implement the DSM in the routine process of developing Levant. Utilizing this code, the entire design process was re-ordered based on the degree of dependency of each sub-process on the outputs of others. As a result, the design approach presented by *Roskam* has been slightly modified so as to allow for additional parallel processes, as dictated by specific needs of the Levant's concept, and consequently, improved development speed.

Lastly, complex Computational Fluid Dynamics (CFD) tools were used to verify the feasibility of the acclaimed NLF. This was done with the highest accuracy possible given the limited available computing power to UACC. The CFD tools provide a reasonable estimate of the trends expected to maintain NLF on the wing even though the values have relatively large uncertainties. This confirms the feasibility of such NLF concepts.

2. Configuration Description

2.1 Wing

The wing planform for Levant has an equivalent area of 1,530 $ft.^2$ and a span of 147.1', resulting in an aspect ratio of 14.1. The quarter chord sweep of the wing is -5.9° while the leading edge sweep is -8.1°. The taper ratio of the wing is 0.28, selected to optimize the Oswald's Efficiency factor for the wing at cruise. Choices surrounding planform are driven by aerodynamic trade studies and optimizations that are highly influenced by the concept of NLF. The low swept forward wings, combined with custom designed NLF airfoils, allow for extensive laminar flow (approximately 45%) on upper and lower surfaces of the wing, drastically reducing the friction drag of the configuration at cruise conditions. Swept forward wings experience a smaller effective sweep angle than swept aft wings, allowing the laminar flow boundary layer to be more stable against attachment line transition and crossflow instability[4]. Levant also features a high wing mounted above the passenger cabin and blended into the fuselage through a smooth fillet. Sections 4.2 and 4.4 of this proposal present the justification for the NLF characteristics and wing planform optimization, respectively. To further increase the efficiency of the wing planform, a 6' downward-facing winglet is canted from the vertical at 15°. Figure 1 presents the wing planform using this configuration.

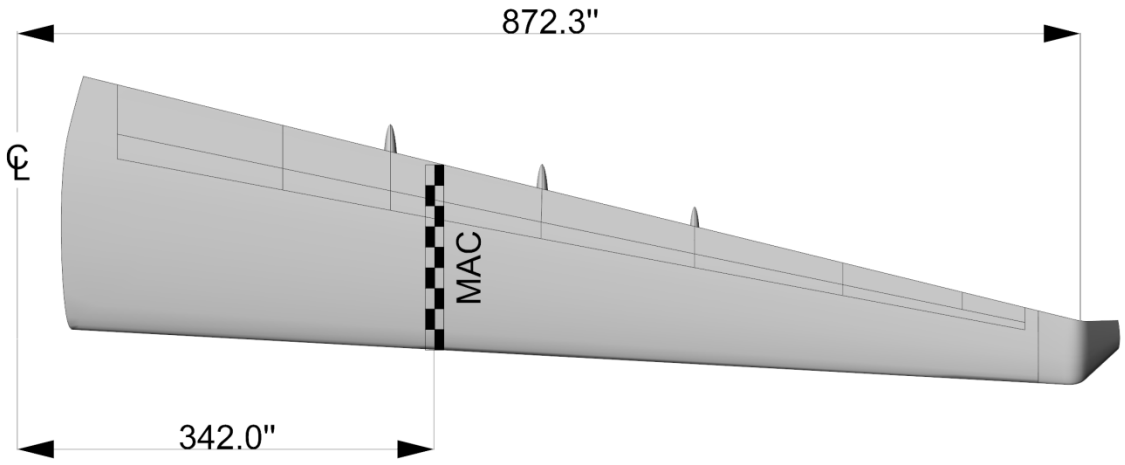

Fig. 1 Wing planform

The wing is equipped with four sets of double slotted Fowler flaps on the trailing edge extending up to 75% of the total wingspan. On the trailing edge of the outboard section of the wing a flaperon surface extends to the inner edge of the wingtip. The wing also accommodates spoiler surfaces that are used for auxiliary control in flight and reducing the speed of the aircraft on the ground.

The trailing edge of the wing features a slight sweep of -12.3° which causes the effectiveness of the trailing edge high lift devices to increase tremendously[5]. To prevent the flow from being tripped by slightly misaligned external surfaces near the leading edge of the wing, no leading edge high lift devices were utilized, as recommended by *Edi* and *Fielding*.[6] The wing structure consists of two main spars passing through the crown of the fuselage at 15% and 65% of the chord. Ribs are placed perpendicular to the spars and spaced from 23.5" to 15.2" depending on their span-wise location. The main wing structure is connected to the fuselage through the central wing box which is fixed to the upper part of the reinforced frames. A keel beam inside the lower deck of the fuselage increases the local stiffness near the landing gear pods. The fuel is housed inside the wings from the central wing box to 85% of the wingspan. The estimated total wing fuel volume is approximately 835 $ft.^3$, resulting in about 6,250 U.S. gallons of fuel. Figure 2 presents the wing structure and high lift systems.

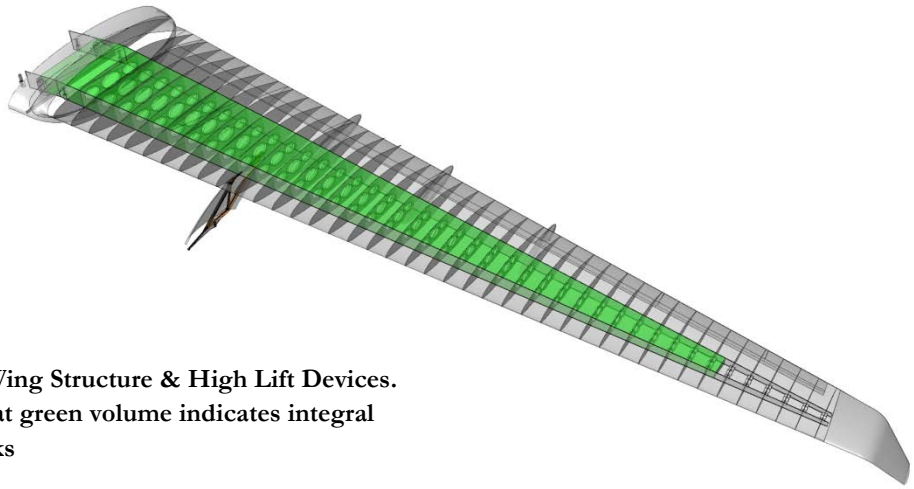

Fig. 2 Wing Structure & High Lift Devices. Note that green volume indicates integral fuel tanks

2.2 Cabin Design

Levant features an elliptical cross-section with exterior semi-major diameter of 159.4" and semi-minor diameter of 155.5". The pressurized section of the fuselage is 1,372" long and is capable of housing 174 passengers in a single class, single aisle arrangement with a seat pitch of 32" and seat width of 17.2" as outlined by the Request for Proposal (RFP). The interior cross-section designed for Levant is presented in Fig. 3. As requested in the RFP, the interior dimensions of the cross-section were selected such that after integration of structures and systems, the cabin width is greater or equal to 151" (12.6') and cabin height is 87" (7.25'). The cargo compartment is designed to house containerized cargo with maximum dimensions of 45" x 95". Overhead bag racks are designed to provide 2.7 ft^3 of volume for the passengers in a seating arrangement with a seat pitch of 32". Levant has the capability of carrying a maximum of 1,410 ft^3 of containerized cargo and 180 ft^3 of bulk cargo on the lower deck.

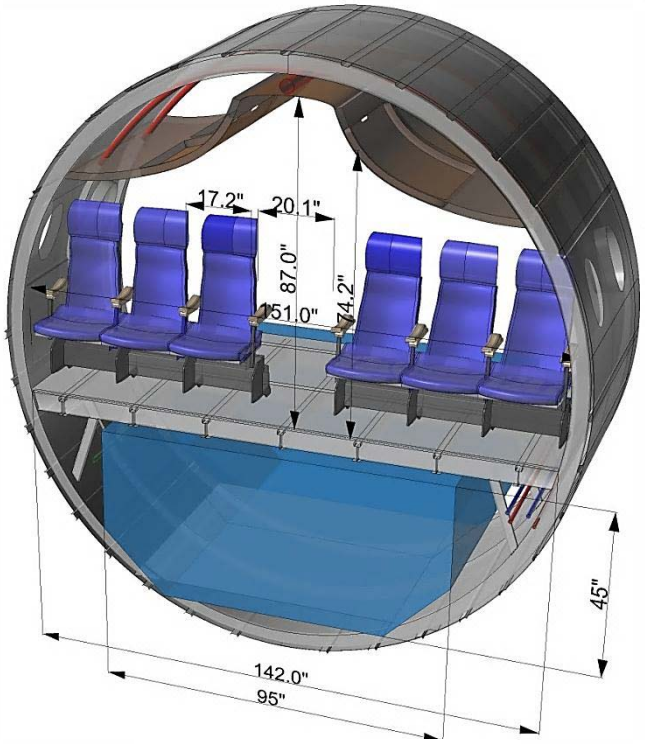

Fig. 3 Fuselage Cross-section

The fuselage is designed based on requirements presented by the Federal Air Regulation (FAR) §25.810 and the amendment §25.117 to this regulation, which requires a 20" clearance row in front of the Type III emergency exits. The main exits and emergency exits designed for Levant are estimated to support an emergency egress of 247 passengers within 90 seconds from the aircraft, allowing for a further expansion of passenger capacity in case of an increased market demand for an extended version of Levant.

2.3 Fuselage Geometry

The forebody of the fuselage features a smooth manifold surface with an ESDU Type I top profile[7] and a customized side forebody profile with a bluntness ratio of 0.73. This is mainly driven by the optimization efforts to minimize the pressure drag, as well as increase the extent of laminar flow on the forebody as will be discussed in Sec. 4.1. The upper sides of the forebody are modified in order to minimize curvature, making the integration of cabin transparencies easier. The forebody possesses an overall fineness ratio of 1.25. The aftbody of the fuselage presents a closure angle of 14° and a fineness ratio of 2.5. The main landing gear is of the tricycle type and is mounted on a gear beam, which is attached to the fuselage and the rear spar of the wing, allowing it to fold into a dedicated landing gear pod blended into the fuselage. The fairing size of the gear pod has been minimized in order to reduce the excrescence and pressure drag. Figure 4 shows the fuselage geometry and landing gear.

(a)

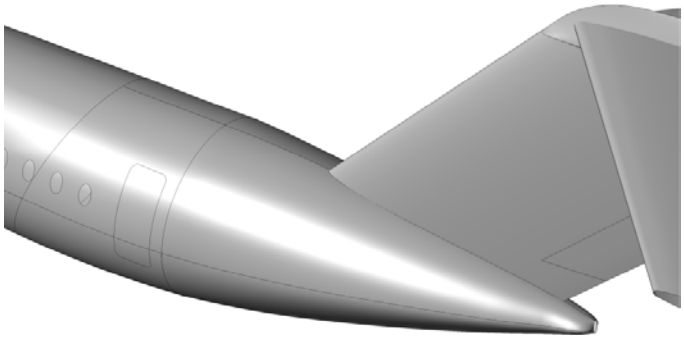

(b)

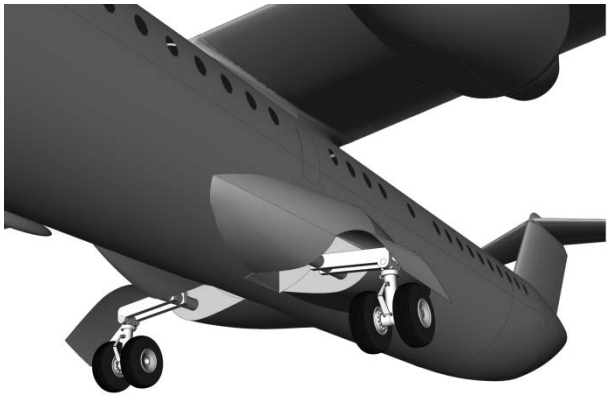

(c)

Fig. 4:
(a) Fore body geometry.
(b) Aft body geometry
(c) Wing-Fuselage Fairing showing the main landing gear folding mechanism and landing gear well.

2.4 Engine Type and Installation

Levant utilizes a Pratt & Whitney PW1000G two-spool GTF with a diameter of 72"[8]. The bypass ratio (BPR) of the engine was estimated, using the GasTurb analysis package, to be around 10. This engine has been designed to demonstrate state-of-the-art GTF engine technology and therefore uses the published projections with regards to combustor efficiency, compressor efficiency, and turbine inlet temperature. This GTF engine has been designed to meet the performance requirements set by the RFP and is capable of generating 4,900 *lbf* of thrust at 40,000' and Mach 0.8. As a result, the engine is designed to be capable of producing 17,500 *lbf.* of thrust at sea level and static conditions. An initial weight analysis of the engine indicates a weight of 5,150 *lbs.* which is considerably higher than any comparable turbo fan engines in terms of thrust. The engines were installed under the wing, which is near the aircraft's center of gravity, so that the fuselage may be extended in the future to carry more passengers while avoiding the need for increasing the tailplane surface area or redesigning the wing-to-fuselage joint. A detailed analysis of the engine and selection justification is presented in Chapter 5 of this proposal. Figure 6 presents the pylon integration of the engine under the wing.

Fig. 5 Geared Turbofan engine

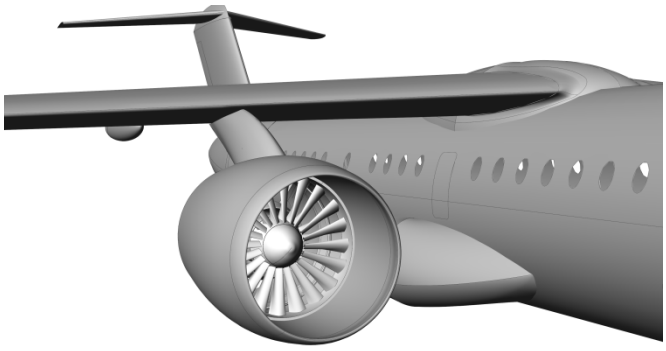

Fig. 6 Engine integration

2.5 Empennage

The empennage of Levant consists of a T-tail configuration selected to keep the horizontal tail planform away from the intense jet wash produced by the engines. The horizontal tail has a planform area of 342 ft^2 and a span of 36.5', resulting in an aspect ratio of 3.9. The quarter chord sweep of the horizontal tail is 36° while the leading edge sweep is 18.7°. The vertical tail has an aspect ratio of 1.1 and does not feature any taper in order to maximize the tip chord length, therefore maximizing the volume available for the installation of the variable incident horizontal tail on top of the vertical tail. The vertical tail surface is swept aft by 35° to increase the horizontal tail moment arm, effectively reducing the horizontal tail planform area needed to initiate takeoff rotation. The horizontal tail is equipped with elevators on the trailing edge extending up to 93% of the tail span. The structures of the horizontal and vertical tails are conventional, semi-monocoque, composite elements that are fixed on the upper side of the fuselage frames.

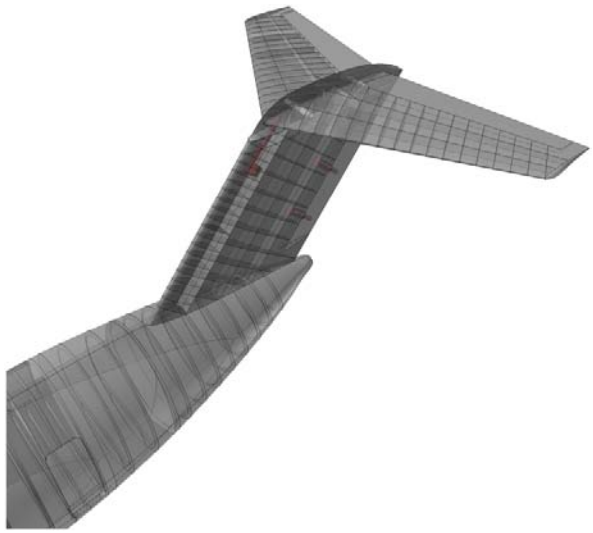

Fig. 7 Empennage and aft body integration of aircraft

Levant

	Wing	Horizontal Tail	Vertical Tail
Area	1530 ft.^2	342 ft.^2	310 ft.^2
AR	14.1	3.9	1.1
Taper	0.28	0.45	1
C/4 Sweep	5.9 deg.	36 deg.	35 deg.
LE Sweep	8.1 deg.	18.7 deg.	35 deg.
Dihedral	3 deg.	-3 deg.	N/A
Root t/c	11 %	9 %	10 %
Tip t/c	9.5 %	9 %	10 %
Twist	-4 deg.	0 deg.	0 deg.

Valuesiin this table were obtained from trapizoidal simplifications and do not match the geometry shown.

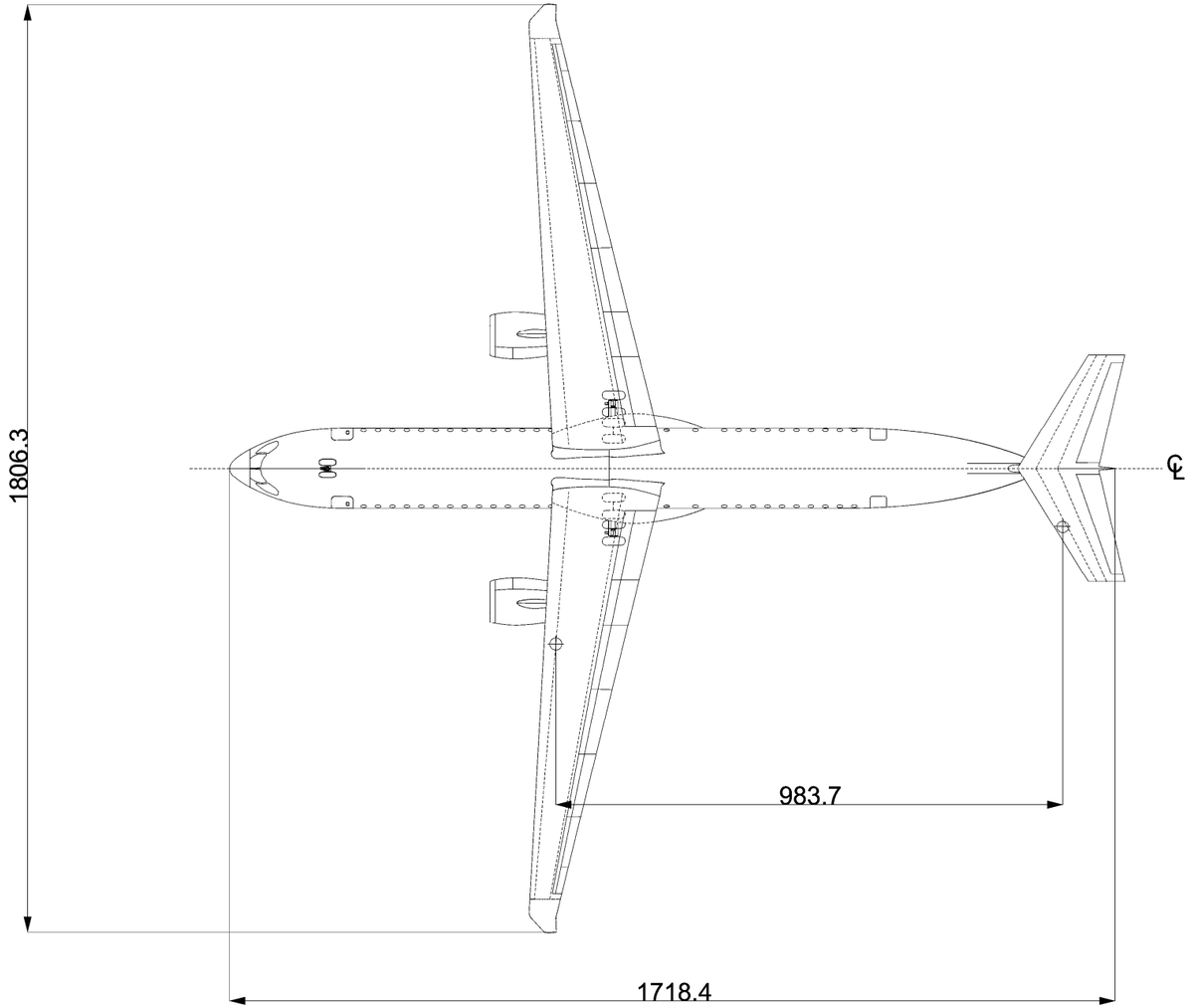

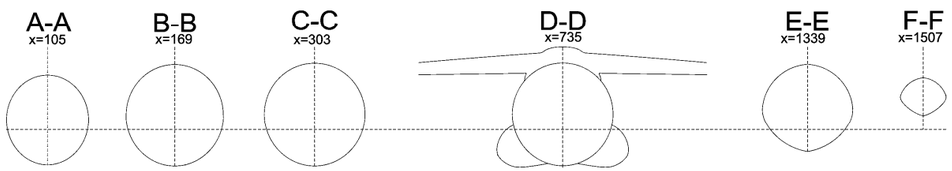

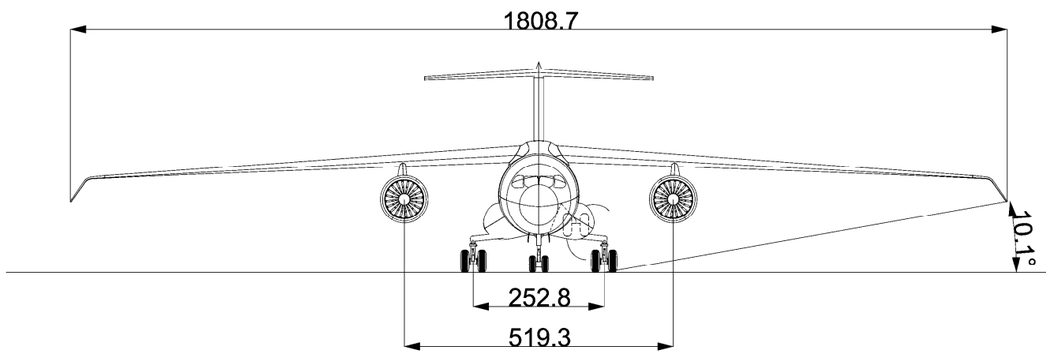

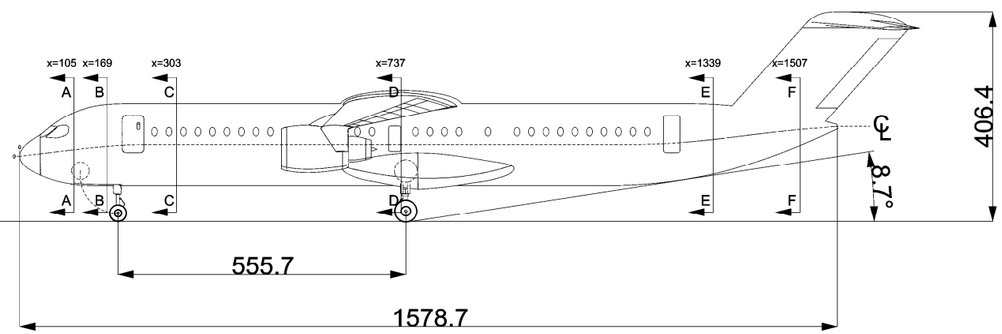

Levant

Inboard Profile (Top) and Interior Arrangement of Levant. Views of the interior design of galleys and lavatories are also presented

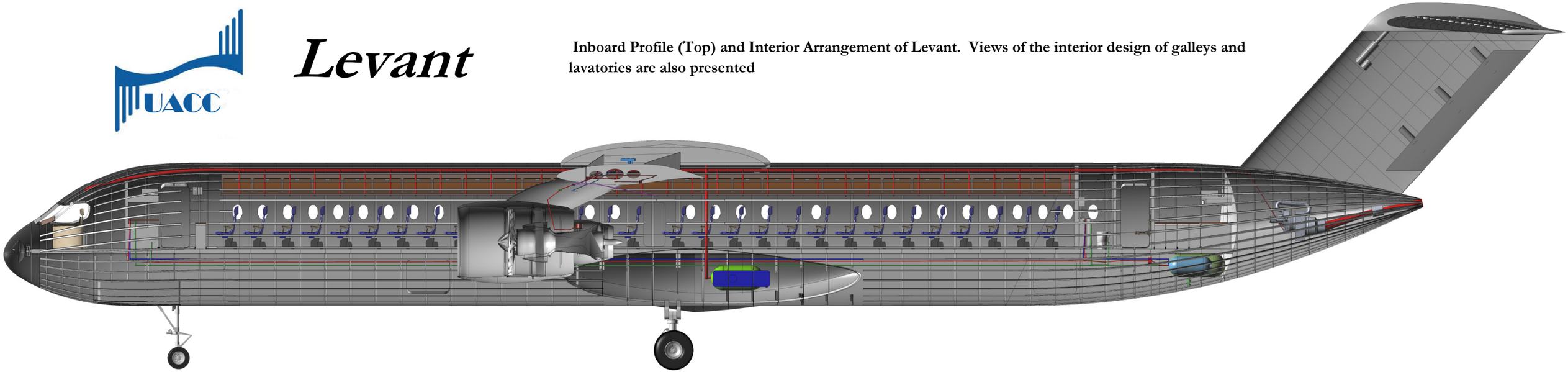

1372"

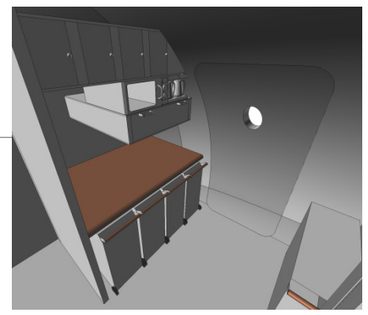

Type B Door
32" x 72"
x = 193"

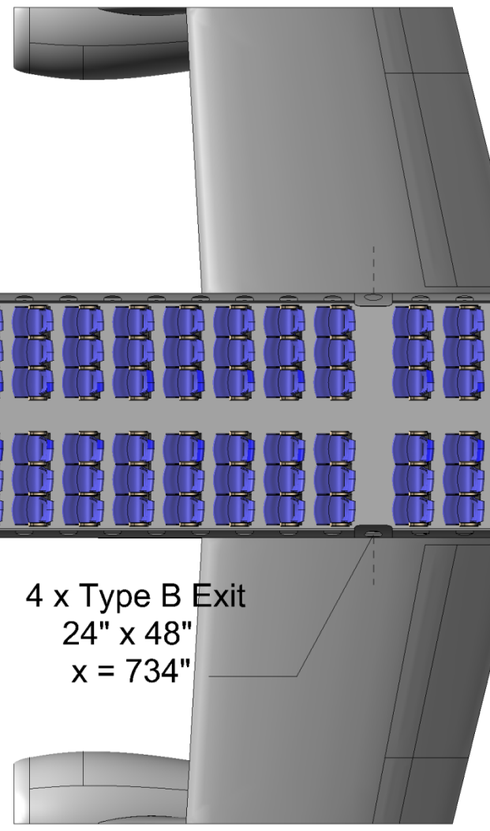

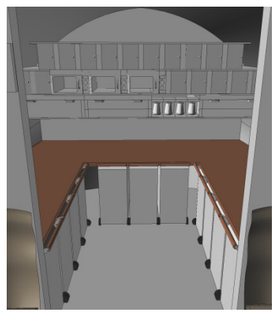

2 x Lavs.

Type A Door
42" x 72"
x = 217"

4 x Type B Exit
24" x 48"
x = 734"

2 x Type B Door
32" x 72"
x = 1260"

1580"

3. Sizing

3.1 Initial Laminar Flow Technology Assessment

In reviewing literature relevant to technology developed for high Reynolds number laminar flow airfoils, and in examining studies on delaying the transition to turbulent flow by reducing the leading edge sweep of the wing surface, it was decided that NLF technology will be a viable technology available in the timeframe of 2020. In particular, papers published by *Redeker* et al.[9] and *Lehner* et al.[10] expressed favorable opinions on the availability of NLF technology within the 2020 timeframe. Significant performance improvements are achievable by careful application of these concepts for future aircraft configurations; however, a paper published by *Holmes*[11] suggests that the proposed aerodynamic benefits obtained by application of NLF are limited by the roughness of the manufactured aircraft surfaces. Performing a case study analysis, details of which can be found in Sec. 4.4 to serve as a rough estimate of L/D benefits obtained by having half of the upper surface in laminar flow, it was concluded that an 8% improvement in cruise L/D would serve as a reasonable estimate for the preliminary mission analysis of Levant[12].

3.2 Mission Analysis and Preliminary Weight Estimations

A typical mission profile was adopted from AIAA[13] and is presented below in Fig. 8.

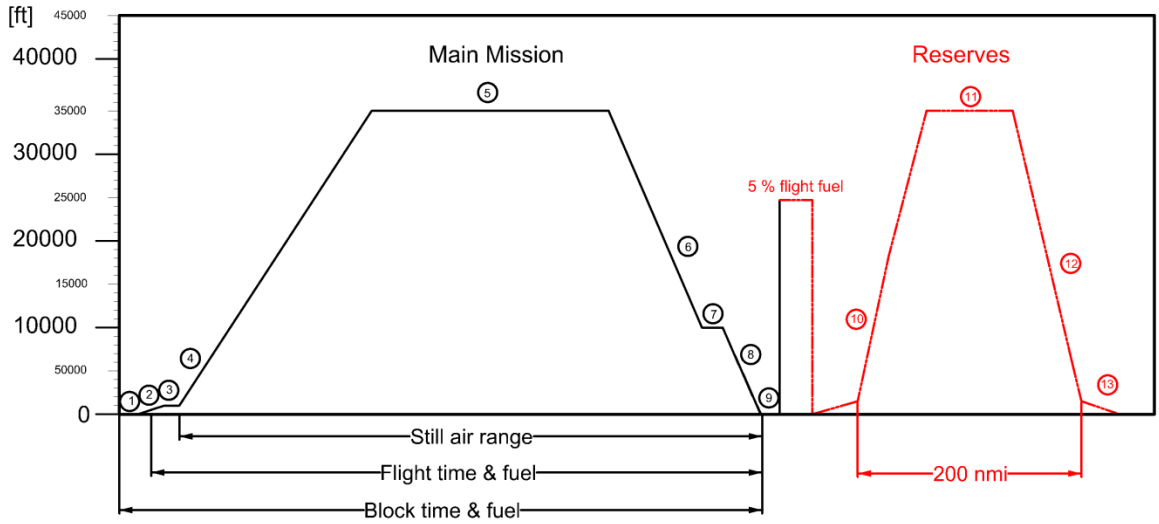

Fig. 8 Mission Profile of Levant. Note that the red portions indicate the reserve mission

Using the methodology presented by ESDU Performance Data Items 73018[14], 73019[15], and 74018[16], combined with *Roskam's*[17] low order statistical weight estimation methods, the mission analysis was performed. Table 2 presents the results for Levant. It was assumed that the target improvement in L/D specified by the RFP (25%) was obtained and Boeing 737-800 was selected as a comparable baseline airplane for the purpose of this mission study. Considering the use of GTF engine concepts, the specific fuel consumption of the engines was reduced by 16%, as claimed by *Godston & Reyolds*[18].

Table 2. Preliminary Mission Analysis Results.
Note the green segments indicate the reserve mission profile

Mission Segment	Altitude (*ft.*)	Mach	Distance (*nm.*)	Time (*min.*)	SFC (lb/lb-hr)	$\Delta W_{F\,used}$ (lb)
1-Warm up	0	0	0	5	0.25	1,870
2-Taxi Out	0	0	0	4	0.25	1,850
3-Takeoff	150	0.12	0	1	0.30	9,060
4-Climb	1,000-36,000	0.3	33	8	0.40	570
5-Cruise	36,000	0.8	3,500	380	0.59	26,120
6-Descent	36,000-10,000	0.5	33	8	0.40	1,550
7- Loiter	10,000	0.2	0	2	0.36	280
8- Descent	10,000-0	0.2	10	2.5	0.36	1,550
9- Land/Taxi	0	0	0	5	0.25	1,160
10- Climb	0-15,000	0.3	20	4.5	0.40	270
11- Cruise	15,000	0.5	180	30	0.47	1,670
12- Descent	15,000-0	0.2	50	15	0.40	1,500
13- Land/Taxi	0	0	0	5	0.25	1,180

Using the weight fractions obtained from *Roskam*[8], as well as the results for the mission analysis, initial estimations for empty, takeoff, and required fuel weight of the aircraft were performed. Table 3 presents the results of this analysis. Note that these results only reflect the statistical trends in commercial aviation and are later refined in Ch. 7 using higher order methods of estimating weight.

Table 3. Summary of initial weight analysis

W_E	74,750 *lbs.*
W_{TO}	155,770 *lbs.*
M_{ff}	0.7842
W_{Fused} (max)	41,875 *lbs.*

3.3 Preliminary Drag Polars

Using the 2nd order regression methods presented by Roskam[19,20], as well as the results obtained from the preliminary weight and mission analyses of Levant, initial empirical drag polars were obtained in order to complete preliminary performance sizing. ESDU Performance Data Item 73019[21] was consulted to choose the critical parameters with the highest influence on fuel burn. Three parameters were chosen to determine the optimal lift coefficient for the aircraft when operating at cruise: C_L/C_D, $C_L^{0.5}/C_D$ and $C_L/C_D^{3/2}$. ESDU 73019 suggests $C_L/C_D^{3/2}$ to be maximized, which corresponds to the maximum Specific Air Range (SAR) at a fixed cruise Mach of 0.8. SAR represents the sensitivity of the air range of the aircraft to its takeoff gross weight and, therefore, the amount of fuel burned during cruise. As it can be seen from Fig. 9b, the SAR is maximized if the aircraft is operating at a lift coefficient of 0.58, which is significantly lower than the lift coefficient corresponding to maximum L/D (0.79). However, one could observe that the C_L/C_D curve in Fig. 9b is relatively flat around a lift coefficient of 0.58; therefore, the reduction in maximum air range as a result of optimizing the aircraft for maximum SAR is minimal.

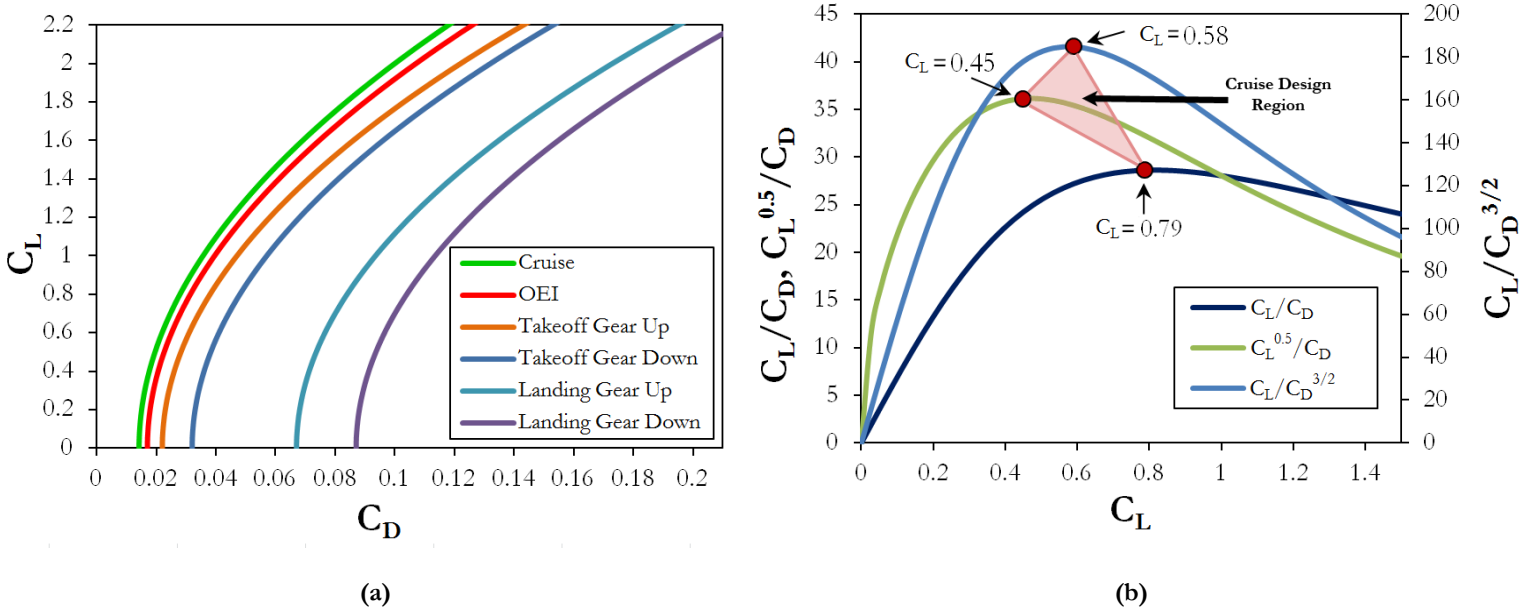

Fig. 9 Results of the preliminary aerodynamic projections. (a) Preliminary drag polars for different mission segments of the aircraft. (b) Parametric analysis of lift and drag data. C_L corresponding to maximum C_L/C_D maximizes the range at constant Mach number. C_L corresponding to maximum $C_L^{0.5}/C_D$ maximizes the range at constant altitude. Parameter $C_L/C_D^{3/2}$ maximizes the SAR of the configurations and was selected based on the recommendations made by ESDU 73019 as a measure of merit, defining a design region for the cruise C_L of the aircraft.

3.4 Performance Sizing

The initial performance sizing of the aircraft was completed based on the performance requirements presented by the RFP, summarized in Table 1, and methods presented by *Roskam*[22]. The wing loading and thrust-to-weight ratios were obtained by solving performance boundary equations. Based on ESDU Aerodynamics 95021[23], it was assumed in this analysis that a maximum lift coefficient of 2.2 is achievable by using stand-alone double slotted Fowler flaps with no leading edge high lift devices. Weight figures obtained from preliminary weight estimates were used in conjunction with lift and drag characteristics obtained from preliminary aerodynamic analysis, which are presented in Sec. 3.2 and 3.3, respectively. A matching plot was constructed by overlaying the performance boundary graphs to identify the acceptable design space for wing loading and thrust-to-weight ratio for Levant. The result of this analysis is presented in Fig. 10.

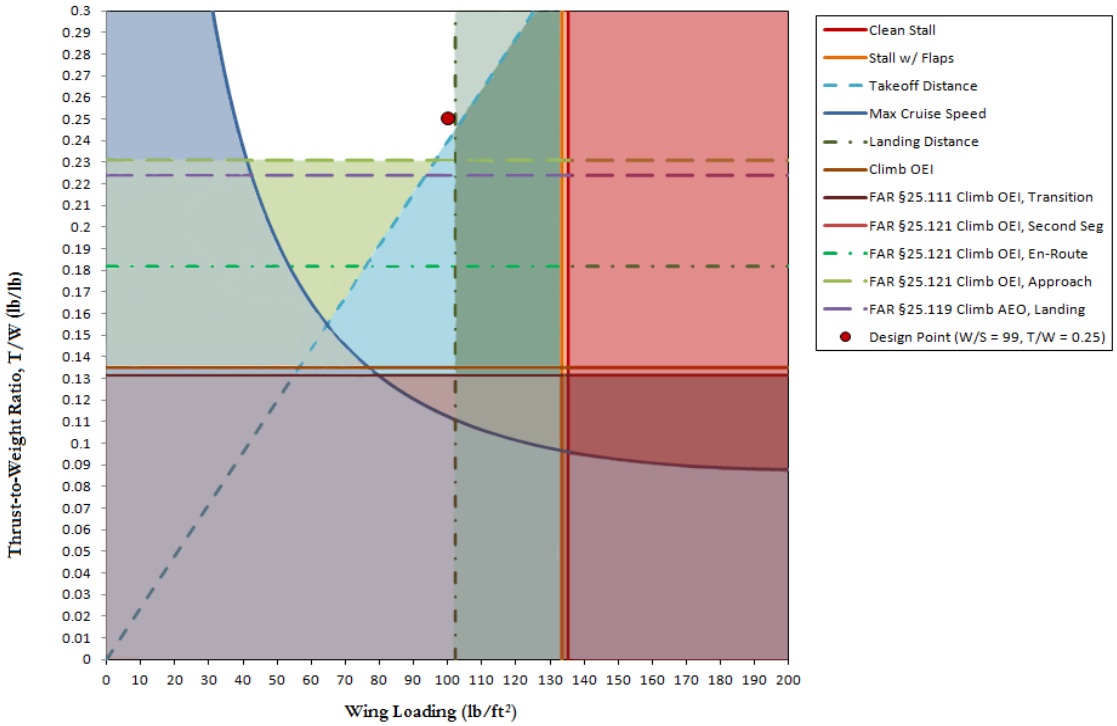

Fig. 10 Preliminary Aircraft Sizing. Design space is indicated by the white area.

As can be seen in Fig. 10, the thrust-to-weight ratio and wing loading of Levant is limited by the critical performance requirements for takeoff and landing distance. It should be noted that these requirements supersede the climb requirements set by FAR-25 regulations, which is typically the limiting case for aircraft performance sizing in aircraft with typical high-lift devices.

4. Aerodynamics

4.1 Fuselage Forebody Transonic Optimization

To minimize the wave drag of the forebody section of the aircraft, ESDU data item 74013[24] was used to select the optimum length-to-diameter ratio given the maximum cruise Mach number specified by the RFP (0.83). Figure 11 presents the results of this analysis, which indicate that a forebody length to diameter ratio of 1.25 would correspond to a drag rise Mach number of 0.83. A parametric study was performed using the equations presented in ESDU Data Item 83017[25] in order to determine the optimal bluntness ratio that minimizes wave drag penalties on the forebody, the results of which can be seen in Fig. 12. Efforts were spent to maximize the symmetry of the side profile of the forebody, thus maximizing the extent of NLF[26]. A three-dimensional CFD analysis was conducted using COSMOS FloWorks in order to investigate the extent of laminar flow on the final forebody geometry, the result of which can be seen in Fig. 13.

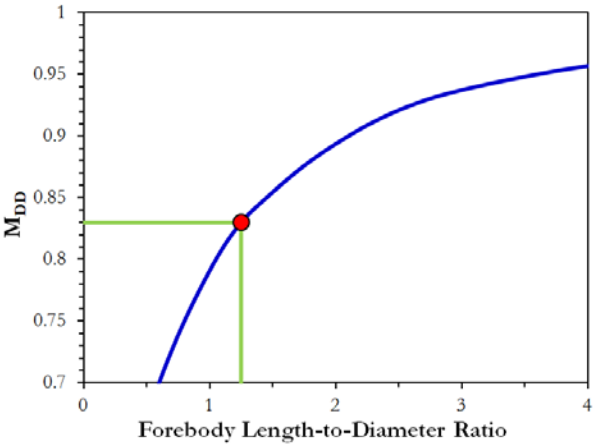

Fig. 11 Drag Divergence Mach Number vs. Forebody L/D

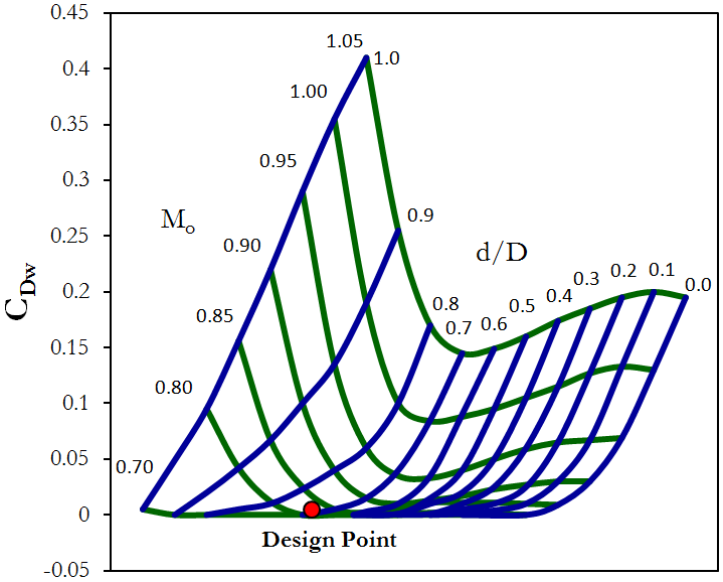

Fig. 12 Forebody Wave Drag Coefficient Vs. Cruise Mach Number (M_o) and Bluntness Ratio (d/D). The bluntness ratio corresponding to the lowest wave drag coefficient was chosen as the design point.

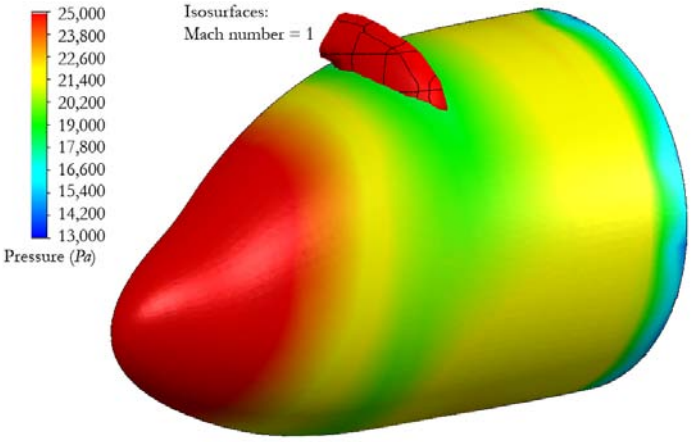

Fig 13 Total pressure contour on the forebody geometry suggests that a favorable pressure gradient is achieved up to the green areas, therefore allowing for possible maintenance of laminar flow. A slight shock is observed on the crown.

4.2 Detailed Analysis of Laminar Flow

Based on the review of general literature, it was decided that laminar flow technologies should be incorporated into the configuration design of Levant if the substantial 25% increase in L/D required by the RFP is to be achieved. Given the substantial increase in weight and complexity cited for hybrid laminar flow* devices by *Edi et al.*[27], as well as the favorable opinions expressed in regards to the feasibility and benefits of NLF concepts by authors such as *Lee et al.*[28] and *Lehner*[29] et al., the decision was made to incorporate modern NLF concepts into the aerodynamic design of Levant. Two general strategies were adopted to maximize the extent of NLF. First and foremost, airfoils were to be designed in such a way as to minimize the extent of adverse pressure gradients on the upper surface of the wing, thus extending laminar flow on the wing surface[5]. This strategy will be discussed in Sec. 4.3. Secondly, it was concluded that by implementing a wing planform with very small leading edge sweep, the effects of cross flow instability†, which contribute greatly to the transition to turbulence[5], could be minimized. It is realized that by reducing the sweep of the wing, one might expect an increase in the compressibility component of the aircraft's drag. Considering the fact that the total drag of a commercial aircraft is dominated by friction components at transonic speeds[30], a tradeoff exists between increasing the sweep of the wing to reduce compressibility drag and decreasing the sweep to increase NLF at the expense of slightly greater compressibility drag. The general consensus in literature is that predicting the location of transition to turbulence is an incredibly sophisticated task requiring complex numerical tools or extensive transonic experimentation, which is beyond the capabilities of the UACC. In order to investigate this tradeoff, the analytical method presented by *Lehner*[31] to estimate the transition location for a transonic wing was used. Equation 1 presents the *Lehner's* equation that predicts the Reynolds number corresponding to the chordwise transition to turbulence as a function of leading edge sweep.

---

* Hybrid laminar flow refers to the concept of inducing suction on the upper or lower wing surfaces in order to keep the flow attached and delay the transition to turbulence.

† Cross flow instability refers to transition to turbulence caused by the component of the streamwise flow that travels in the spanwise direction and trips the adjacent flows into increased turbulence levels; therefore increasing the friction drag of the surface.

$$\mathrm{Re}_{tr} = 24 \cdot 10^6 - \mathrm{atan}\left(\frac{\Lambda_{LE} - 13}{13} \cdot 1.6\right) \cdot \frac{28 \cdot 10^6}{\left(2 \cdot \mathrm{atan}(1.6)\right)} \quad (1)$$

This model was incorporated into the general aerodynamic analysis used to perform the wing planform optimization, which will be presented in Sec. 4.4. Extensive CFD studies later verified the results for the chordwise percentage of laminar flow obtained by *Lehner's* equation.

4.3 Airfoil Selection/Optimization

The method for selection of airfoil profiles was dictated by two main elements. First, in order to maximize the extent of NLF on the upper surface, a favorable "rooftop" shape pressure coefficient distribution[7] was sought. Second, the airfoil geometry must be of sufficient thickness to house the wing structure. The limits for thickness-to-chord ratio were set to 15% for root, 11% for mid-planform, and 10% for the outboard wing airfoil. In order to obtain a reasonable baseline airfoil, a study of 30 transonic airfoil geometries, available on the University of Illinois Urbana-Champaign's web portal, was conducted. The airfoils were analyzed using the DesignFoil software on the merit of the maximum extent of laminar flow at C_L 0.58 (selected in section 3.3). From the initial 30 airfoils studied, eight airfoils were selected for the design. Using the eight final airfoils, 40 combinations of upper and lower surface curves were analyzed in order to select the best performing airfoils. NASA Langley's NLF-415 was selected as the root airfoil profile. For the quarter span airfoil, the BAC NLF airfoil was selected as the upper profile, and the RAE 2822 airfoil as the lower profile. The SC2110 airfoil was selected as the tip profile. Camber adjustment was performed on the quarter span and tip airfoils to increase their section cruise L/D. CFD analysis using ANSYS CFX was performed to verify the location of transition to turbulence. Figures 14 and 15 present a summary of the results of the transonic CFD analysis performed on the root and tip airfoils.

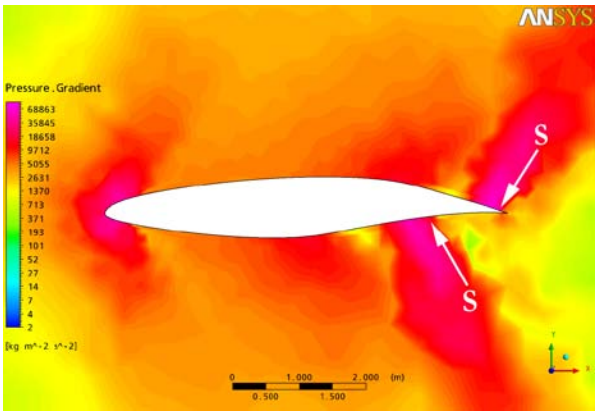

Fig. 14a Pressure Gradient for wing root airfoil

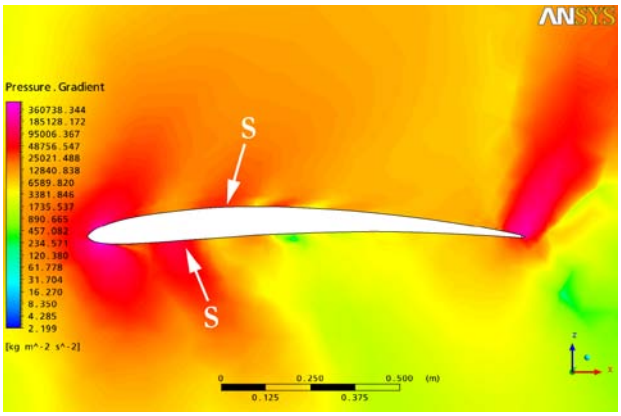

Fig. 15a Pressure Gradient for wing tip airfoil

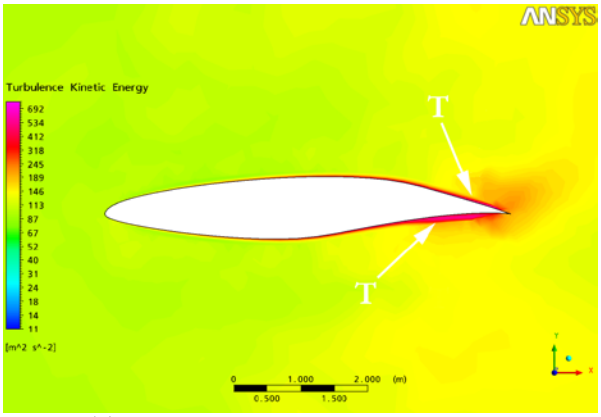

Fig. 14b Turbulence Kinetic Energy for wing root airfoil

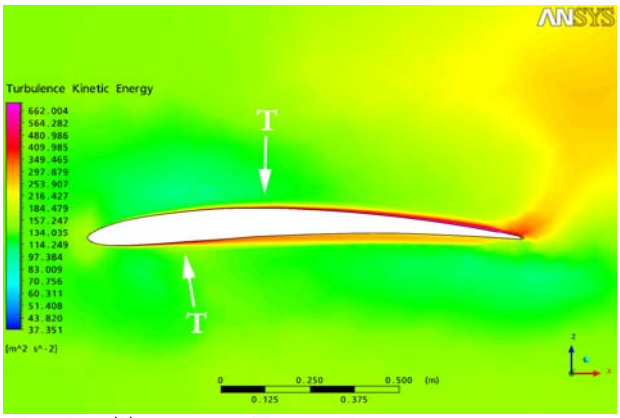

Fig. 15b Turbulence Kinetic Energy for wing tip airfoil

Transonic CFD analyses were performed on tip and root airfoil profiles to determine the location of the transition to turbulence. The analyses are simulating the stream wise flow speed of 0.8 Mach with the International Standard Atmosphere (ISA) atmospheric conditions at 36,000'. The chord length selected for the analysis corresponds to the final wing planform geometry. Pressure gradient contours indicate the existence of normal shocks at points marked by "S" and turbulence kinetic energy contours show transitions locations marked by "T". Averaging the location of transitions on top and bottom sides of the root and tip airfoils yields a 50% laminar flow for the wing.

4.4 Wing Planform Optimization

Based on the NLF method presented in Sec. 4.1, parametric studies were performed in order to obtain the optimal aspect ratio and quarter chord sweep angles that would maximize the L/D of the aircraft, assuming level flight at the cruise condition with a lift coefficient of 0.58. A procedure was developed to compute the percentage of laminar flow on the wing as a function of wing area, aspect ratio, and quarter chord sweep angle using *Lehner's* equation (Eqn. 1).

A parametric analysis was performed by varying the aspect ratio of the wing from 9 to 15 and the quarter chord sweep angle of the wing from 0º to 25º. Considering the results presented in Sec. 4.3, which indicate that an average 50% laminar flow is achievable* (between upper and lower surfaces of root and tip wing profiles), this analysis was normalized to 50%. Figure 16 presents the results of this parametric study.

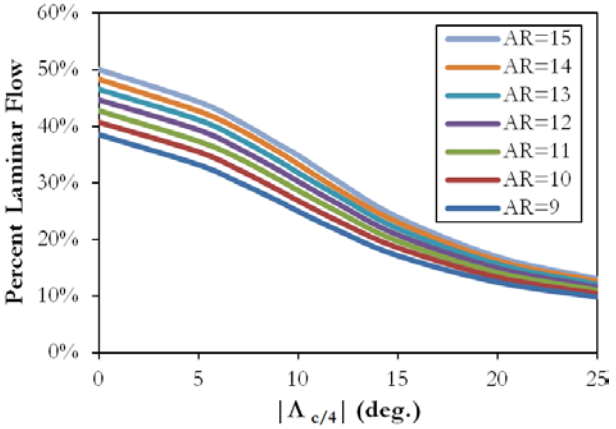

Fig. 16 Extent of Laminar Flow vs. Quarter Chord Sweep of the wing.

In order to perform this analysis, a dynamic spreadsheet was created to analyze typical design tradeoffs for swept forward configurations[32]. Using the result for the relationship between the extent of the laminar flow and the basic geometry of the aircraft, as well as the inherent geometric and performance sizing capabilities of this dynamic spreadsheet, a parametric analysis was performed in order to observe the effects of the changes in quarter chord sweep angle on the cruise L/D of the configuration. This parametric study was constrained similarly to the laminar flow analysis presented in Fig. 16 so as to preserve consistency. Figure 17 indicates that as the magnitude of the sweep angle increases, the cruise L/D increases. *Lehner et al.* present the argument that this occurs because the induced in-wash flow generated on the outboard sections of the wing has the potential to sustain larger areas of laminar flow. Susceptibility to flutter also increases with increasing sweep angle. Accordingly, UACC selected a sweep angle of -5.9° due to flutter induced structural limitations, as suggested by *Lehner et al.*

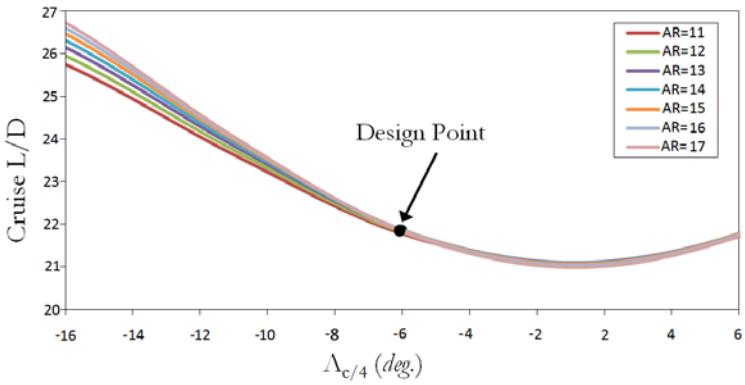

Fig. 17 Variation in cruise L/D as a result of changes in the sweep of the wing, performed using the dynamic spreadsheet. The design point is defined by susceptibility to flutter and divergence.

* This result also agrees with the suggestions made by *Lehner*[9] regarding normalization of the percentage laminar flow on wing surfaces.

4.5 Numerical Verification of Laminar Flow

To ensure that the wing geometry is capable of sustaining laminar flow on its upper and lower surface, two main elements are required. First, a favorable pressure gradient has to be maintained over a significant portion of the wing planform, starting at the leading edge. Second, no shock should exist in the region that laminar flow is expected to be maintained. To verify the capability of Levant's wing planform to satisfy these conditions, a transient CFD analysis of the flow field around the wing was performed using COSMOS FloWorks for which the results are presented in Figs. 18-20. From this analysis, it was concluded that a favorable pressure gradient (i.e. decreasing pressure in the streamwise direction of the flow) exists on the wing upper surface. The shock on the upper surface does not occur until the 80% chordwise station. The lower surface of the wing is shock free; however, the extent of favorable pressure gradient is smaller than the upper surface

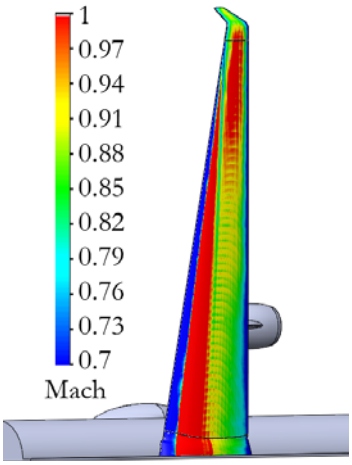

Fig. 18 Mach number contours adjacent to the upper surface of the wing

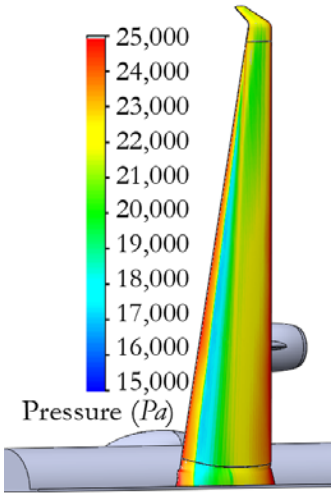

Fig. 19 Pressure contours adjacent to the upper surface of the wing

Figs. 18-20 Transient CFD analyses were performed using COSMOS FloWorks on the upper and lower surfaces of the wing to ensure the potential of the surfaces to maintain laminar flow along the chord. The initial conditions replicate ISA atmosphere at a Mach number of 0.8 at 35,000'.

As it can be seen from Figs. 19 and 20, a favorable pressure gradient exists along the chordwise direction on the wing. Figure 18 also confirms that there exist no shocks in the region extending from the leading edge to approximately 80% of the chord.

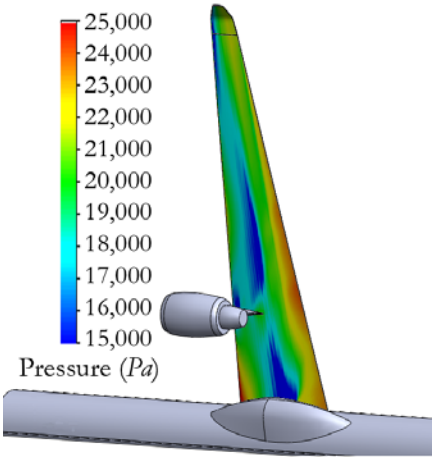

Fig. 20 Pressure contours adjacent to the lower surface of the wing

4.6 High Lift Device Sizing

The strategy to maintain maximum laminar flow on the wing surfaces dictated that no deployable part on the leading edge should be incorporated. This led to the decision to incorporate only the most efficient trailing edge devices that can generate a C_{Lmax} of 2.2, as was assumed in Sec. 3.4, given that the flap will extend to 75% of the wing half-span*. Reviewing the ESDU Data Item 95021[21], it was determined that a set of Fowler flaps would generate sufficient lift for this purpose. Using the *Roskam*[33] method for sizing flaps, a parametric study was performed to determine the required flap chord to wing chord ratio that will generate sufficient C_{Lmax} at takeoff. Figure 21 shows the results of this analysis for flaps having a streamwise extent between 15% and 35% of the wing chord. . Efforts were made to define the geometry of the flap segments to ensure attachment of fast moving air to the upper surface of each segment once the flaps are deployed. A low speed, transient CFD analysis was used to verify the attachment of flow at landing conditions with a flap deflection of 35°, the result of which can be seen in Fig. 22.

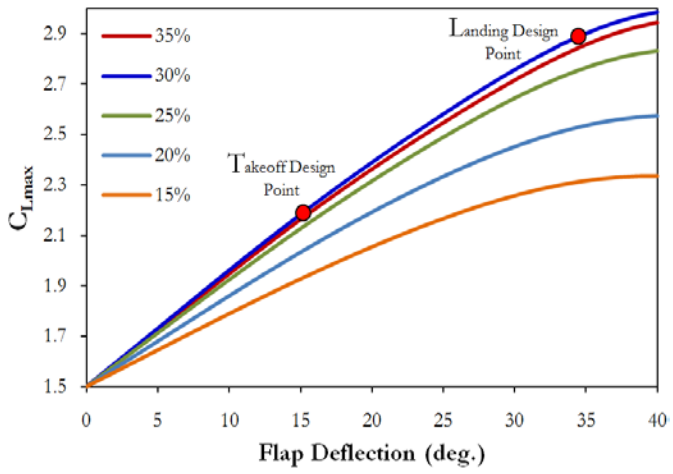

Fig. 21 Aircraft maximum lift coefficient vs. flap deflection for different flap chord to wing chord ratios. The takeoff position of 15° and landing flap setting of 35° is indicated.

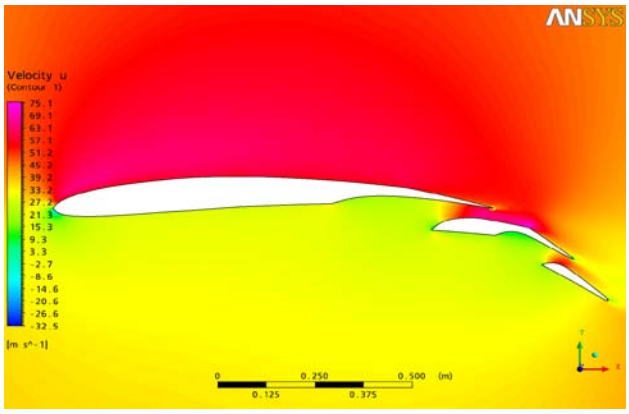

Fig. 22 CFD results for verification of flow attachment for fully deflected double slotted Fowler flap, performed using ANSYS CFX transient CFD model.

From Fig. 21, increasing the flap chord to wing chord ratio decreases the maximum C_L attained by the high lift device system above a flap chord to wing chord ratio of 30%; therefore, a 30% ratio was chosen. CFD analysis, presented in Fig. 22, was used to determine the wideness of the slot by performing geometric optimizations.

* As dictated by the location of the folding line on the wing

4.7 Detailed Drag Polars and Breakdown

To obtain a more accurate estimate of the lift and drag forces acting on the aircraft, a more detailed analysis of the aerodynamics of the aircraft was performed using the methods presented by *Roskam*[34]. The methodology used to determine cruise drag polars accounts for compressibility effects by taking advantage of the corrections presented in ESDU Transonic Aerodynamic Data Items[*]. The low speed drag polar methodology is adopted from *Torenbeek*[35]. The results of the CFD analysis related to the verification of the extent of laminar flow on the wing and fuselage, presented in Sec. 4.1 and 4.5, were used to compute the drag acting on the wing and fuselage at transonic speeds. It was assumed that all empennage surfaces would have 15% of their wetted area exposed to laminar flow. Figure 23 presents the results of detailed drag analysis using 5th order drag polar equations, which will be used later in Sec. 11.1-11.6 to verify the satisfaction of performance requirements. Figure 24 presents the drag breakdown of Levant at cruise conditions.

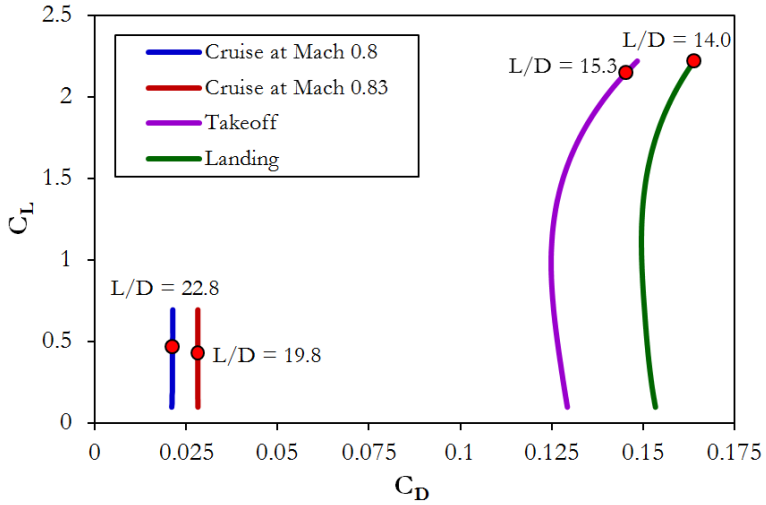

Fig. 23 5th order Drag Polars at Cruise, Max Cruise, Takeoff, and Landing Conditions.

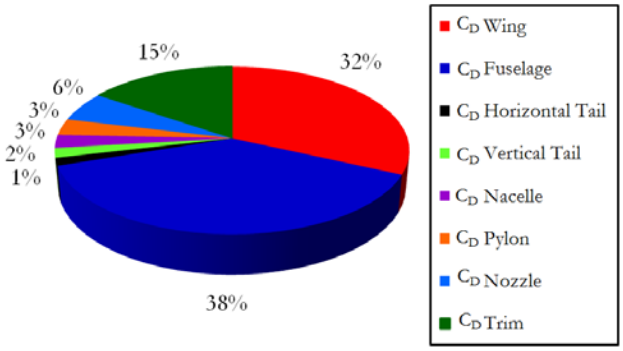

Fig. 24 Drag breakdown at cruise.

The drag polars for cruise and max speed conditions are computed using 5th order methodologies for a range of lift coefficients from 0.1-0.75. Higher lift coefficients were deemed unnecessary for cruise conditions. The lift coefficients selected for cruise, max speed, takeoff, and landing are 0.48, 0.46, 2.2, and 2.3 respectively. From the drag breakdown at cruise, it is observed that the drag of the wing constitutes 32% of the drag for the entire aircraft. This number is substantially lower than the conventional 50% wing drag at cruise, due to the utilization of NLF.

[*] The following data items have been used: 6407, 71019, 79004, and 83017

4.8 Drag Rise Characteristics

Given the low wing sweep resulting from planform optimization, it was critical to verify the drag divergence Mach number (M_{DD}) of the configuration. Drag rise analysis was performed using the method presented by *Roskam*.[36]. The M_{DD} was defined as the Mach number at which the rate of change of total drag of the aircraft exceeds 0.1. Figure 25 presents the results of this analysis.

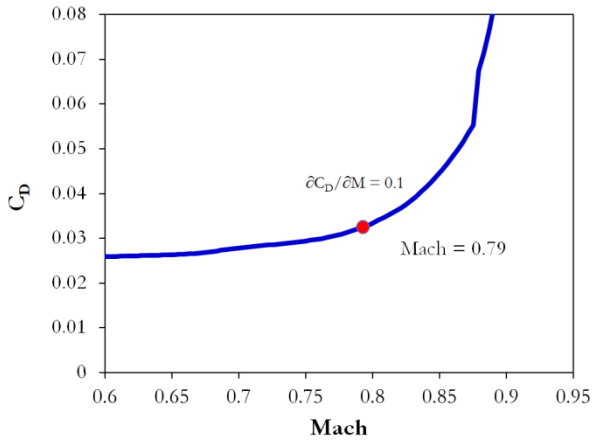

Fig. 25 Result of drag divergence analysis on Levant indicating a M_{DD} of 0.79, according to the criteria of $\partial C_D/\partial M$ of 0.1.

4.9 Drag Verification

To verify the accuracy of the methodology used to model the high speed drag of Levant, experimental data was obtained with regard to the high speed aerodynamic performance of the DC-10-40[37]. This data was compared to the results of a case study analysis of the DC-10-40 using the drag estimation methods of Levant. Figure 26 (on the following page) presents this comparison. As it can be seen, the drag polars intersect in the neighborhood of $C_L = 0.5$, indicating the agreement of *Roskam*'s method with experimental data at typical cruise lift coefficients.

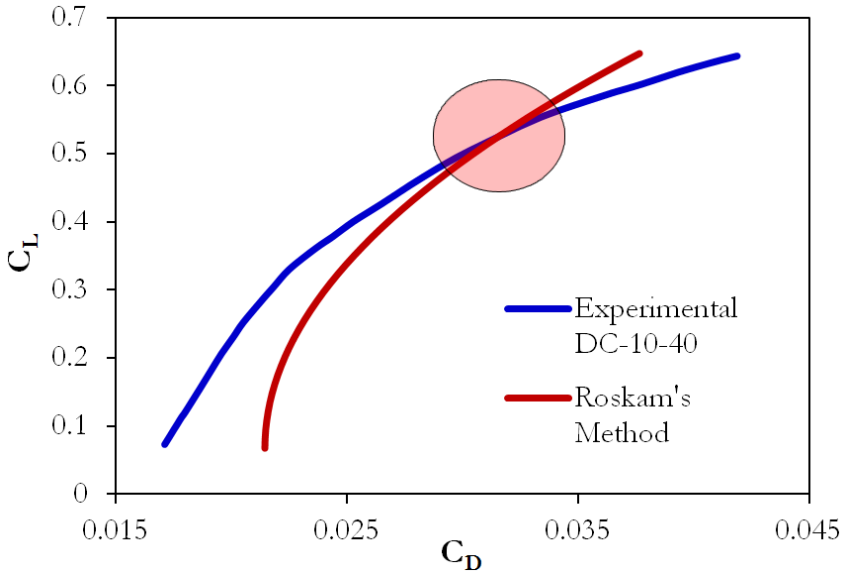

Fig. 26 Comparison of experimental data regarding the lift and drag characteristics of the DC-10-40 with results obtained by applying *Roskam's* method to estimate drag.

5. Propulsion

5.1 Engine Technology Tradeoff

Levant's propulsion system was especially designed to satisfy the RFP's guidelines regarding environmental footprint, fuel burn, and aircraft operating cost. Two main available propulsion technologies were explored during initial configuration design: GTF and open fan engines. Modern turbofan technologies, including GTFs, such as the Pratt and Whitney PW1000G, and direct drive fans, such as CFM's LEAP-X, were explored to observe their benefits and drawbacks. Advanced turbofan technology presents fewer development risks within the timeframe set by the RFP[38], but arguably represents today's propulsion technology rather than that of an aircraft entering service in 2020.

Based on the sensitivity analysis performed earlier during the project, it was concluded that the type of engine and its method of integration would play a major role in improving Levant's fuel efficiency, acoustic characteristics, and environmental impact. UACC researched different variations of three main engine types: unducted rotors, GTFs, and advanced direct-drive three-spool turbofans. Given the "under development" status of most of the concepts studied, assumptions were made in order to make the analysis of each power plant possible. Available drawings and cutaway views published for advertising purposes were analyzed and used to obtain basic parameters regarding the turbomechanical configuration of each engine, such as the number of stages and approximate dimensions. GasTurb* was the software of choice for propulsion analysis and was used to determine the main performance characteristics of each engine and compare the different powerplant options. In addition to performance and environmental analysis performed using GasTurb, basic risk and feasibility considerations were also influential in choosing the engine. Measures of merit and selection strategies developed by *Bonnacorsi et al.*[39] were used to narrow down the selection domain by integrating multiple performance characteristics and empirical market

* Developed by Joachim Kurzke, U.S. Distributor: Concept NREC, MA

preferences into the selection strategy. In the following sections, a brief description of each of the concepts and the result of the performed analysis is presented.

5.2 Unducted Rotor Concept

The unducted rotor (or open fan) concept is basically a modified turbofan engine, with the fan blades placed outside of the engine nacelle on the same axis as the compressor blades. Open fans are known to possess extremely high BPRs, offering the speed and performance of a turbofan with the fuel economy of a turboprop engine. This concept has also been subjected to substantial experimental studies. The NASA Propfan Test Assessment project is a remarkable example of these studies, and the official reports of the project[40] indicate considerable potential for implementation of the open fan concept into modern day commercial aircraft. Snecma and Rolls-Royce have both invested in unducted rotors with an estimated reduction in TSFC of 20%, and the Airbus NSR* project has shown willingness to utilize these engines in their design.[41]

Despite the enormous advantages in fuel economy, open fans are known to generate incredibly high noise levels due to the sonic speed induced in the flow field around the external fans. Reducing the far and near field noise of an open-rotor has been the subject of many research efforts, most notably the extensive research performed by NASA[35] and by *Holste et al.*[42] from the Institute for Advancement in Flight. After much investigation, *Holste* concludes that the possible reduction in the source noise as a result of blade optimization and improved turbo machinery does not exceed 10 *dB* due to the extremely high flow speeds generated by the fan. It is notable that the Airbus NSR project has been dealing with substantial issues in fields of acoustics of open-rotor engines. Using a Rolls-Royce RB3011 open fan, it is believed that the engine, without any suppression effects from the fuselage and empennage, will hardly satisfy the ICAO Chapter-4 noise requirements. Other than noise, the open rotor concepts are believed to face major reliability challenges because they mount the blades on a hot rotating structure around the engine's exhaust end, exposing it to possible heat

* New Short Range Project intending to replace the A320 series by 2018

fatigue.[38] Also, other issues such as the containment of lost blades present a serious configuration challenge, which is usually addressed by applying armor plating on the aft fuselage. *Garber* mentions the installation of 700 *lbs.* of 3/8" stainless steel armor plating as a method of blade containment on the fuselage of the Gulfstream II prototype used by NASA to test the initial open-rotor concepts.[43] A protective armored system for a commercial transport plane is expected to weigh substantially more while also being less effective. All the aforementioned issues have caused Rolls-Royce and Snecma to push back the EIS of their open rotor engines to 2020,[44] in order to allow more time for improving the engine characteristics, reliability, and safety. Given the significant financial risks associated with the application of an open rotor concept, and availability of safer options for the power plant, this concept was not chosen for the development of Levant.

5.3 Advanced Direct Drive and GTFs

In the design of Levant, emissions were particularly important to consider, given the possible introduction of carbon taxation in the near future. It has been suggested that such taxation would be implemented as a part of the tax imposed on the sale of aviation fuel, increasing the cost of operators of high-emission aircraft. The future market will thus be financially motivated to procure lower emission aircraft.

UACC has addressed the market demands concerning low emission aircraft by using more advanced propulsion technology, flight path optimization, alternative fuels, and general range performance enhancements. Given the challenges faced by the open-rotor concept, modified turbofan engines present a considerable potential for utilization in the next generation of short to medium range aircraft. Two main commercial engines under development were considered to power Levant: Pratt & Whitney PW1000G GTF and CFM Leap-X direct drive turbofan, which are both capable of satisfying the requirements for maximum Sea Level Static Thrust (SLST). Only scarce information is currently available due to the proprietary nature of the performance of these two engines. Considering a conventional turbofan configuration, and mindful of the claims made by

P&W and CFM, a parametric study was performed to observe the effects of the changes in BPR on the MTOGW and the block fuel burn for the aircraft flying a 3,500 *nm.* cruise mission. The results of this investigation are presented in Fig. 27. It was concluded that when using a direct drive turbofan and an AR of 14.1 for the wing, a BPR of eight is the optimum configuration for a conventional turbofan engine*. This result confirms the unofficial reports regarding the BPR of the under development CFM Leap-X engine believed to have a BPR of approximately eight[45]. Assuming a three-spool engine core configuration with a SLST of 22,000 *lbs.* a GasTurb model of the engine was constructed by defining the approximate geometry of the Leap-X engine and applying the efficiencies computed by the software to obtain a BPR of eight. Figures 28 and 29 present the cross-section of the constructed GasTurb model for the high BPR direct drive turbofan in the mixed and unmixed flow configurations. Cross-section of both mixed-flow and unmixed-flow high bypass ratio turbofans were modeled using GasTurb, based on the basic parameters obtained through analyzing pictures and cut-away views of the CFM Leap-X engine. Diameter of the engine was measured to be approximately 70**".**

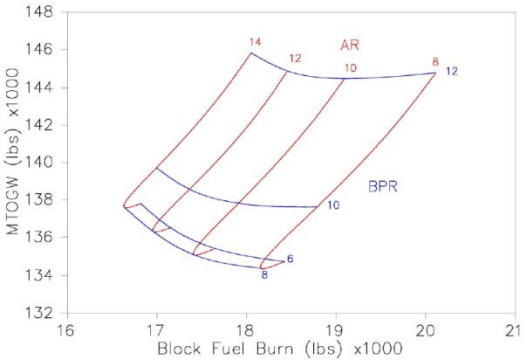

Fig. 27 MTOGW vs. Block Fuel Burn for different AR and BPR (M=0.8, ICA=38,00')

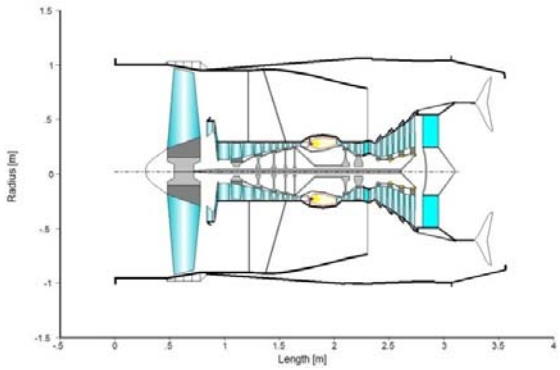

Fig. 28 General arrangement cross-section of the mixed flow high BPR direct drive turbofan concept investigated

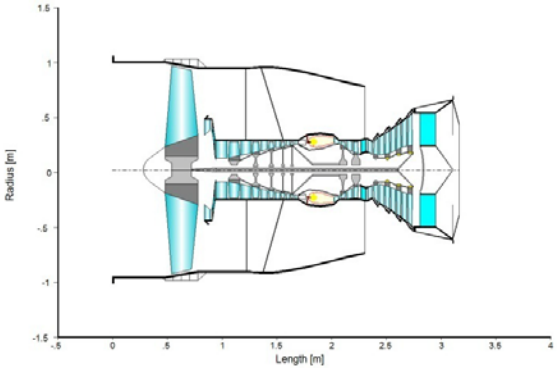

Fig. 29 General arrangement cross-section of the un-mixed flow high BPR direct drive turbofan

* The non-monotonic behavior is attributed to the increased weight of the direct drive turbofan engine and the nacelle associated with them, as projected by the JetSizer propulsion module.

An engine map was constructed from parametric studies that were performed that identified the thrust and TSFC characteristics of these two configurations. Instead of having bleed air taken from the engine, the analysis estimated an increased power extraction of 250 *kW* by the accessories and gearbox installed on the engine. The NOx Severity Index was chosen as the measure of merit in assessing the environmental effects. This parameter, presented by the Committee of Aeronautical Technologies[46] is defined as:

$$S_{NO_x} = \left(\frac{P_3}{2{,}965 kPa} \right)^{0.4} e^{\left(\frac{T_3 - 826K}{194K} + \frac{6.29 - 100\,war}{53.2} \right)} \qquad (2)$$

where P_3 and T_3 are pressure and temperature inside the combustor of the engine and *war* denotes the liquid water to air ratio of the air entering the combustion chamber. NOx Severity Index was chosen mainly due to the emphasis placed on the role of NOx in the destruction of the ozone layer by *Schwartz et al.*[47] In their extensive study of the effects of different emitted gasses, *Schwartz et al.* concluded that NOx emissions are the most significant contributors to the destruction of the ozone layer. Results of the NOx severity analysis were combined with the result of the engine performance analysis to visualize the trend between engine performance and environmental impacts. Figures 30 and 31 (on the following page) present the results of the analysis for both mixed and unmixed flow direct drive concepts.

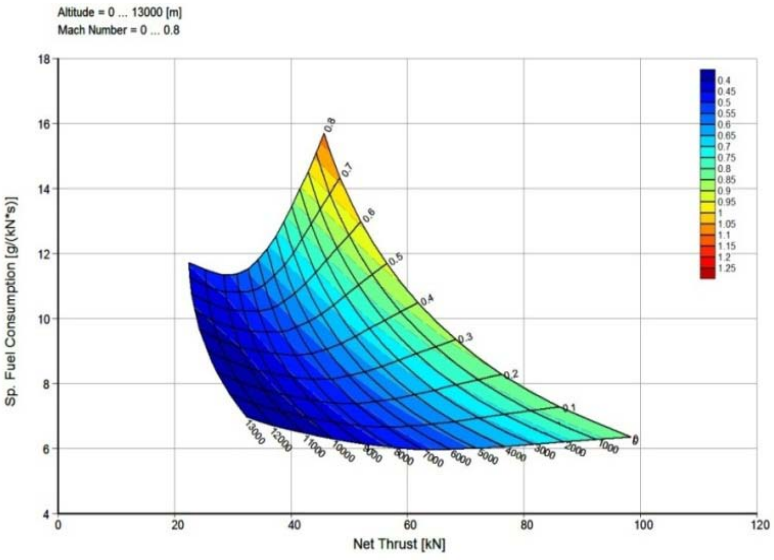

Fig. 30 Installed engine map for direct drive, unmixed flow high BPR turbofan. NOx Severity index is plotted as a color contour indicating the areas of high emission levels with bright colors. At cruise condition (M=0.8/38,000') SFC is equal to 0.44 *lb./lb.-hr*, and installed thrust is equal to 4,500 *lbs* NO_x severity parameter for cruise at 38,000' and 0.8 Mach is equal to 0.55

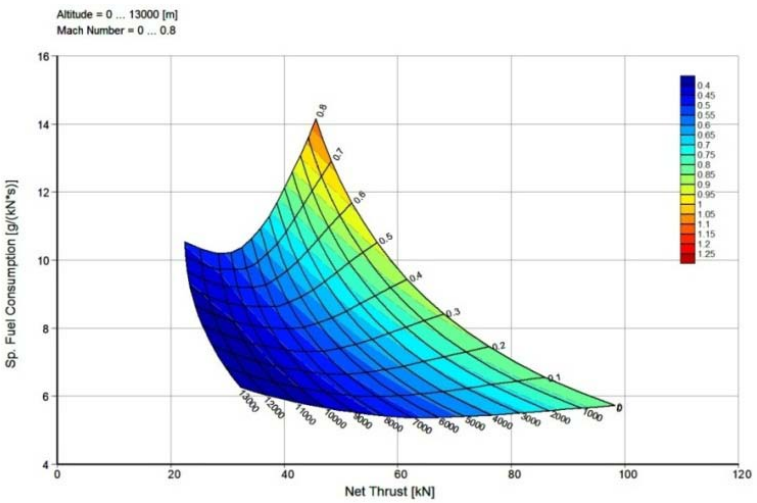

Fig. 31 Installed engine map for direct drive, mixed-flow high BPR turbofan. NO_x Severity index is plotted as a color contour indicating the areas of high emission levels with bright colors At cruise condition (M=0.8/38,000') SFC is equal to 0.40 *lb./lb.-hr*, and installed thrust is equal to 4,400 *lbs.* NO_x severity parameter for cruise at 38,000' and 0.8 Mach is equal to 0.55.

The PW1000G, a GTF similar to the advanced direct drive turbofans, was modeled using GasTurb based on the released cutaway views[48]. Parameters regarding the efficiencies of the gearbox, the high and low pressure compressors, and the high and low pressure turbines were varied to obtain an engine with an SLST of 22,000 *lbs*. This engine was also studied in two configurations of mixed and unmixed duct flow, for which the general arrangements are shown in Figs. 32 and 33.

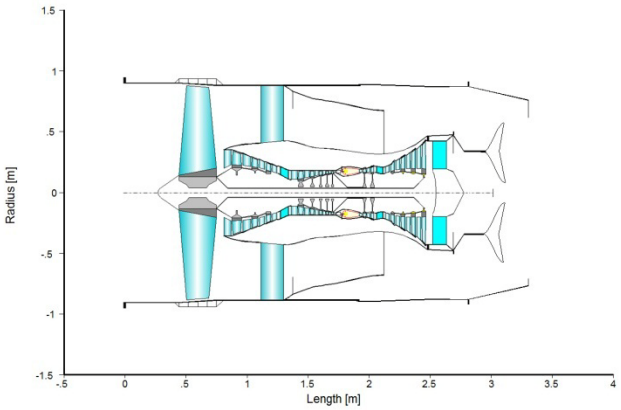

Fig. 32 General arrangement cross-section of the mixed flow geared turbofan concept investigated

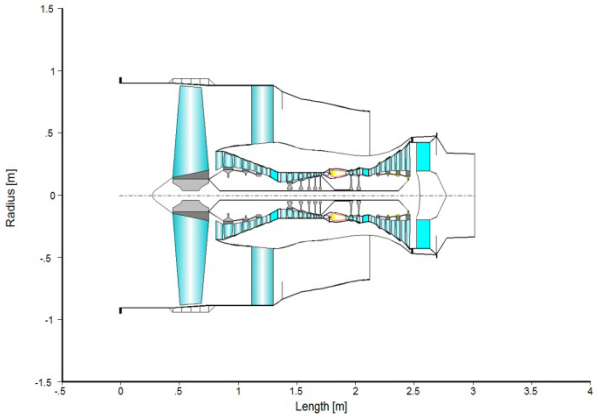

Fig. 33 General arrangement cross-section of the un-mixed flow geared turbofan concept investigated

Cross-section of both mixed-flow and unmixed-flow geared turbofans were modeled using Gasturb, based on the basic parameters obtained through analyzing the cut-away view of the PW1000G. Diameter of the engine was measured to be approximately 75".

Analysis of these concepts indicated that the engines with a gear ratio of 4 had a BPR of approximately 10. It should be noted that the trade study performed prior to the engine selection processes presented in Fig. 27 does not apply to a GTF, and the BPR of 10 obtained for the GTF thus cannot be regarded as non-optimal. Results of this analysis can be seen in Figs. 34 and 35.

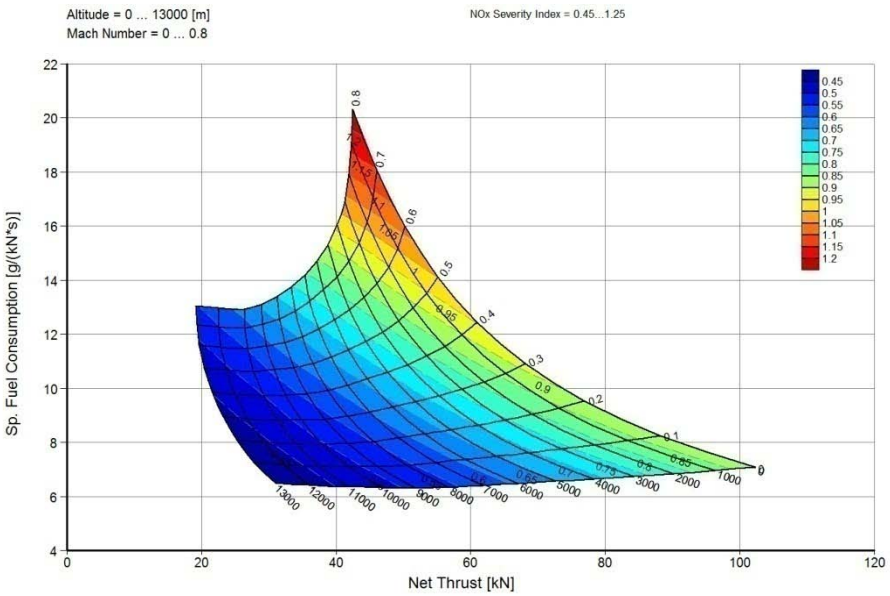

Fig. 34 Installed engine map for, <u>unmixed-flow</u> geared turbofan. NO_x Severity index is plotted as a color contour indicating the areas of high emission levels with bright colors. At cruise condition (M=0.8/38,000') SFC is equal to 0.45 lbm./lbf.hr, and installed thrust is equal to 4400 lbs NO_x severity parameter for cruise at 38,000' and 0.8 Mach is equal to 0.55.

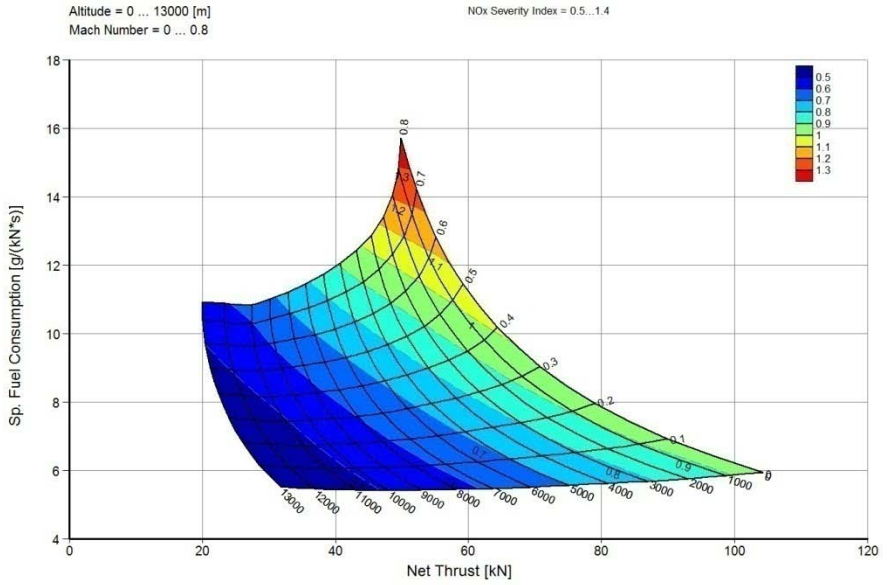

Fig. 35. Installed engine map for <u>mixed-flow</u> geared turbofan. NO_x Severity index is plotted as a color contour indicating the areas of high emission levels with bright colors At cruise condition (M=0.8/38000 ft) SFC is equal to 0.41 *lb./lb.-hr.*, and installed thrust is equal to 4,400 *lbs*. NO_x severity parameter for cruise at 38000' and 0.8 Mach is equal to 0.55.

The results of these analyses indicate that the NOx severity parameter values are similar for both geared and direct drive turbofan engines during cruise. It was also concluded that the type of the by-pass flow (mixed and unmixed) has a significant effect on the fuel consumption of both types of engines, with a more significant impact on the GTFs. Since both geared and advanced direct drive concepts attain approximately the same fuel consumption and thrust characteristics during cruise, noise and feasibility considerations became critical in engine selection. The Pratt & Whitney GTF, which has already started the testing process and was selected as the engine for the Mitsubishi Regional Jet and Bombardier C-Series, faces fewer technical challenges and development delays.

Therefore, the concept presents less financial risk for Levant. Also, given the lower rotation speed of the main fan due to the implementation of the epicyclical gear system, the GTF will produce less fan noise. All these factors led UACC to select the Pratt & Whitney PW1000G GTF in a mixed flow configuration.

Additionally, emphasis was placed on optimizing the flight path of the aircraft[49] in order to reduce the fuel burn and corresponding emission levels by accurately determining the optimum cruise Mach number and altitude (within the range specified by the RFP). Utilizing modern structure and NLF technology contributed to reductions in weight and an increase in the L/D of Levant, consequently providing a significant reduction in the fuel burn and emissions of the aircraft.

5.4 Engine-Wing Integration

The inlet for the engine was designed by applying the method presented by *Seddon et al.*[50] in order to achieve a full pressure recovery at the fan station of the engine. Trade studies were performed to observe the effects of duct length and inlet cross-section area on inlet pressure recovery, and to determine the shortest length and smallest cross-section area for the inlet of the utilized engine. This trade study, the cross-section of the inlet, and the mixed flow nacelle designed for Levant are shown in Figs. 36 and 37 below.

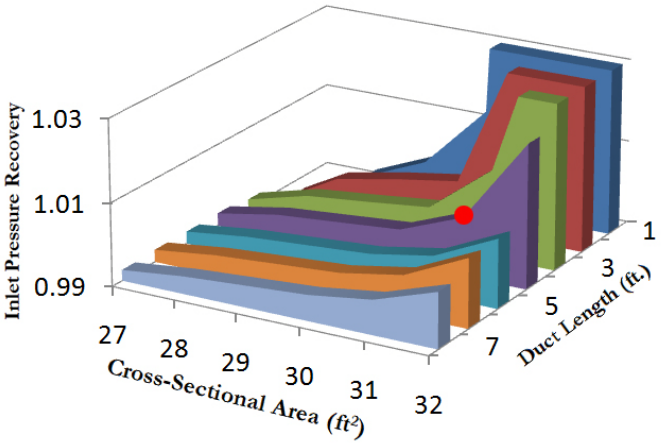

Fig. 36. Intake geometric trade study, showing the design point

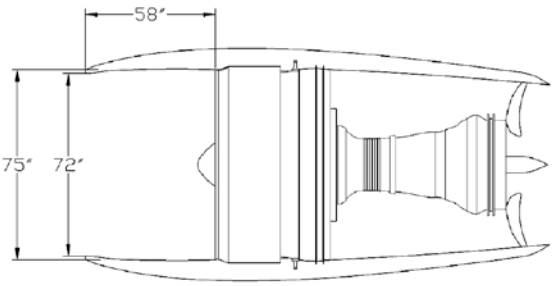

Fig. 37. Intake Geometry using a fully mixed flow nacelle

5.5 Bleedless Architecture

As stated by *Collie et al.*[51], the fuel burn of high BPR, small core engines can be significantly reduced by eliminating their bleed air system. Removing this system from the high pressure compressor stage can significantly improve local compressor efficiencies. Analysis using GasTurb was used to model the effects of the variations of the overboard bleed mass flow on the TSFC of the engine, the results of which can be seen in Fig. 38. By reducing the overboard bleed mass flow from five to zero *lb/sec*, the TSFC varies significantly from 0.485 to 0.454 *lb/(lb-hr)* (causing a 6% reduction). Because of this substantial reduction in TSFC, a bleedless architecture was integrated into Levant.

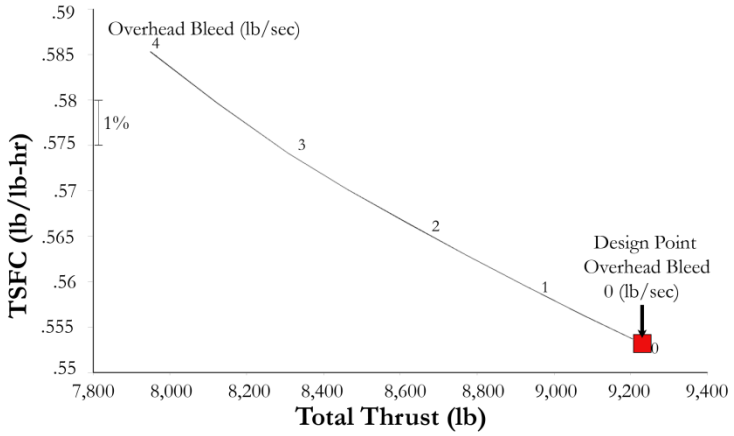

Fig. 38 TSFC vs. total thrust at mass flow overhead bleeds from four to zero *lb/sec*. Design point suggests minimal TSFC at no overhead bleed

5.6 Emissions

In the design of Levant, emissions were particularly important to consider, given the possible introduction of carbon taxation in the near future. It has been suggested that such taxation would be implemented as a part of the tax imposed on the sale of aviation fuel, increasing the cost of fuel for operators of high-emission aircraft. The future market will thus be financially motivated to procure lower emission aircraft.

UACC has addressed the market demands concerning low emission aircraft by using more advanced propulsion technology, flight path optimization, alternative fuels, and general range performance enhancements. Engine design parameter optimization was performed in order to minimize the cumulative effect of NOx emissions and fuel burn of the aircraft on the environmental

footprint of Levant. The NOx intensity factor was chosen as a measure of merit for the production of NOx emissions, as defined by the Committee of Aeronautical Technologies,[52] and is presented in Equation 3,

$$S_{NO_x} = \left(\frac{P_3}{2965kPa} \right)^{0.4} e^{\left(\frac{T_3 - 826K}{194K} + \frac{6.29 - 100\,war}{53.2} \right)} \quad . \tag{3}$$

An analysis was performed using GasTurb to evaluate the NOx severity factor over the flight envelope of the engine of the aircraft, the result of which is shown in Fig. 39.

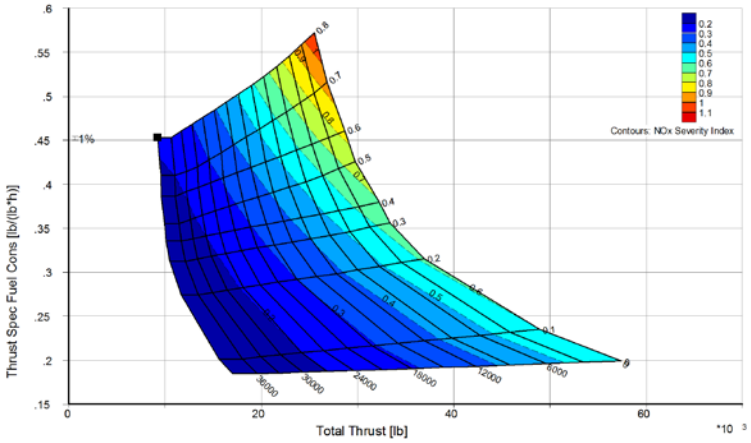

Fig. 39 NOx intensity contours plotted over engine performance map

From this analysis, it was determined that 5.75 grams of NOx is generated per every kilogram of fuel burned at 39,000' altitude. Emphasis was placed on optimizing the flight path of the aircraft[53] in order to reduce the fuel burn and corresponding emission levels by accurately determining the optimum cruise Mach number and altitude (within the range specified by the RFP). Utilizing modern structure and NLF technology contributed to reductions in takeoff weight and an increase in the cruise L/D of Levant, consequently providing a significant reduction in the fuel burn and emissions of the aircraft.

6. Systems Integration

6.1 Electrical Distribution System

Commercial aircraft are gradually replacing hydraulic and pneumatic subsystems with lighter, cleaner, and more efficient electrical architecture*,[54]. The Levant is engineered to take advantage of this potential for simpler, safer, and more fuel efficient, electrically dominant aircraft subsystems. Six starters/generators (two per engine and two on the APU) provide an estimated 740 kW to the subsystems of Levant, based on the power consumption trends of commercial aircraft over the last two decades[55]. Each starter/generator provides a three-phase, variable frequency 230 V_{AC} to the aft electrical/electronics (E/E) bay, where 230 V_{AC}, 115 V_{AC}, and 28 V_{DC} loads are controlled by computer managed Remote Power Distribution Units (RPMUs). An additional ± 270 V_{DC} is used within the liquid cooled electrical distribution power cabinets located in the forward and aft E/E bays[56]. The larger and innovative 230 V_{AC} and ± 270 V_{DC} satisfy the needs of the higher power consumption systems, such as the electrical environmental control and pressurization system. The smaller 115 V_{AC} and 28 V_{DC} are required for traditional electrical subsystems, such as lighting and galley operations. Figure 40 demonstrates the basic power distribution hierarchy used by Levant. More detail regarding the electrical distribution system can be found in the accompanying large scale drawing SY – 3.0.

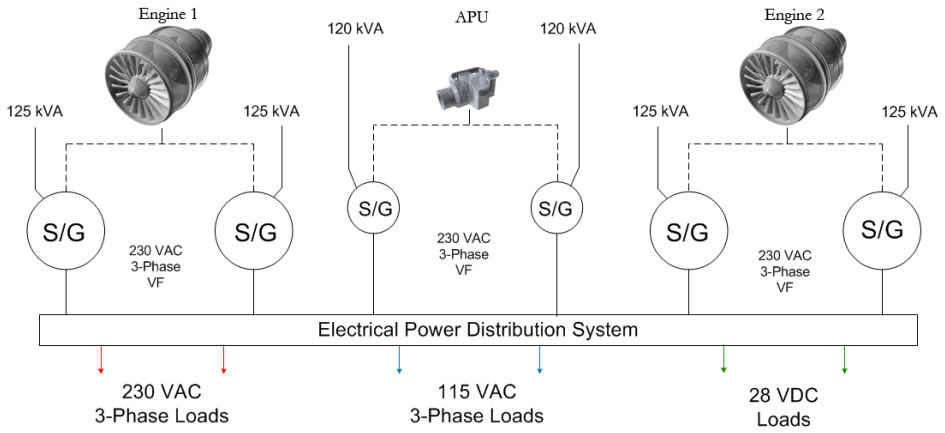

Fig. 40 Electrical power generation architecture. S/G denotes starter/generator units installed on the engines and APU. V/F denotes variable frequency.

* The Levant generates 250 kW per channel via its starters/generators. Comparatively, the Boeing 747-400 produces 120 kW and the Boeing 787 produces 500 kW per channel. The Boeing 787 is unique in that it is the first jetliner to incorporate a bleedless architecture and thus requires large amounts of electrical power. Similarly, the Levant's electrical systems that replace its hydraulic and pneumatic functions require greater amounts of electrical power compared against other aircraft in its class.

6.2 Electrical Pressurization and Environmental Control System

UACC has fashioned Levant's electrical pressurization and environmental control system (ECS) after the Boeing 787 bleedless architecture. Considering that Levant contains half the payload of the Boeing 787, UACC projects that the ECS and pressurization systems will require 250 *kW* of electrical power, as compared to the 500 *kW* for the Boeing 787[57]. The all electric environmental control system integrated into Levant takes advantage of greater fuel efficiency by nearly eliminating bleed air and thus reducing the weight associated with traditional bleed air architecture. Ram-air inlets and variable speed, electrically driven compressors allow Levant to expend only as much energy as required to pressurize and ventilate the cabin[58]. In a bleedless architecture[59], energy is not leached from the engine's thrust, improving the TSFC of the engine, whereas traditional bleed architecture would have adverse impacts on engine performance. Once compressed, the hot air from the electrical compressors mixes with the cool air in the mixing chamber before being distributed throughout the aircraft, as seen in Fig 41. The avionics equipment utilizes the aircraft's cool skin surface temperature and the flight deck's conditioned, uncirculated air to dissipate excess heat. Conditioned air is mixed with filtered, recirculated cabin air after passing through the dual environmental control system packs. Air that is circulated to the cabin returns to the mixing chamber via the forward cargo bay. More detail regarding the electric air conditioning system can be found in the accompanying large scale drawing SY – 2.0.

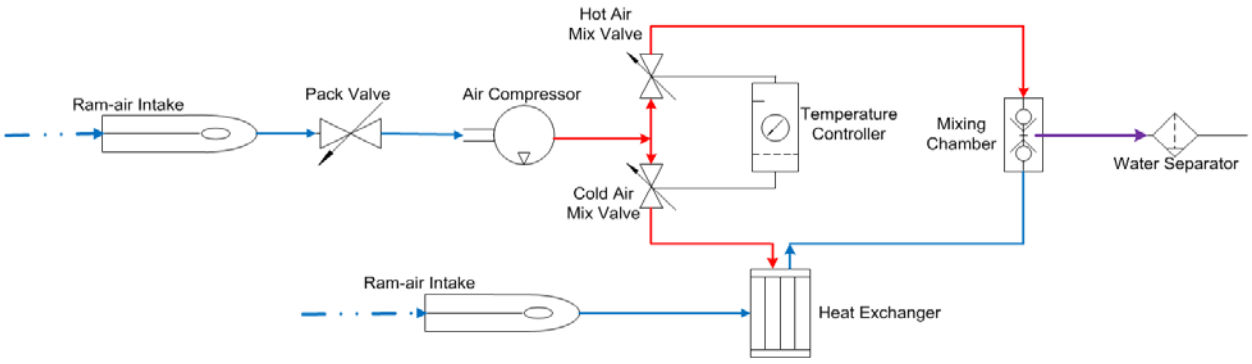

Fig. 41 Air conditioning pack flow diagram. Notice that the recirculation/filtration system is not shown here to be concise.

6.3 Electrical Flight Controls System

The Levant employs a historically novel flight control system that replaces traditional hydraulic systems with electro-mechanical actuators. The placement of the actuators on the wing surfaces is shown in Fig. 42. The unique fly-by-wire and power-by-wire systems are operated in conjunction with three Primary Flight Control Computers (PFCCs) and two airplane information management computers. The "pipelines" through which the system communicates are composed of a triple redundant, high bandwidth fiber optic network. Pilot inputs are converted into primary and secondary control surface movements through the PFCCs. Once the input is calculated by the PFCCs, commands are sent to the Actuator Control Electrics units (ACE). The ACE units control the movement of the actuators in the spoilers, flaperons, tailplane horizontal stabilizer, elevators, and rudder. The ACE units also receive feedback information on the actuator positions, which is sent back to the PFCCs for further processing. In landing and takeoff conditions, the flap positions are controlled by redundant Flap Electronics Units, which communicate with three Autopilot & Flight Director Computers, while the flaperons are controlled directly by the ACEs and PFCCs. The flight control system loop is completed when the pilots receive tactile feedback via "feel" actuators located in the flight deck. A major advantage of this all-electromechanical system is that it reduces weight by replacing traditional hydraulic systems[60]. Additionally, maintenance is simplified because individual actuators can be replaced without draining hydraulic fluid, which increases the aircraft's utilization time[61]. More detail regarding the electrical flight controls can be found in the accompanying large scale drawing SY – 4.0.

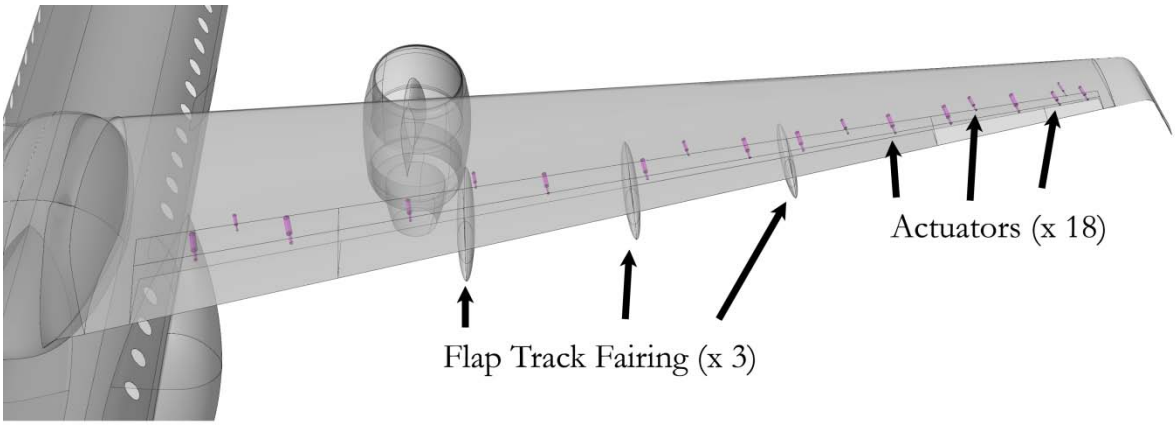

Fig. 42 Location of control surface actuators and flap track fairings

6.4 Landing Gear/Tire Spray

The nose landing gear is of the self-contained hydraulic shock absorber type and is equipped with a steer-by-wire system that is actuated electrically by a link to cockpit controls. It is retracted forward by a drag-brace-member that is electrically actuated. Nose landing gear doors are mechanically linked to the system to allow deployment. The large portion of the nose landing gear bay is sealed by the landing gear doors to reduce the airframe noise and drag of the aircraft and is only opened during the retraction/deployment process. Figure 43 presents the nose landing gear integration. The main landing gear is installed in a dedicated landing gear pod blended to the fuselage. The main landing gear bay has outboard and inboard doors, the latter of which is closed except during the retraction/deployment process to reduce airframe noise and drag. The doors are operated by electric motors and the retraction/deployment mechanism is done through a side brace electric actuator. Main shock absorption is done using a self-contained hydraulic oleo. Both the main and nose landing gears can be mechanically unlocked; therefore, allowing them to fall onto their own weight and achieve down lock as a result of kinematic air pressure acting on their surfaces. Using the method presented by ESDU Data Item 83042[62], the maximum depth of contaminates on the surface of the runway, at which the takeoff of the aircraft will be impacted by the impinging tire spray released from the nose landing gear, was determined to be 3/8", corresponding to a side spray elevation angle and a plan view angle of 14º each.

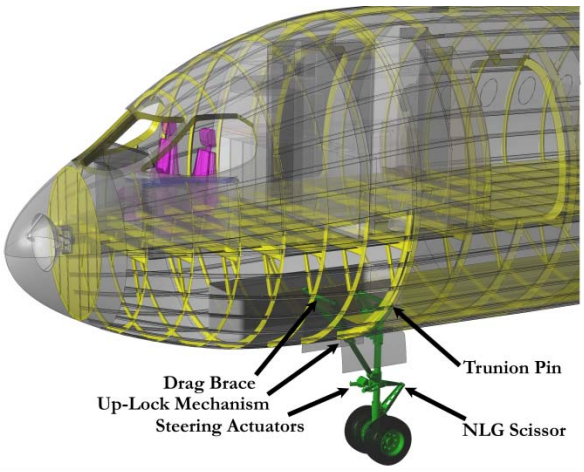

Fig. 43 Nose landing gear

Tire spray analysis was performed in order to determine the compatibility of the engine installation configuration with a spray pattern that could potentially damage the engine core or fan blades if it contains mud or ice. Notice that the critical design case will not be the occasional exposure to this material, rather a continuous occurrence of foreign object debris ingestion.

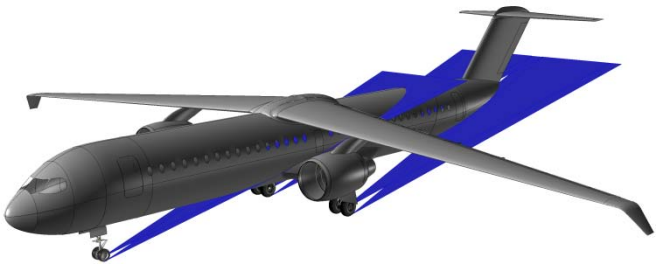

Fig. 44 Tire spray analysis results

6.5 Avionics and Cockpit Integration

The main avionics and computational task are performed by two Aircraft Information Management Computers (AIMCs). Communication with the Data Localizing Units (DLUs) and the Remote Power Management Units (RPMUs) is performed by the redundant, high speed, fiber optic information network. The DLUs gather analogue, digital, and serial data from remote avionics and aircraft systems sensors. The RPMUs control and distribute power loads from electrical cabinets located in the forebody and mid fuselage sections based on information received from remote hardware. That information is processed by the AIMCs and fed into the cockpit instrument panel. The location of the E/E bays is shown in Fig. 45. There are five 15" diagonal main display units in addition to two Multi-Function Interactive Display Units (MIDUs). Both the pilot and first officer have individual Head Up Displays (HUD) with their own control units located in the mid console beneath the landing gear lever. Information displayed on the HUDs and five main displays can be customized according to the pilot and first officer's preferences. More detail regarding the instrumentation of the cockpit can be found in the accompanying large scale drawing SY – 7.0.

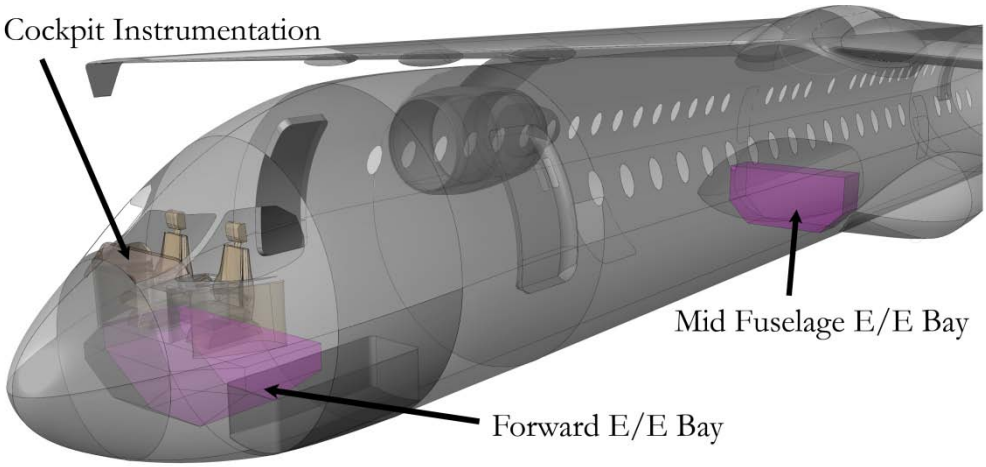

Fig. 45 Location of E/E bays along with Cockpit Instrumentation

6.6 Fuel System

The Levant's fuel system is comprised of three main fuel tanks, each supplying the engines with two fuel pumps, located in the wings and upper center fuselage. In the event of any one or two fuel tank failures, the aircraft can maintain operation through a single fuel supply pump. Once at cruise altitude, engines are suction-fed and fuel pumps can be turned off, reducing energy requirements during flight. Levant is also equipped with a fuel jettison system that can quickly dump fuel through valves located in the outboard wings in the event of a need for a rapid emergency landing, therefore reducing the landing weight of the aircraft so that landing gear structure remains intact.

6.7 Inert Gas Generation System

Safe oxygen levels in the fuel tanks have been more rigorously enforced in the 21th century since the 1996 Trans World Airlines Flight 800*. Oxygen in the fuel tanks is a potential explosive hazard that becomes more and more dangerous as the empty space in the fuel tanks increases. Considering this safety hazard, the fuel vapor-laden volume within the wing and center tanks (also known as ullage) is replaced by a 95% nitrogen rich gas until the oxygen levels are between 9% - 12%†. The Levant's inert gas generation system collects air from the plane's underbelly space via pumps. The air is then compressed using an electric motor and the Air Separation Module (ASM) membrane separates the oxygen from the rest of the gas. The now nitrogen rich gas is pumped into the fuel tanks to reduce the oxygen content of the respective ullages to 12% levels. Figure 46 presents the inert gas generation system.

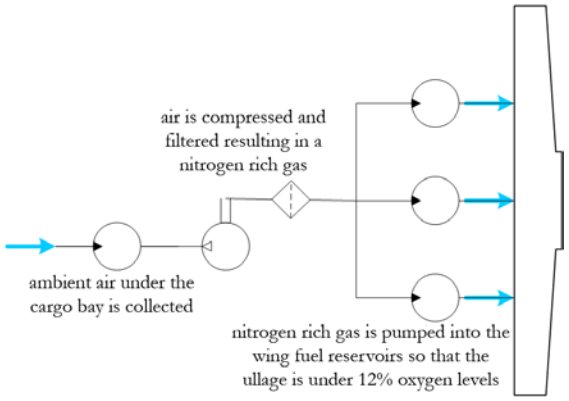

Fig. 46 The architecture of the inert gas generation system providing a nitrogen-rich gas mixture to wing fuel tanks

* TWA Flight 800 in 1996 was an airplane disaster off the coast of Long Island. It is speculated that unsafe oxygen levels in the fuel tanks led to a catastrophic explosion.
† For reference, combustion is not considered possible below 9% oxygen levels. The standard for commercial aviation fuel safety is 12%, at which the chances for combustion are significantly reduced. Atmospheric air has an oxygen level of 21%.

6.8 Auxiliary Power Unit Integration

To provide the power needs of the aircraft on the runway, as well as to supply the aircraft's power grid at the instances of significant power use, an Auxiliary Power Unit (APU) was integrated into the tailcone. This system was equipped with two 120 *kW* alternating current, three phase, variable frequency generators producing the electric power needed by the grid. The APU fuel flow is provided from the central wing tank through a dedicated pump/valve system. Given the proximity of the location of the installation of the APU to the empennage of the aircraft, and in compliance with FAR §25.903, the vertical tail was equipped with a three spar structure to ensure the redundancy in case of a blade loss occurring at the APU. The APU's exhaust is directed to a muffler via high temperature resistant ducting, and after suppression it is disposed of at the apsis of the tailcone contributing towards reducing the intensity of the fuselage wake. Figure 47 presents the location of the installation of the APU and the recommended zones by FAR §25.903 for clearance maintained from the critical structure of the vertical tail.

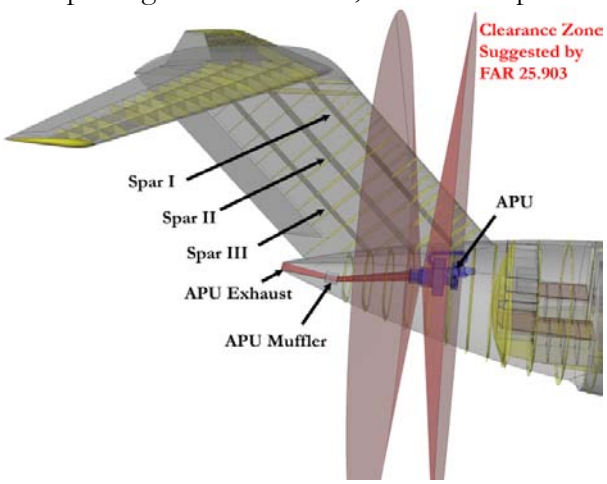

Fig. 47 APU installation showing the FAR §25.903 clearance zone for turbine equipment. In the event of turbine blade loss, there are at least two spars to keep the empennage intact.

6.9 Lightning Protection

Since Levant uses composite structures which are non-conductive material, there exists a need to implement a mesh of highly conductive material to conduct electricity near the surfaces of the aircraft in the event of a lightning strike. Due to machine-aided process used in manufacturing Levant, such conducted mesh can be laid during the process of manufacturing of the composite outer skins. If such a system is not implemented, local accumulation of charge on the non-conductive fuselage during a lightning strike will cause structural melting and significant damage near the location of lightning impingement.

6.10 Water & Waste Management

The waste and water system distributes, stores, and disposes of potable and black water between the galleys, lavatories, storage tanks, and service ports. The potable water is pressurized by an electric pump and distributed to the galleys and lavatories from a 200 L storage tank located behind the aft cargo compartment. Due to the possibility of the operation of the aircraft in the areas in which the potable water contains bacterial and mineral contamination, Levant was designed with a water filtration system. Water running through the potable water lines is filtered continuously by a dedicated water pump and filtration unit and is returned to the potable water tank. Used potable water or wastewater from the galley and lavatory sinks is disposed overboard via pressurized anti-icing ports. A vacuum generator forces the black water from the lavatory toilets into a 170 L waste tank also behind the aft cargo compartment. Black water is properly disposed of once the Levant has landed.

Traditional 115 V_{AC} and 28 V_{DC} powers the electrical components of the water and waste system including sensors, heaters, valves, vacuum generators, controllers, and compressors. The Levant's unique all-electric architecture avoids unnecessary weight penalties and power losses by replacing the bleed air with electrical pumps. The new system is simpler, easier to maintain, and more fuel efficient without stealing thrust from the engine to pressurize the water. Figure 48 presents the inboard profile of the aircraft showing only the water and waste systems connecting the galleys and lavatories to their respective storage tanks.

Fig. 48 Inboard profile of Levant featuring water and waste systems along with piping.

6.11 De-Icing and Anti-Icing System

Ice detectors work in conjunction with the de-icing and anti-icing subsystems at the engine inlets and leading edges of the wings, empennage, nosecone, and cockpit windshields. Electro-thermal heating blankets are secured within the interior of the leading edge of the wings and tail, and are used for both icing prevention and removal. The move from bleed air architecture to an electrical icing subsystem is highly advantageous for its previously mentioned savings in weight, complexity, upkeep, and fuel efficiency, as well as improvements in drag and noise from the removal of the exhaust ports. UACC predicts that the electrical icing subsystem will require a relative 50 *kW* based on the power needs of the Boeing 787[63]. Additionally, the engine internal de-icing makes use of the engine's own bleed air from a fan casing valve. The use of the engine bleed air for its own icing protection is the most effective method at the present time and will probably not be changed in the near future because it does not have the weight penalties of most other pneumatic architecture.

6.12 Cargo Handling

The cargo in Levant is carried in both containerized and bulk cargo form. Cargo is stored in Levant on the lower deck in three main compartments. The front cargo compartment can house 867.3 ft^3., equivalent to 8 LD-W unit load devices (ULDs). The aft cargo department can house 542.1 ft^3. of containerized cargo, equivalent to 5 LD-W ULDs, as well as 181.6 ft^3. of bulk cargo aft of the cargo door. Both cargo doors are of the 48" x 35" type, allowing rapid loading of containerized or bulk cargo into the aircraft, reducing the turn-around time for the carrier. The cargo floor is equipped with uni-directional rollers and ball rollers in front of the cargo loading doors. 5" lifting power rollers in front of the cargo doors provide both lateral and longitudinal movements for the containerized cargo being loaded. The cargo handling system is controlled by control panels installed near each cargo door.

Waxwing

Systems Integration Drawing. A view of the cockpit instrumentations is also presented (right).

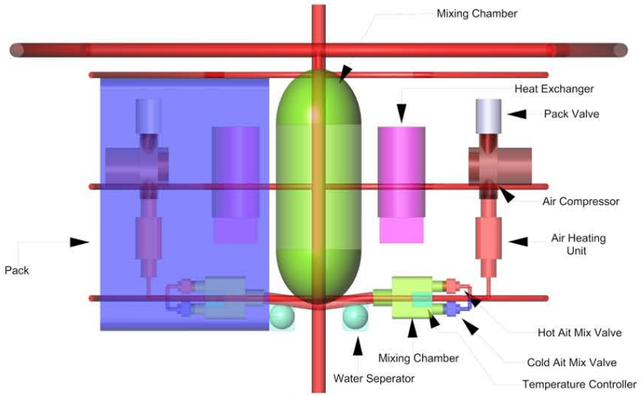

Electric Air Conditioning System

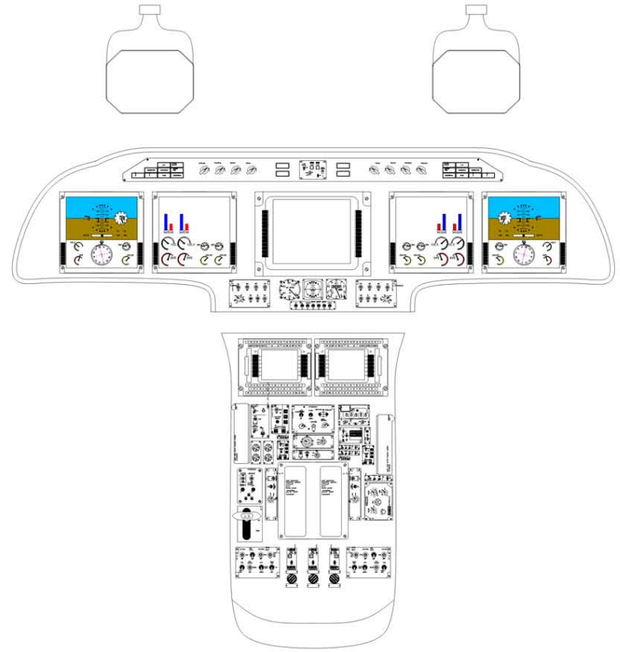

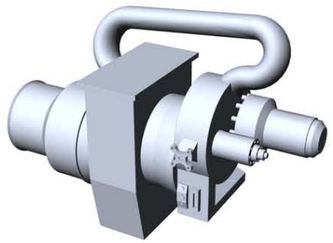

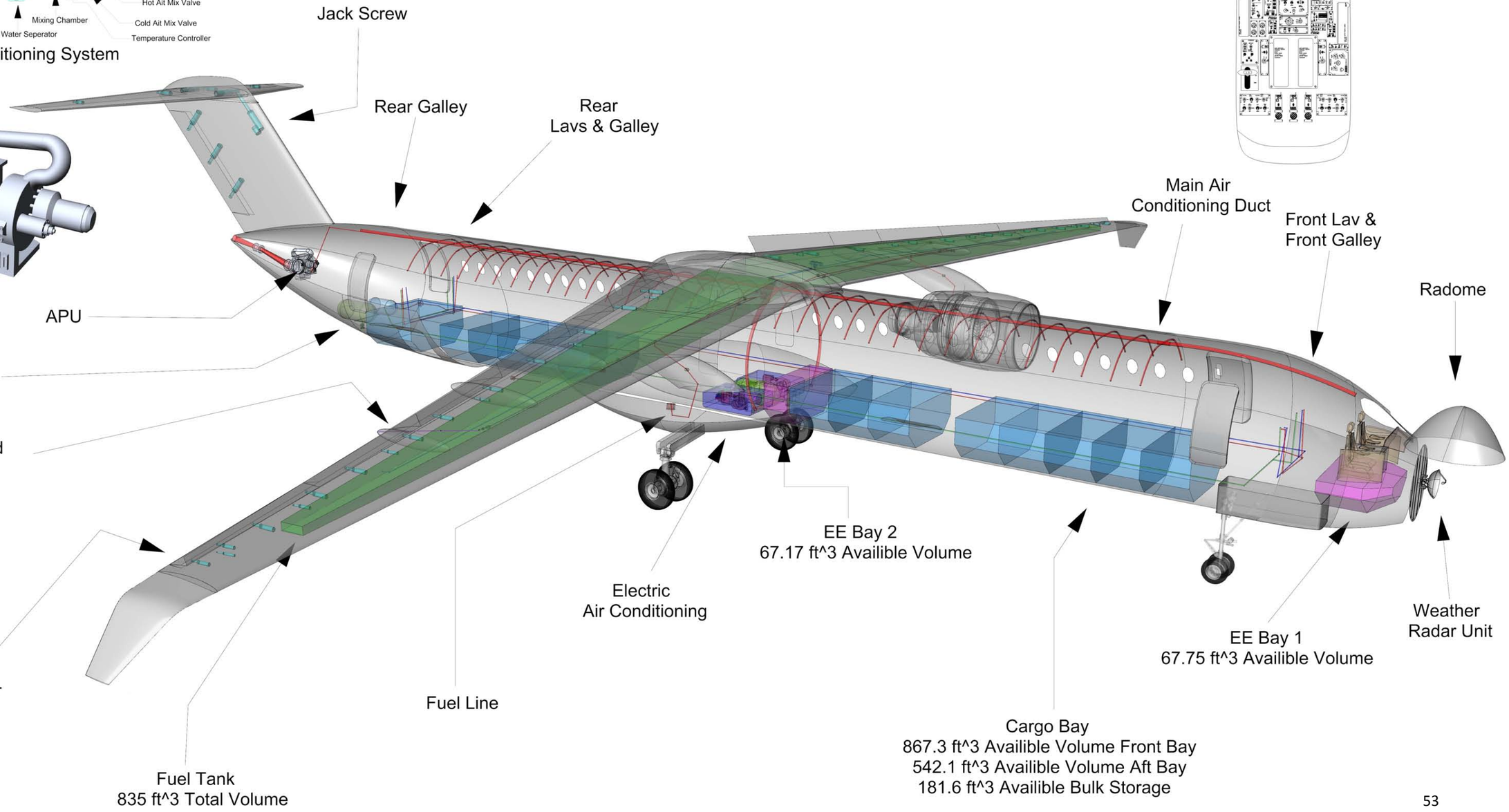

7. Weight Justification & Analysis

7.1 Electrical System Architecture Weight Decrement

As was presented in Chapter 6 of this document, the full electric architecture of Levant allows for significant weight reductions, as a result of simplification of the systems and elimination of heavy subsystems pertaining to hydraulic and bleed air power supplies. The Levant's all-electric architecture saves considerable weight by eliminating the unnecessary bulk and materials associated with hydraulics and pneumatics. Multiple NASA/Lockheed case studies[64,65]analyze the potential weight, fuel burn, and cost reductions of the all-electric architecture against conventional subsystems. One case study estimated an uniterated 2,700 *lbs.* weight reduction in a plane with a operating empty weight of 238,000 *lbs*. Simpler and cleaner electromechanical subsystems cut out the unnecessary weight from the aforementioned parts. Additionally, the electrical hardware is made more efficient and simpler via RPMUs. A NASA/Lockheed study[66] predicted a 22% net empty weight reduction in subsystems for a generic 150 passenger jetliner. The specified system weights were reduced or eliminated except for slight increases in the APU, electrical hardware, and avionics. These small weight increments were more than compensated from the elimination of the hydraulic & pneumatic piping and over 40% reduction in the air conditioning weight, due to the removal of a bleed air architecture. The Levant's weight reductions from all-electric architecture were based on the projections of relevant literature. The reductions were compared individually to the Levant's weight iterations and computed as either a ratio or flat difference. Each change to the empty operating weight was normalized with respect to the payload of the Levant in order to promote a more thorough and accurate projection. Figure 49 on the following page presents the weight adjustments for Levant due to an all-electric architecture.

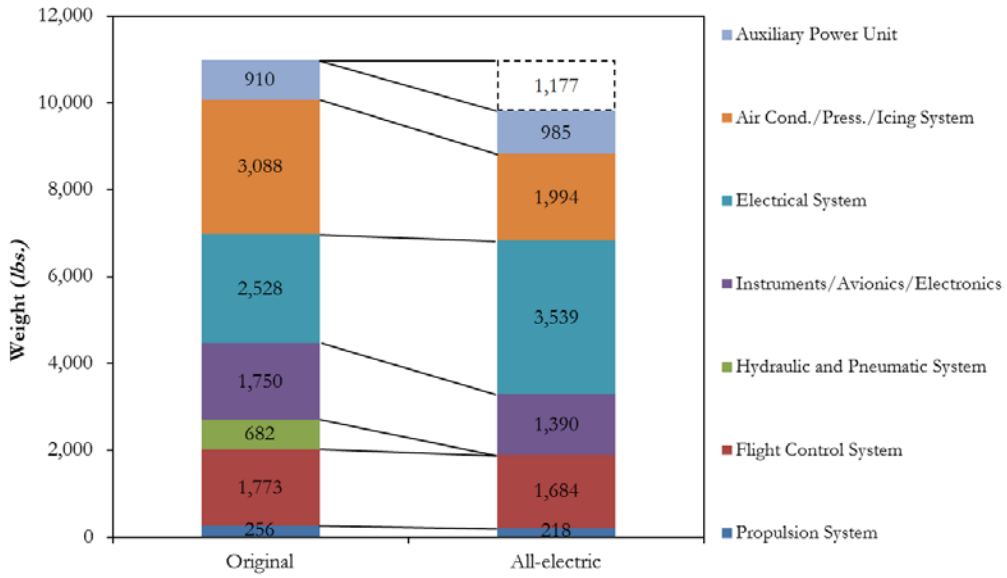

Fig. 49 Levant's weight adjustments due to all-electric architecture. Note that net weight reduction is indicated above the right hand weight column.

7.2 Final Weight Analysis

The Levant's weight was estimated from its mission design requirements and geometry comparable to similar aircraft. The initial estimates were averaged against the General Dynamic and *Torenbeek* methods[67], and then fed into an iterative algorithm. The impact of lightweight composites was estimated by comparing the reduced weight of Boeing 787 components against the components of similar sized aircraft. The differences were calculated as a percent reduction shown in Table 4 below. The additional weight reductions from an all-electric architecture were verified by the appropriate literature, normalized, and then applied to Levant. Table 5 on the following page presents the detailed empty weight estimation using General Dynamics, *Torenbeek*, and statistical methods. The corrected average values were obtained by averaging the aforementioned methods and applying the weight corrections of Table 4.

Table 4. Weight Correction

Empennage	-15 %
Wing	-10 %
Fuselage	-17 %
Nacelle	-10 %
Landing Gear	-3%
Fixed Equipment	-7%

Table 5 Detailed Empty Weight Estimation

Components	GD Method (*lbs.*)	Torenbeek Method (*lbs.*)	Statistical Results (*lbs.*)	Corrected Avg. Values (*lbs.*)
Wing	12,223	21,632	13,324	14,505
Horizontal Tail	1,040	1,383	1,950	1,241
Vertical Tail	997	1,238	1,671	1,108
Fuselage	8,100	17,610	15,511	11,572
Nacelles	2,975	2,366	1,845	2,156
Nose Landing Gear	628	883	818	759
Main Landing Gear	3,465	4,870	4,512	4,204
Engines	-------	8,165	9,416	10,283
Fuel System	-------	811	935	728
Propulsion System	323	232	308	218
Flight Control System	1,878	2,041	1,333	1,684
Instruments/Avionics/Electronics	1,826	2,236	1,381	1,390
Electrical System	1,918	4,081	2,040	3,539
Air Cond./Press./Icing System	4,556	2,737	2,481	1,994
Oxygen System	269	247	176	219
Auxiliary Power Unit	-------	1,168	718	985
Furnishings	7,531	8,470	5,443	6,839
Cargo Handling Equipment	-------	2,391	1,470	1,827
Operational Items	-------	6,785	4,171	5,184
Other Items	-------	438	269	359

Table 6 Detailed CG location and moments of inertia of Levant

Component	Weight *(lbs.)*	X_{CG} *(ft.)*	Z_{CG} *(ft.)*	$\|L_{xx}\|$ *(lb.-ft.)*	$\|L_{zz}\|$ *(lb.-ft.)*
1-Wing	14,505	73.77	-2.51	1,070,034	36,408
2-Horizontal tail	1,241	136.94	21.22	169,943	26,334
3-Vertical tail	1,108	113.20	17.56	125,426	19,456
4-Fuselage	11,572	59.71	1.21	690,964	14,002
5-Nacelles	2,156	117.47	6.94	253,265	14,963
6-Nose Landing Gear	759	17.44	-4.00	13,237	3,036
7-Main Landing Gear	4,204	79.65	-4.00	334,849	16,816
8-Engine	10,283	117.66	6.86	1,209,898	70,541
9-Fuel System	728	73.66	-2.54	53,624	1,849
10-Propulsion System	218	117.67	6.86	25,652	1,495
11-Flight Control System	1,684	77.25	-1.25	130,089	2,105
12-Avionics, Electronics & Instrum.	1,390	9.54	-1.45	13,261	2,016
13-Electrical System	3,539	63.18	4.30	223,594	15,218
14-Air Conditioning/ Anti Icing	1,994	75.06	-1.12	149,670	2,233
15-Oxygen System	219	75.06	-1.12	16,438	245
16-Auxiliary Power Unit	985	124.42	4.25	122,554	4,186
17-Furnishings	6,839	70.45	1.88	481,808	12,857
18-Cargo Handling Equipment	1,827	39.69	1.21	72,514	2,211
19-Operational Items	5,184	75.21	5.74	389,889	29,756
20-Other	359	13.80	-1.51	4,954	542

The center of gravity location was estimated based on their internal configurations and respective iterations of the weight analysis. The defined locations of the empty weight components are shown in Table 6, and are also located in the updated side profile for the aircraft in Fig. 50. Tables 7 through 9 show a detailed summary of takeoff and empty weight figures, as well as moments of inertia.

Table 7 Detailed takeoff weight

W_{fix}	24,019 *lbs.*
$W_{Structure}$	33,934 *lbs.*
W_{PP}	11,228 *lbs.*
W_{PL}	36,925 *lbs.*
W_{Crew}	950 *lbs.*
M_{ff}	0.800
M_{tfo}	*0.5%*
$W_{F_{Used}}$	21,500 *lbs.*
$W_{F,\max}$	37,875 *lbs.*
W_{tfo}	692 *lbs.*
W_E	70,793 *lbs.*
W_{TO}	145,668 *lbs.*

Table 8 Empty Weight CG

X_{CG}	71.94’
Y_{CG}	0’
Z_{CG}	1.75’

Table 9 Moment of Inertia

I_{xx_B}	71,389 *slug-ft²*
I_{yy_B}	1,871,993 *slug-ft²*
I_{zz_B}	1,800,604 *slug-ft²*
I_{xz_B}	159,371 *slug-ft²*

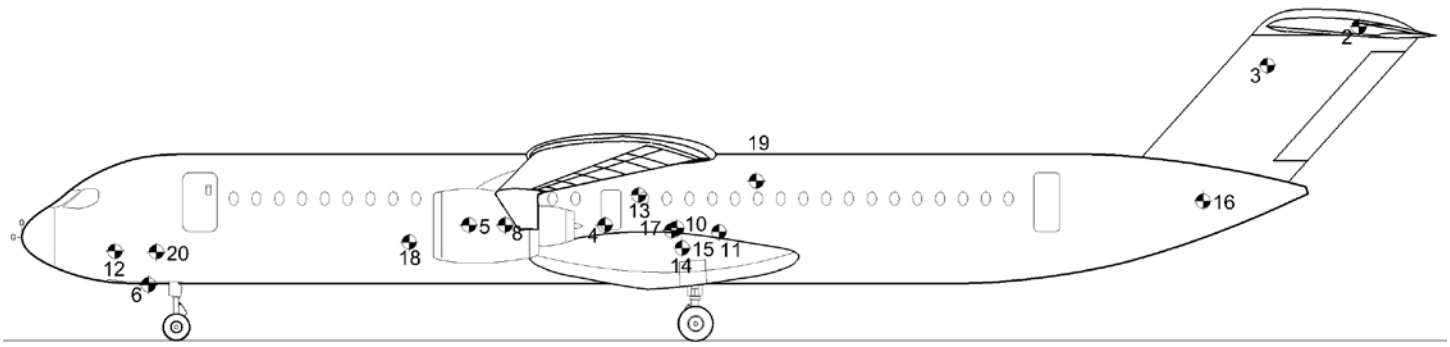

Fig. 50 The location of the main items listed in Table 6

8. Structures

8.1 Material Selection

The UACC determined that the optimum structural material for the Levant should be composites after considering the three main factors of weight, manufacturing methods, and near-field acoustic fatigue tolerance. The weight reduction due to aggressive utilization of advanced materials will improve the general fuel economy performance by reducing the overall mass as well as the induced drag of the aircraft due to less required lift to maintain steady flight. Manufacturing methods, which will be discussed in greater detail in Section 8.6, are important when determining material selection when one considers the argument presented by *Raman Raj et al*[68] comparing the "buy-to-fly" ratio of aircraft using 65% modern aluminum alloys with highly composite-based aircraft. "Buy-to-fly" ratio is defined as the weight of the purchase material to the weight of the finished structure. It is argued that given the large quantities of wasted raw materials created in the process of manufacturing metal structures, a very high-tech composite structure can be a more cost-effective way to manufacture primary airframe structures due to the significant reduction in raw materials consumed and thus reducing the manufacturing costs.

Carbon-laminated composites were selected for the fuselage, wing structure and surface, and empennage due to the potential for significant reduction in structural weight, as discussed in Section 7.2. UACC considered comparatively less cost-effective carbon sandwich composites due to their high strength for the engine nacelle, winglets, and control surfaces of the aircraft because these thin surfaces must withstand a wide range of loads while maintaining a thin profile. Titanium alloy Ti-8Al-1Mo-1V was used in the design of the pylon main structure due to its extremely high modulus of elasticity, yield strength, and heat tolerance. GLARE laminates were selected to be used on the skin of the surfaces near the engine, such as the engine pylon and nacelle structures, due to their acoustic fatigue resistance characteristics. Glass fiber reinforced polymers are considered for the construction of parts that have been manufactured in a single piece and have complex geometric

features and high surface curvatures, such as the radome and wing-to-fuselage fairings. The distribution of materials over the surface and substructures can be seen on the structural isometric foldout.

8.2 Load Estimation for the Wing

A maneuver envelope was constructed using guidelines provided by FAR §25.335 to determine the critical case load factors for the structural design process of Levant. This study indicated that the airframe is to be designed for a positive pull-up load factor of 2.5 g to occur at 260 *keas* at 37,000' and a negative push-over load factor of -1 g to occur at speeds between 235 and 260 *keas*. It was determined that the maneuver speed of Levant is 228 *keas* and the maximum safe flight speed in a 50 *ft/sec* gust is 239 *keas*. The dive speed at cruise altitude is computed to be 330 *keas*. The final V-n diagram is shown in Fig. 51.

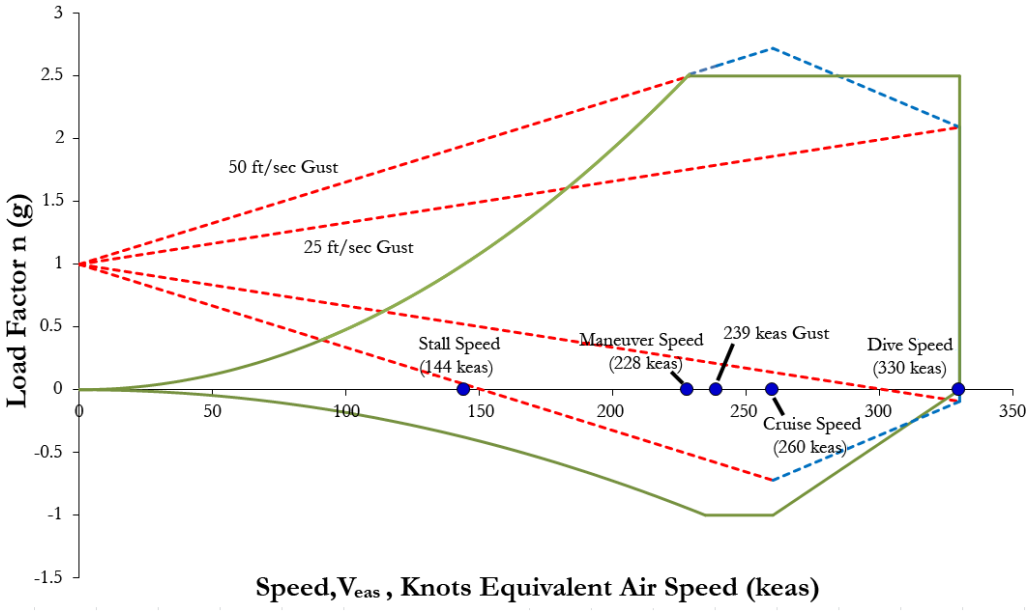

Fig. 51 Maneuver Envelope for Levant

The shear and bending moment diagrams for wing and fuselage were computed along *Libove*'s principal axes[69] to perform structural analysis and sizing using AAA's load module, which computes the total load by taking into account aerodynamic and dynamic loads in addition to concentrated and distributed weight sources on the lifting surfaces and fuselage structures. To accomplish this analysis, the aerodynamic loads acting on the wing structure were estimated using various high order methods presented in ESDU Data Item 83040[70], the result of which is shown in terms of lift, drag, and moment diagrams in Fig. 52. The moment coefficient plotted is computed around the elastic axis of the wing considering both lift and twisting forces acting on the structure.

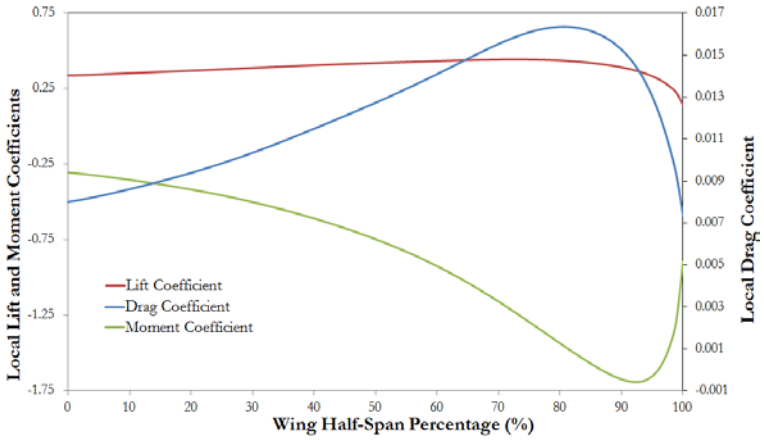

Fig. 52 Lift, drag, and moment coefficients vs. wing half span %

The loads acting on the wing structure were calculated by considering both the derived distribution of lift and drag forces as well as the torsional moment acting on the wing structure. The total acting forces and moments on the wing were computed by summing the aforementioned aerodynamic forces with the concentrated weight of the engines, wing structure, and the distributed fuel weight. These values were multiplied by a load factor of 2.75 to comply with the critical loading cases predicted by FAR §25.335. Figure 53 presents the final results of the critical wing load case for which the wing structure was designed.

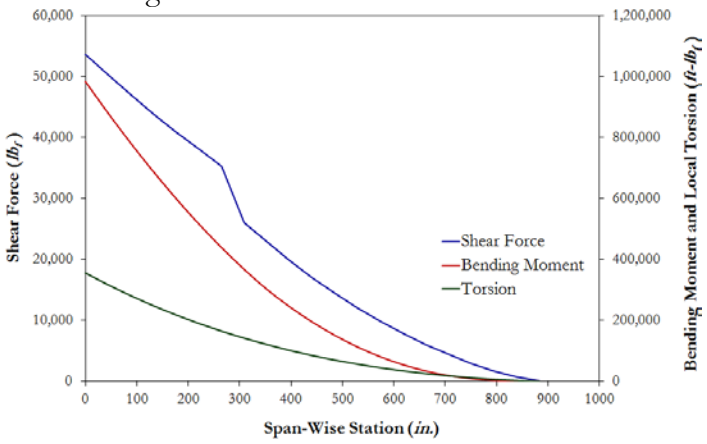

Fig. 53 Wing Loading

8.3 Wing Structure & Flutter

The wing structure of Ibis presents a number of unique features that require novel design solutions. First, Levant's swept-forward wing planform is susceptible to divergence because its aerodynamic center is ahead of its elastic axis. Divergence is the tendency of the wings to increase the local twist under the influence of increasing lift and moment applied to the wing as the angle of attack rises[71]. This will require a stiffer wingbox to prevent divergence-related structural failure. Second, Levant is designed to take advantage of maximum NLF on the surface of the wing to reduce airframe drag. However, slightly misaligned edges can trip the boundary layer causing unfavorable drag-inducing turbulent flow on the surface of the wing. Therefore, the wing skin structure consists of two single-piece skin panels on the upper and lower surfaces to minimize potentially misaligned skin panel edges (more likely to occur with multiple skin panels per surface). Lastly, wing flutter was addressed in the design of the high AR wing planform by increasing the number of stiffener elements under the wing skin panels.

Levant is not affected by the limitations of the manufacturing methods of an aluminum airframe, which restricts the size of the panels to the overall dimensions of the raw material and the tooling machinery. Utilization of composite materials and modern manufacturing technology allows Levant's wing skin panels to be laid up in two continuous pieces, therefore minimizing the potential for misalignment and the resultant turbulent flow experienced on the surface of the wing. Although this manufacturing strategy increases the size of the tooling and autoclaves needed to cure the composites after manufacturing, it improves the potential for maintaining laminar flow on the wing.

The wing super-structure consists of two primary spars, located at 15% and 65% of the chord length, and a series of composite ribs that are spaced on average 26" apart. The upper and lower wing skin panels are attached to the wing super-structure via reinforced brackets located on skin panel stiffeners that are connected to the wing ribs. The trailing edge fowler flaps are an independent structure that is installed on the rear spar. The surfaces of the trailing edge high-lift

devices are constructed of machined composite sandwich panels, which results in a high-strength, low-weight structure. Figure 54 presents a detailed breakdown of the Levant's wing structure.

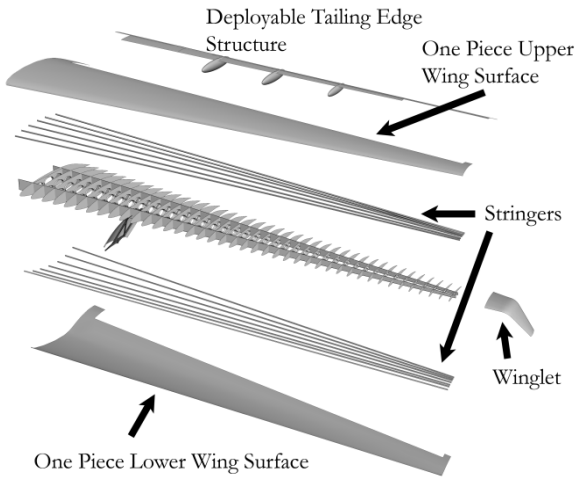

Fig. 54 Wing structure breakdown

Load analysis presented in Section 8.2 was used to perform an estimation of wing skin thickness and the overall area of wing spars. The super-structure was precisely defined by using AAA's software structure module to calculate the total skin cross-section area as well as shear web cross-section area of the at 21 distinct stations along the span of the wing. Figure 55 presents the result of this analysis, which was used to define a detailed parametric CAD model of the wing structure.

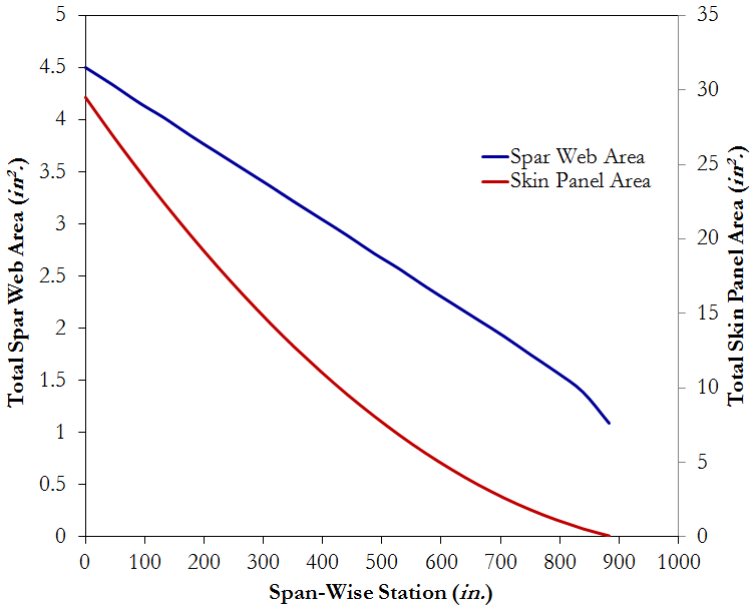

Fig. 55 Total spar and skin panel area vs. span-wise station

A parametric study was performed to investigate the relationship between the occurrence of flutter and wing geometry using the method presented by *Harris*[72] and *Leibeck et al*[73]. In conjunction with the trade study presented in Section 4.4, the decision to utilize a wing planform with an AR of 14.1 was confirmed to be below the flutter limits set by the aforementioned publications and therefore demonstrating an achievable structural solution with integrity. Figure 56 on the following page presents the results of this parametric study.

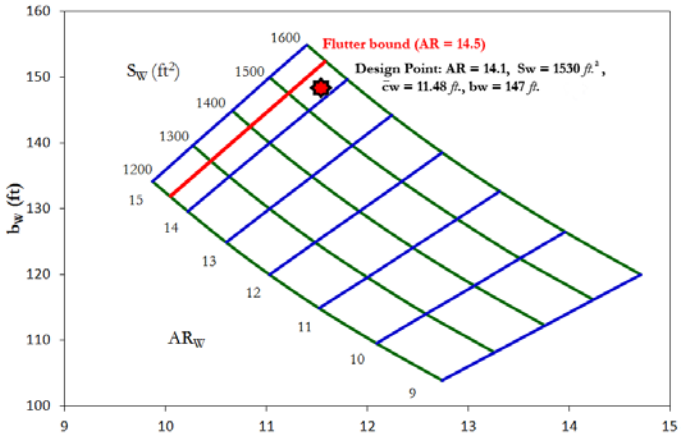

Fig. 56 Parametric study of aspect ratio vs. wing area. The flutter bound for a fully composite wing is shown in red and is equal to an aspect ratio of 14.5.

8.4 Load Alleviation System

UACC implemented a system of spoilers to reduce lift produced by the outboard section of the wings at the angles of attack higher than approximately 10^{o}[74] to improve safety concerns associated with excess wing loads at high angles of attack. Electromechanical actuators located in the wing deploy spoilers by the sub-system's ACEs when the PFCC determine the airspeed and angle of attack to broach the predetermined safety limit. This prevents an unintended overload of the wing primary structure therefore increasing the safety and extending the airframe's useful life. More information regarding this system can be found by reviewing the accompanying large scale drawing SY – 4.0.

8.5 Fuselage and Empennage Structure

The structure of the fuselage consists of eight major sections that are manufactured using carbon laminated composites with varying thickness, depending on the curvature of the cross

section. The outer skin is stabilized by adhesively-bounded longerons made by the same material. The major sections of the fuselage are connected to each other through titanium links and are sealed to prevent leakage of pressurized atmosphere. The floor panels inside the fuselage are supported by carbon fiber lateral and longitudinal beams, the latter of which contains the seat trails allowing for the installation of passenger seats in any selected pitch by the customer. The wing box structure is extended through the upper part of the crown of the fuselage and is anchored to three reinforced frames that carry the load from the wings to the fuselage as seen in Fig. 57. The middle fuselage section contains the landing gear pod, as well as the reinforcing keel beam that increases the stiffness of the middle fuselage structure. The pressure vessel is sealed in the front and back by two pressure bulkheads. The front bulkhead is consisted of a highly reinforced, slightly curved ball that separates the cabin space from the radome, and is sandwiched between layers of the skin of the nose section (referred to as Section 41). The aft pressure bulkhead is a dome-shaped, stabilized structure that intersects the fuselage's inner skin at an angle of 60° and is sandwiched between the skin layers of the aft fuselage section (referred to as Section 47). Figure 57 presents a view of the 3D CAD model constructed for Levant.

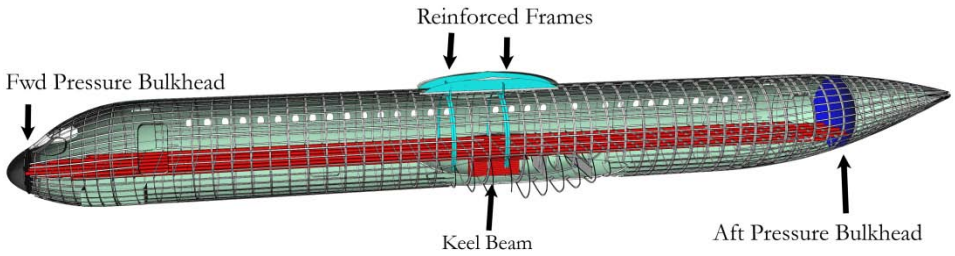

Fig. 57 Fuselage Structure

The carbon laminated composite structure used for the skin of the fuselage allows utilization of larger windows due to the increased tolerance to fatigue brought on by pressurization cycles[75]. Considering the corrosion resistivity of carbon laminated composite panels used for the fuselage structure, the cabin could be kept at higher levels of humidity and lower pressure altitudes with no adverse effects on safety or operational life of the structure. The vertical tail of Levant features a similar structure to the wing in terms of architecture and composite material application, however, it

utilizes three spars to provide fault tolerance in case of an APU blade loss as discussed in Sec. 6.8. The horizontal tail is supported on a trunnion which is secured to the upper vertical tail structure. The horizontal tail incident angle is varied by a triple redundant actuation system installed inside the vertical tail of the aircraft. Figure 58 (shown on the previous page) presents the general structural arrangement of the empennage of Levant.

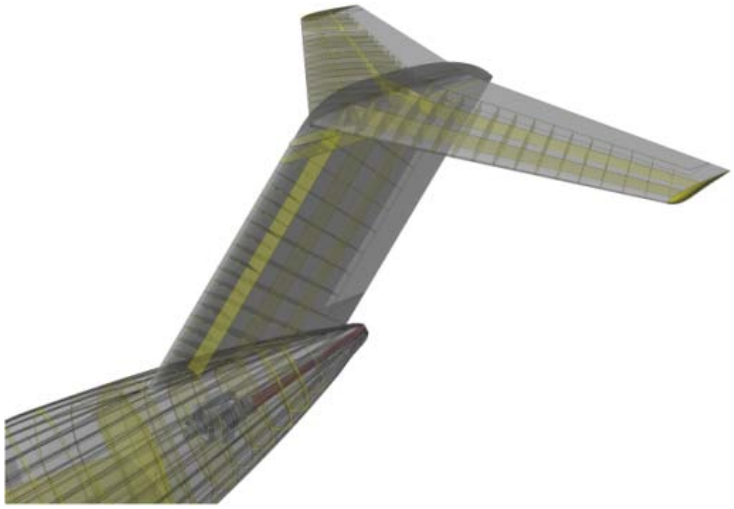

Fig. 58 Empennage Structure

8.6 Manufacturing Methods

Due to the utilization of carbon laminated composites, Levant is able to be manufactured using modern automated composite laying technology. This technology allows for manufacturing of large, continuous pieces of structure rather than the conventional method that relies on manufactured sub structures to create larger assemblies. The fuselage structure of Levant is to be manufactured in computer controlled, rotary matrix laying barrels that will be cured with heat and pressure to ensure obtaining the required mechanical properties. Wing skins are to be laid in large, continuous pieces, eliminating the possibility of small surface misalignments. If the wing surfaces of Levant are manufactured using conventional methods, these common misalignments (present at manufacturing or created during the service life) can lead to the tripping of the boundary layer, therefore making the implemented NLF technology less effective. Compatibility of the structural design of Levant with modern manufacturing methods allows for higher production rates and buy-

to-fly ratios. Higher rates of production allows for substantial reduction in the overhead cost per plane and higher buy-to-fly ratios allow for significant reductions in the cost of raw materials used to build the aircraft.

To allow for distributed manufacturing of the airframe of Levant, the structural assembly of the aircraft (shown in Sec. 8.7) was divided into sub-assemblies. This provides greater manufacturing flexibility, as well as allowing the producer to utilize skilled and diverse sets of labor force, therefore increasing the quality of the product while reducing the ultimate cost. The airframe breakdown was performed in a manner to allow air transportation of sub-assembly parts using regular cargo aircraft, therefore reducing the cost of distributed manufacturing as cargo aircraft capable of transporting oversized cargo will not be needed. The manufacturing breakdown of Levant is presented in Sec. 8.8.

Levant

Structural isometric drawing (bottom) and material distribution (right). The structural isometric is false-colored to make the floor beams, main spars and folding mechanisms more visible.

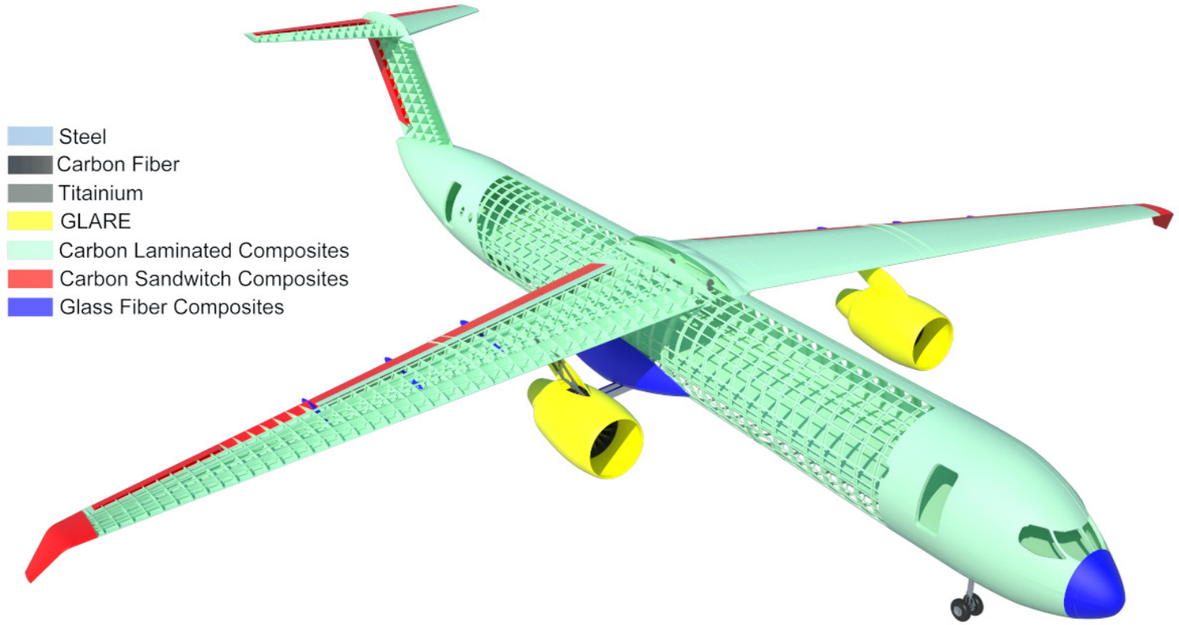

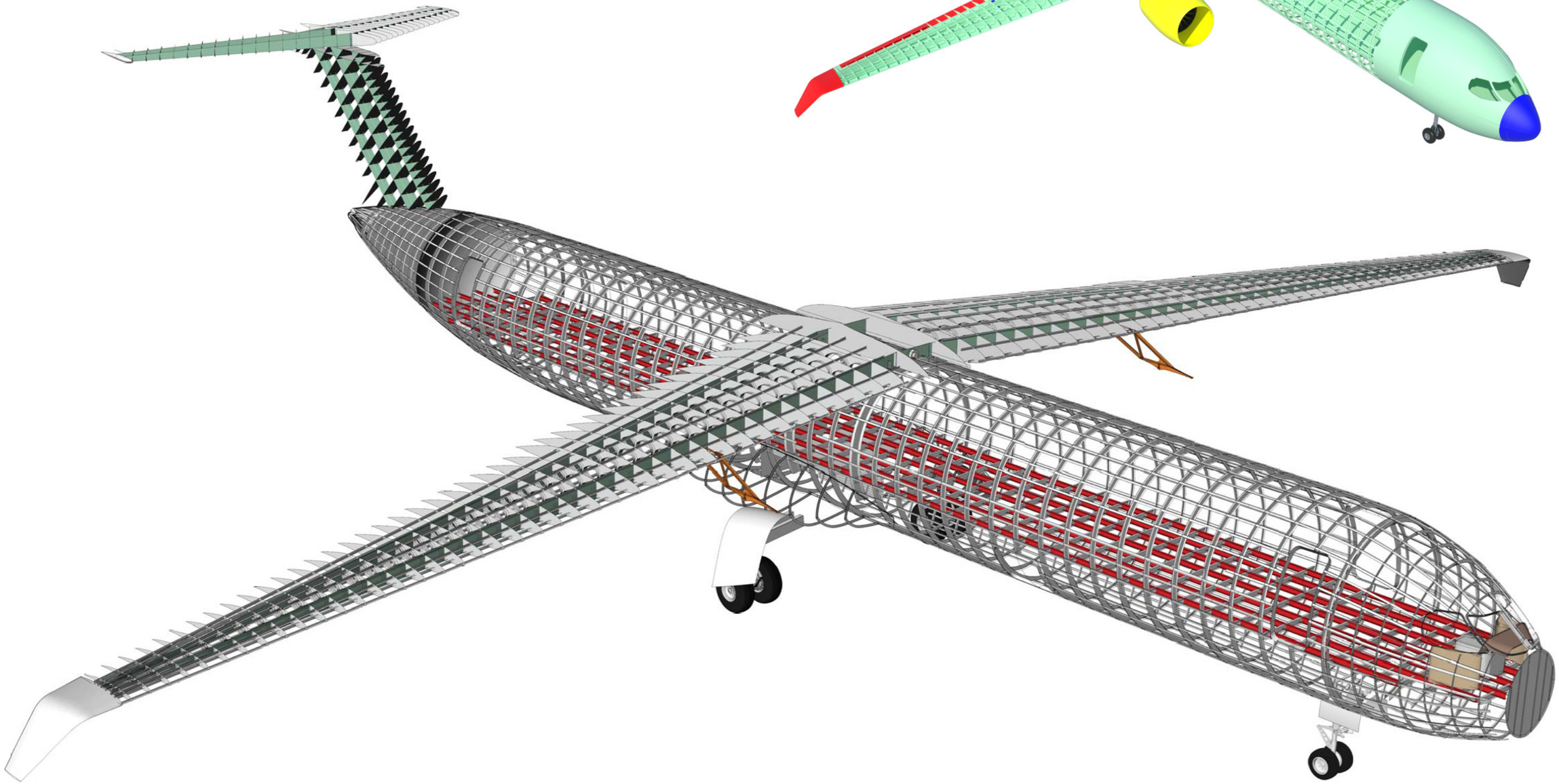

Levant

Manufacturing Breakdown of Levant. Naming of the sub-assemblies follows the Boeing's naming convention.

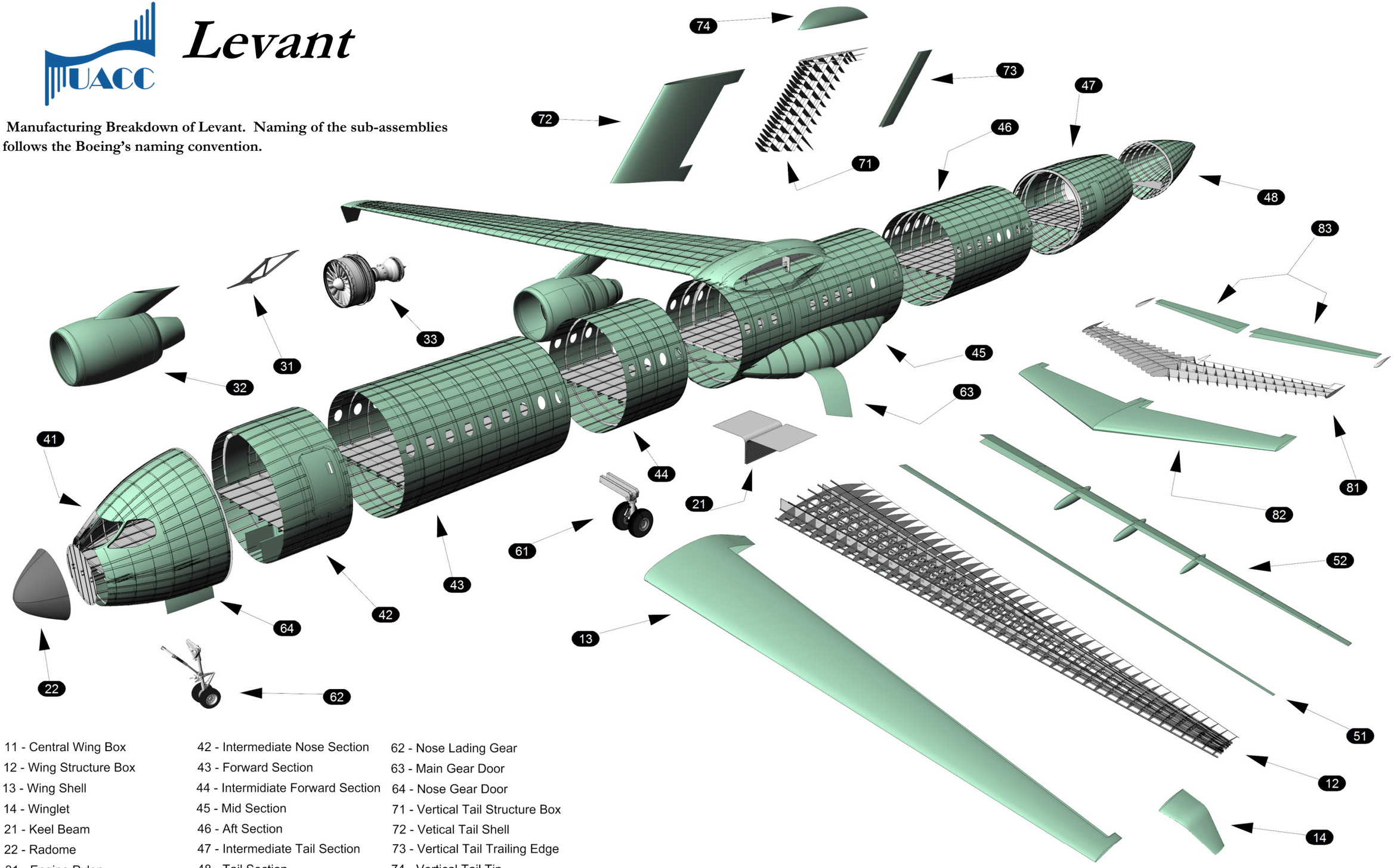

11 - Central Wing Box
12 - Wing Structure Box
13 - Wing Shell
14 - Winglet
21 - Keel Beam
22 - Radome
31 - Engine Pylon
32 - Engine Nacelle
33 - Built-Up Engine
41 - Nose Section
42 - Intermediate Nose Section
43 - Forward Section
44 - Intermidiate Forward Section
45 - Mid Section
46 - Aft Section
47 - Intermediate Tail Section
48 - Tail Section
51 - Spoilers
52 - Wing Trailing Edge
61 - Main Landing Gear
62 - Nose Lading Gear
63 - Main Gear Door
64 - Nose Gear Door
71 - Vertical Tail Structure Box
72 - Vetical Tail Shell
73 - Vertical Tail Trailing Edge
74 - Vertical Tail Tip
81 - Horizontal Tail Structure Box
82 - Horizontal Tail Shell
83 - Horizontal Tail Trailing Edge

9. Stability & Control

9.1 CG Travel

Static stability of the configuration was achieved by performing a parametric study of the impact of the longitudinal location of the wing on the magnitude of static margin using the methods presented by *Roskam*[76]. Mass properties analysis of Levant indicated that a CG travel range equivalent to 19.8% of mean aerodynamic chord of the aircraft is likely in a maximum range mission. A target positive stick free static margin of 15%[77] was selected for the mid-cruise segment of the flight to ensure the inherent static stability of the aircraft considering the variations of the location of the CG during flight. The result of this parametric study can be seen in Fig. 59.

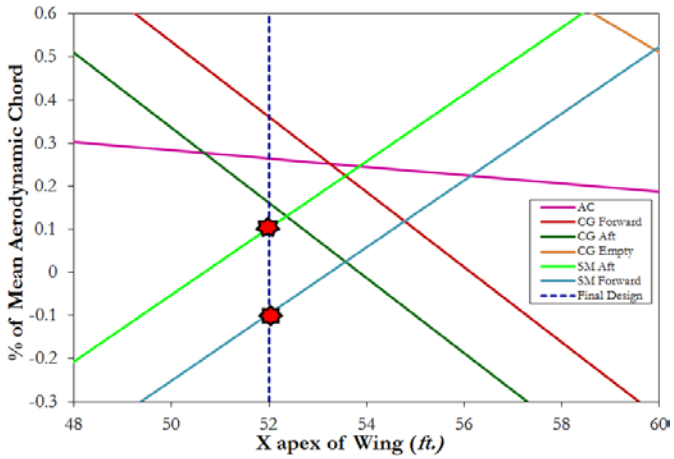

Fig. 59 Wing location trade study

UACC concluded that a longitudinal wing apex of 67' will provide sufficient positive static margin at forward and aft locations of the CG, therefore ensuring the maintenance of the static stability of the aircraft under all loading conditions.

9.2 Tail Sizing and Trim Maintenance

The empennage of Levant was sized to satisfy basic stability and control requirements set by MIL-F-8785[78] and recommended by *Roskam*[79] as well as being able to initiate the takeoff rotation of the aircraft MIL-F-8785 recommends that in order to maintain static longitudinal stability the air vehicle must possess negative values of C_{m_α} and $C_{m_{\dot{\alpha}}}$ at all flight conditions. A horizontal tail area of 342 $ft.^2$, capable of maintaining a C_{m_α} and $C_{m_{\dot{\alpha}}}$ of at least -0.2 rad^{-1}, was selected by performing a

parametric study that varied the area of a generic horizontal tail planform and then computed the corresponding C_{m_α} and $C_{m_{\dot{\alpha}}}$ using methods presented by *Roskam*[80]. A trim diagram was generated assuming the horizontal tail was capable of varying its root incident angle from -15° to 5° in order to verify the capacity of the plane to maintain trim under all loading conditions. This trim diagram can be seen in Fig. 60.

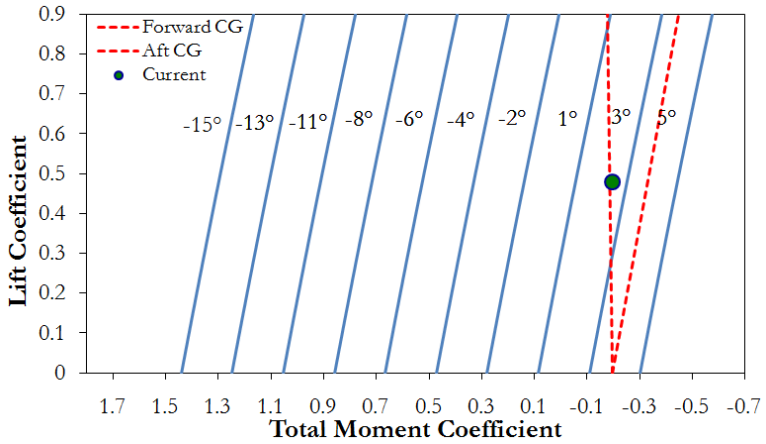

Fig. 60 Trim diagram for Levant

9.3 Stability & Control Derivatives

MIL-F-8785[81] requires that every aircraft should have a neutral point located behind the most aft center of gravity in order to maintain static longitudinal stability in all flight conditions. The location of the aircraft's neutral point was determined using the method presented by *Roskam*[82]. A selection of the results is presented in Table 10. As it can be seen from this table the location of the free stick neutral point, NP_{free}, in terms of wing chord is always behind the location of the center of gravity in all flight segments.

Table 10 Location of CG, aerodynamic center, and corresponding free stick neutral point at takeoff, cruise, and landing

Segment	Takeoff	Cruise	Landing
$\bar{x}_{cg}$	0.0121	0.0326	0.0412
$\bar{x}_{ac}$	0.0046	-0.0334	-0.0238
NP_{free}	0.3918	0.1437	0.4882

In order for the aircraft to remain statically stable, the pitching moment coefficient due to the angle of attack (C_{m_α}), and pitching moment coefficient due to angle of attack rate derivative ($C_{m_{\dot{\alpha}}}$) both should be negative. In order to verify the lateral and directional static stability of the aircraft, yawing-moment coefficient-due-to-sideslip derivative (C_{n_β}), and rolling-moment-coefficient-due-to-sideslip derivative (C_{l_β}) were computed as *Roskam* suggests to maintain lateral and direction static stability, C_{n_β}, should be positive while C_{l_β} should have a negative value. These derivatives were computed using methods presented by *Roskam*[70] and can be seen in Table 11.

Table 11 Important longitudinal and lateral-directional static stability derivatives

Segment	Takeoff	Cruise	Landing
C_{m_α} [rad^{-1}]	-3.5761	-4.2176	-3.6253
$C_{m_{\dot{\alpha}}}$ [rad^{-1}]	-7.576	-14.4480	-9.3978
C_{n_β} [rad^{-1}]	0.0800	0.0912	0.0158
C_{l_β} [rad^{-1}]	-0.0054	-0.510	-0.02927

9.4 Aileron Sizing

Due to the acceptability and availability of FAR-25 standards for commercial aircrafts, guidelines suggested by this code are used to estimate the size of the required ailerons for the aircraft. To estimate the size of the ailerons for this aircraft, a theoretical approach presented by *Roskam* was used. In the interests of brevity, this method is not presented in this proposal. The goal of achieving "level I" rolling qualities in the takeoff flight condition was pursued using the rolling time constants suggested by FAR-25. Assuming an individual aileron has a C_a/C_w equal to 20% starting at 77% of the half-span (following the flap), the outboard station of the aileron was calculated to be located at 98% of the half span. This aileron geometry was validated later during the analysis of the lateral directional flying qualities by fulfilling the rolling requirements defined in FAR-25.

9.5 Dynamic Stability

Considering that the RFP requested only the static stability analysis to be presented in the proposal, the results of the dynamic stability analysis and flight handling are not presented in their entirety in this proposal. Instead, the results of the most important segments of these analyses for takeoff, cruise, and landing are presented. Handling quality analyses performed using the AAA package indicates that Levant is capable of achieving Level I and Level II flight handling characteristics in all segments of flight. Results are confirming the satisfaction of the regulations presented by FAR-25 and MIL- F-8785 with regard to the time constants and damping ratios, in particular those pertaining to phugoid and short period oscillation modes.

In order to verify longitudinal dynamic stability, dynamic stability derivatives were evaluated along the *x*, *y* and *z* axes to determine the transfer functions and characteristic equations for Levant. The methods applied were obtained from USAF Stability and Control DATCOM[83]. Natural frequencies and damping ratios for short period oscillations, and phugoid mode, were calculated based on the methods presented by *Roskam*[84]. Values of short period and long period natural frequencies and damping ratios can be seen in Table 12 for takeoff, cruise, and landing conditions.

Table 12. Dynamic longitudinal stability characteristics for various flight conditions

Flight segment:	Takeoff	Cruise	Landing
T_{2_P} sec.	492	25.73	370
$T_{1/2_P}$ sec.	-----	-----	-----
$Level_P$	II	Unstable	I
$Level_{\xi_{SP}}$	I	I	II
$\omega_{n,S.P}$ (rad/sec^{-1})	1.5667	0.4641	1.6082
$\omega_{n_{P,long}}$ (rad/sec^{-1})	0.2123	0.1650	0.2455
ζ_{SP}	0.456	1.000	0.494
$\zeta_{P,long}$	-0.007	-0.163	-0.008

10. Environmental Impact

10.1 Biofuel Analysis

Environmental responsibility is a top priority for current commercial aviation. The implementation of an environmental tax requires a solution to reduce the influence of such a tax on the cost of commercial flight. The most significant contributor to the environmental tax is the tax on carbon emissions. Techniques must be developed to mitigate the emission of carbon considering the possible introduction of the environmental tax. Several methods to reduce CO_2 emissions are increasing the efficiencies of the propulsion system and utilizing NLF technologies, both of which are present in Levant. This already significant reduction can be augmented by the use of low carbon footprint fuels. The use of such fuels can result in an 80% reduction in the net carbon output, and a corresponding reduction in carbon taxation[85].

Of all the alternative fuels, biofuels are the only ones that result in a net reduction of carbon footprint due to the fact that their biological sources sequester CO_2 as they grow. Ideally, this results in a carbon neutral product; however, the use of biofuels represents an 80% reduction in carbon emissions due to fossil fuel use in their production.

For their benefits, biofuels also bring some challenges. If their biological sources are not chosen carefully, they could compete for arable land with food crops, which is not a sustainable option. Additionally, an ideal biofuel would require no modifications to aircraft or infrastructure of the airports. To ensure this, ASTM International established a new framework, known as D 7566, to classify fuel blends containing synthetic* hydrocarbons. D 7566 refers back to the requirements for traditional jet fuels, D 1655. This ensures that all synthetic fuels are "drop in" fuels, i.e. they require no changes to any piece of system or infrastructure[86].

As a result of these requirements, the ideal biofuel would consist of Hydrotreated Renewable Jet (HRJ) derived from sources such as japtropha, camelina, algae, and halophytes[87]. It is created by extracting and filtering the oil from the feedstock and then heating and hydro-treating it to correct

* Synthetic refers to both biologically and fossil fuel derived manufactured fuel, e.g. Coal-to-Liquid and Biodiesel

its molecular structure[88]. After extraction, the feedstock residue can be converted to methane and burned to create the electricity needed to power the process, as well as selling electricity back to the grid[89]. This can bring the carbon emissions reduction up to 100%, or even as high as 124% because the energy that is sold back to the grid offsets energy that would otherwise be produced from fossil fuels[90]. HRJ is chemically similar to traditional jet fuel and is considered a "drop-in" fuel[91]. The small differences between HRJ and traditional jet fuel can actually be beneficial, as the use of HRJ can result in a decreased fuel burn of 3%[92]. HRJ feedstock can be grown in areas not suitable for food crops, thus removing arable land competition. The most promising biofuel is algae derived HRJ due to its ability to be grown in polluted water, salt water, and deserts. A typical alga is shown in Fig. 61. It is also capable of producing fifteen times more oil per square kilometer than other biofuel crops[93], making it the best candidate for large scale production. Also, an algal biofuel facility could be attached to a fossil fuel power plant, and use the power plant's exhaust to feed the algae. Because algae thrive on CO_2, their growth will be encouraged while sequestering the plant's CO_2 emissions[94]. Currently, D 7566 is meant only for fuel blends; however, the Commercial Aviation Alternative Fuels Initiative is working with ASTM International to add HRJ to D 7566 by the end of 2010[95].

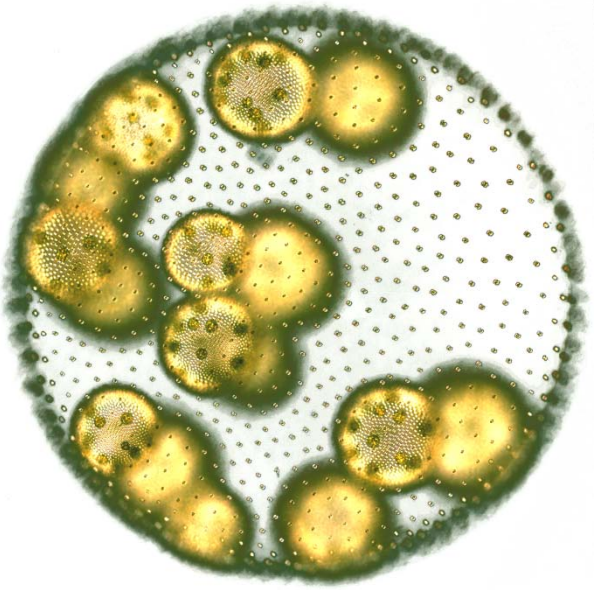

Fig. 61 Microscopic view of an alga

Due to carbon taxes and the emerging potential of algae-based fuel, as well as other technologies that directly convert sugar into jet fuel by use of microbes or catalysts[96], the projected costs of HRJ have a large value of uncertainty. Additional cost analysis of HRJ can be found in section 13.3.

10.2 Environmental Tax Modeling

In order to include the effects of the proposed environmental taxation methods on the aircraft's Direct Operating Cost (DOC) and Cash Airplane-Related Operating Costs (CAROC), a method based on the work presented by *Schwartz* et al.[97] was adopted and used to perform flight path optimizations presented in Sec. 13.1. This method accounts for four main components of the environmental tax. The most significant component is the carbon tax, which is computed as 0.33¢ per gallon fuel burned. *Schwartz* suggests that the carbon emissions, for any given propulsion system, are a linear function of fuel burn, and therefore are independent of altitude*.The combined taxation accounting for NOx emissions, Aviation Induced Cloudiness (AIC), and high altitude cirrus clouds were computed as a multiplier to be added to the baseline carbon tax (as a percentage). Given that *Schwartz* provides values for the variation of the influence of each of these forms of emissions as a function of altitude, her model was adopted to compute the total environmental tax imposed on the operation of the aircraft. Figure 62 presents the variation of taxable pollutants normalized to one, based on CO_2 emissions, which are assumed constant, independent of altitude. Equation 4 is used to compute the environmental tax in U.S. dollars,

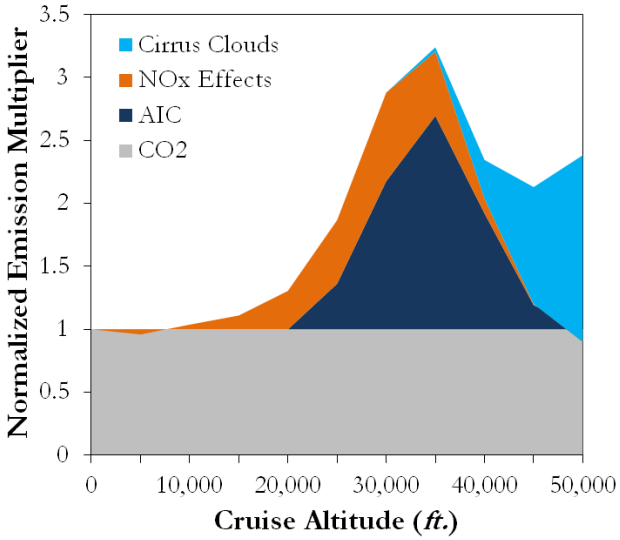

Fig. 62 Environmental Multiplier vs. Altitude

$$C_{ENVTAX} = \underbrace{0.33}_{\substack{carbon \\ emissions}} \cdot \left(1 + \sum_{1}^{3} M_i\right) \tag{4}$$

where M_i is the corresponding normalized emission multiplier as shown in Fig. 62.

* Note that the variation of altitude has a significant effect on the block fuel burn of the aircraft, therefore affecting the total carbon emissions of the airplane

10.3 Noise Verification

The ICAO Chapter 4 noise requirement defines three main noise measurement positions for the processes of noise certification of the aircraft. Flyover noise of the aircraft is measured on the ground at a point 6500 *m.* away from the start of the takeoff roll, while the approach noise is measured on the extended centerline of the runway 2000 *m.* away from the edge of the landing field. The lateral noise for the aircraft is measured on a line parallel to the axis of the runway 450 meters away from the centerline, at the location with the maximum noise level. Figures 63 through 65 illustrate these noise measurement reference points as specified by ICAO Chapter 4.

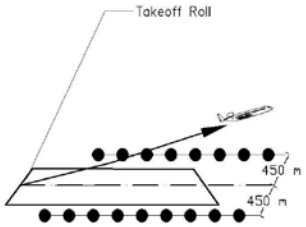

Fig. 63 Lateral Noise Reference positions

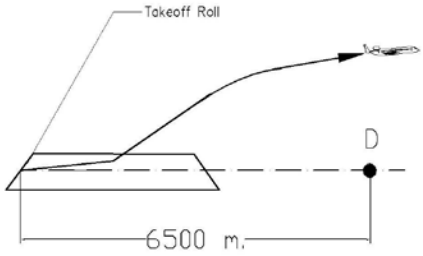

Fig. 64 Flyover Noise Reference Point (D)

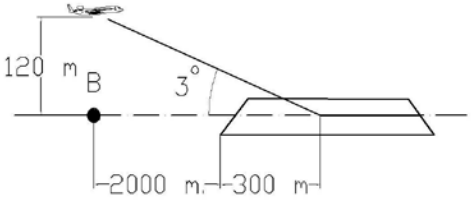

Fig. 65 Approach Noise, Reference Point (B)

ICAO Chapter 4 also cites the maximum value of the acceptable noise for each of the described reference measurement positions, and allows a cumulative deviation of 3 *dB* from the reference noise levels, while limiting the deviations at each point to 2 *dB.*[*] Table 13 presents the maximum noise levels required by ICAO chapter 4. The NASA N+1 study[98] requires a total reduction of 20 Effective Perceived Noise Decibels (*EPNdB)* compared to the ICAO-4 values. Three different modules of the ANOPP† software were used to predict the noise levels of the aircraft corresponding to each of the measurement positions for flyover, approach, and lateral noise. Each module consisted of an executable file, including sub-modules such as atmospheric absorption, geometry, and noise level.

Table 13. Noise Level Requirements

Position:	ICAO-Ch. 4 (EPNdB)
Lateral Noise	94
Flyover Noise	89
Approach Noise	98

[*] Annex 16 to the conventions on International Civil Aviation, Volume I, Aircraft noise, P. II.3.3 dated 20/11/2008, International Civil Aviation Organization

† Aircraft Noise Prediction Program, developed by NASA Langley Aeroacoustics research center

The engine noise was modeled by modifying the Circular Single-Stream jet noise module (SGLJET) using the results of the engine performance analysis using GasTurb. Inputs were provided via on-screen plain text data entry and the outputs from ANOPP were produced in the form of plain ASCI disabled .txt files, which were transferred to a spreadsheet for post-processing.

10.4 Parametric Studies and Noise Optimization

Due to the relatively small suppression of the lateral noise for the design, an analysis was conducted to identify the location of the maximum lateral noise for the aircraft. Perceived noise levels were plotted versus the distance traveled on the runway on a line parallel to the axis of the runway, 450 *m.* away from the centerline. Figure 66 presents the results of this analysis. As can be seen from this figure, a maximum lateral noise of 77 *dB* is expected to be observed at 5,800' down the runway. Using these results, a parametric study was performed to optimize the takeoff flap deflection and thrust setting in order to minimize the noise at 5,800' down the runway as well as at the flyover point 6,500 *m.* down the runway. Figures 67 and 68 present the results of these optimizations for takeoff configuration.

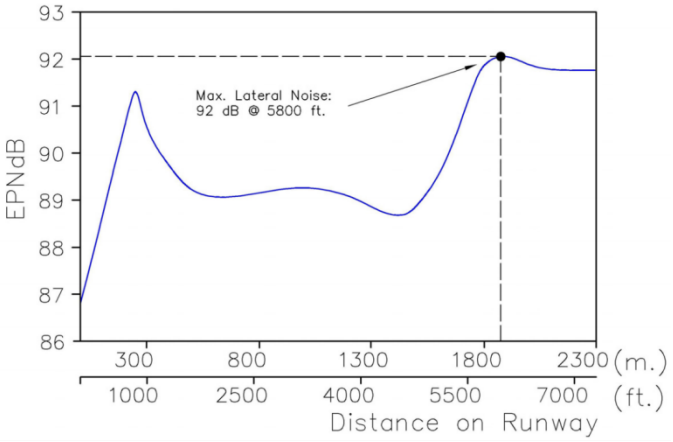

Fig. 66 Lateral EPNdB vs distance on Runway

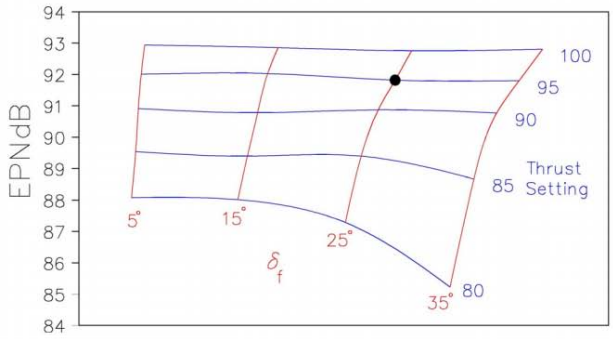

Fig. 67 Lateral noise for different combinations of thrust settings and flap deflections at 5,800' down the runway

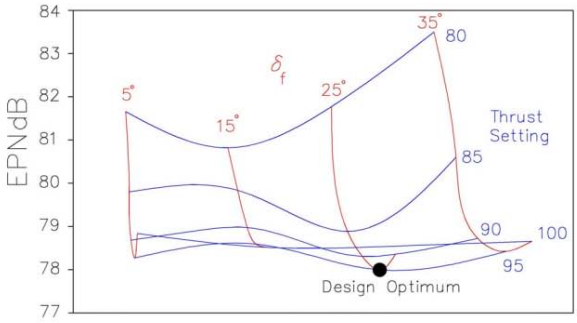

Fig. 68 Flyover noise for different combinations of thrust settings and flap deflections at 6,500 *m.* down the runway

From these analyses it was observed that a thrust setting of 95% combined with a flap setting of 25° would yield the largest reduction in cumulative aircraft noise for takeoff. It should be noted that

maintaining 95% thrust levels at low altitudes immediately after takeoff reduces the flyover noise of the aircraft tremendously, while simultaneously having no notable effects on the lateral noise characteristics of the aircraft.

10.5 Final Noise Analysis

A final noise evaluation was performed using ANOPP to confirm that the RFP's requirement with regards to aircraft noise was satisfied. Table 14 presents the results of the final noise calculations in the optimum configurations, as well as the difference of noise levels with the requirements set by ICAO Chapter 4 for two-engine commercial airliners.

Table 14. Final Noise Evaluation

Position:	EPNdB	ICAO-4 Offset
Lateral Noise	92	-2 *dB*
Flyover Noise	78	-11 *dB*
Approach Noise	88	-10 *dB*
Total	------	-23 *dB*

As it can be seen from these figures, Levant achieves 47 *dB*[*] reduction in noise compared to ICAO Ch. 4 requirements presented in Table 15. This noise performance surpasses the requirements set by the RFP in terms of noise reduction and highlights one of the most important features of Levant.

[*] Pratt & Whitney Claims that each of the two PW1000G engines are 20 *dB* quieter than present day turbofan technology, which is ICAO Ch.4 Compatible for the most part.

11. Performance Validation

11.1 Takeoff Performance

The required takeoff field length for Levant is determined by applying relations presented by ESDU Data Item 85029 [99] and considering the ground effect on generated lift and drag[100]. It is assumed that the aircraft uses the previously sized flaps during takeoff without assistance from leading edge high lift devices, making the maximum lift coefficient ($C_{L_{max}} = 2.2$) attainable. The average kinetic friction coefficient was computed using the data presented by *Roskam*[101] to be 0.02, assuming a conventional tarmac mix, as used in the United States.

The takeoff trajectory was computed for normal takeoff and can be seen in Fig. 69. Assumptions regarding takeoff performance computations and the results of this analysis are presented in Tables 15 and 16.

Table 15 Takeoff Condition

$C_{L_{max_{TO}}}$	2.2
$C_{DO,TO}$	0.0328
$L/D\|_{TO}$	16
Π_{TO}	0.95

Table 16 Takeoff Performance

$V_{S_{TO}}$	114 *kts.*
V_{LOF}	137 *kts.*
S_{TO}	7,323’
$S_{TO,G}$	4,996’

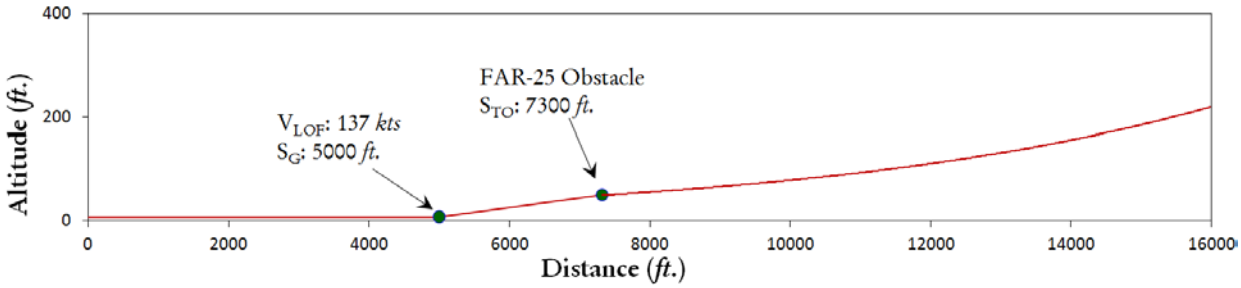

Fig. 69 Takeoff trajectory

11.2 Climb Performance

In order to verify that Levant’s performance agrees with federal regulations, the climb gradient was compared with the values set by various sections of FAR 25. §25.121 requires all commercial aircraft to be able to maintain a climb gradient of at least 1.2%. At an altitude of 10,000’, FAR §25.111 requires that a commercial aircraft should be able to maintain the same climb gradient

with only one engine operative. Additionally, FAR §25.105 requires that the climb gradient in the transition phase between takeoff and climb should be no less than 2.4%. The result of the climb gradient analysis can be seen in Table 17, which indicates that all FAR requirements are satisfied.

Considering the high bypass ratio of the engine used and the requirements for an operational ceiling of 41,000', analyses were performed to verify that Levant is capable of achieving this max operational ceiling. The operational ceiling is defined as the altitude at which the rate of climb is equal to 150 *ft./min.* Using the engine performance map developed for the power plant of Levant, it was estimated that the ceiling rate of climb would occur at 43,000' in ISA conditions. At this altitude, the specific excess power available to the pilot is 396 *ft./min.*, which allows for a climb gradient of 0.6 %. Figure 70 presents the climb performance for Levant.

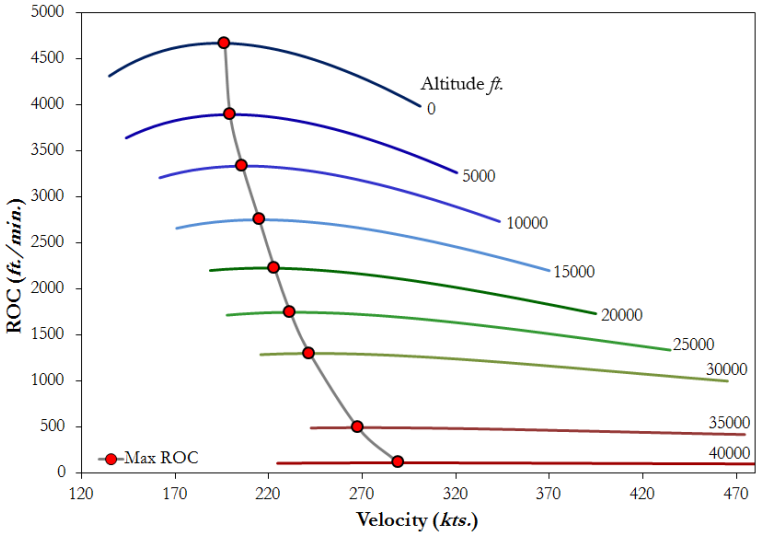

Fig. 70 ROC vs. velocity at various altitudes. Ceiling occurs at 43,000', corresponding to a ROC of 150 *ft/min*

Table 17 Results of climb gradient analysis, along with corresponding FARs

Regulation	Required Climb Gradient	Achieved Climb Gradient
FAR §25.121 Takeoff	1.2%	1.9%
FAR §25.111 Takeoff OEI	1.2%	1.9%
FAR §25.105 Transition Phase	2.4%	2.8%

11.3 Max Cruise Speed Validation

In order to verify the RFP requirements relating to cruise speed performance, thrust required to maintain level flight was computed using Equation 5:

$$T_{req} = \left(\frac{C_{D0_{clean}} \rho S_w V_{Cr_{max}}^2}{2\cos(\alpha + \varphi_T)} \right) + \left(\frac{2W_{Cr}^2 B_{DP_{clean}}}{\rho S_w V_{Cr_{max}}^2 \cos(\alpha + \varphi_T)} \right) \quad . \qquad (5)$$

This value was plotted versus the installed thrust data obtained using GasTurb. Figure 71 presents a graph of thrust vs. velocity for both available and required thrust for the cruise altitude of 39,000'. It can be seen from this figure that the maximum cruise speed is equal to 467 *kts.* at an altitude of 39,000', which corresponds to 0.8 Mach, satisfying the goal set by the RFP for the maximum cruise speed (0.83 Mach). The velocity corresponding to maximum range was also determined from this analysis to be 467 *kts.* (0.8 Mach at 39,000'). The maximum excess thrust is estimated to be achieved at a speed of 300 *kts.* (0.506 Mach at 39,000'), which yields the maximum maneuverability and endurance within the flight envelope.

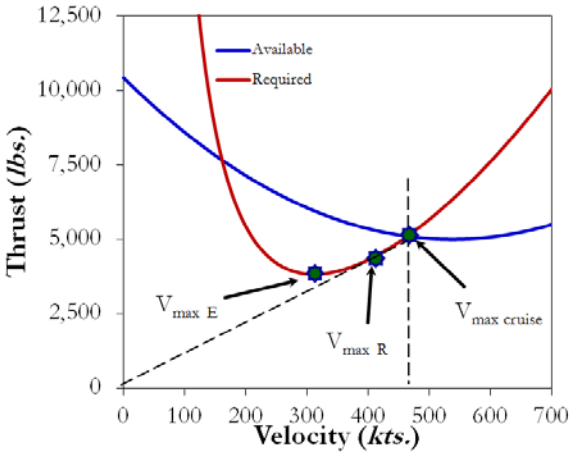

Figure 71. Available & required thrust vs. velocity (*cruise*)

11.4 Fuel Burn Performance

Detailed analysis of the block fuel burn was performed to assess the economic advantages of Levant over present day technology. Analysis was repeated for three different block ranges of 850, 1,200, and 3,500 *nm.* for 175 passengers, equivalent to a payload of 37,000 *lbs.* Figure 72 presents the results of this analysis. From this figure it is evident that for longer range missions, significant reductions in block fuel burn are attained by flying at higher initial cruise altitudes. The initial cruise altitude has a very minute effect on the block fuel burn of the aircraft for shorter ranges, such as the 1,200 *nm.* nominal block range specified by the RFP. This analysis also confirmed that the block fuel burn for a 1,200 *nm.* mission with 175 passengers is approximately 6,550 *lbs.* (corresponding to a fuel burn per passenger of 37 *lbs./seat*), assuming an initial cruise altitude of

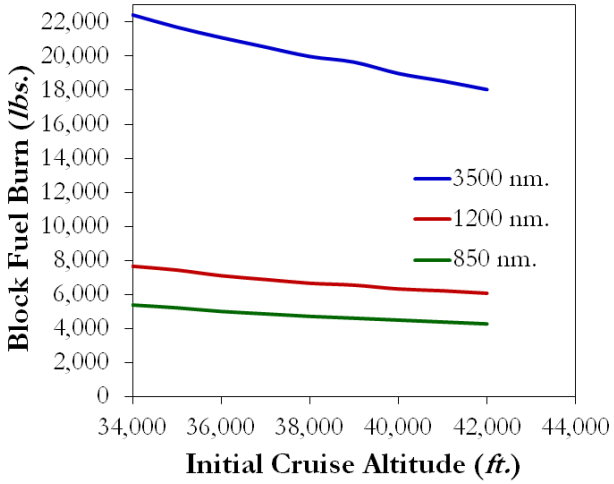

Figure 72. Block fuel burn vs. initial cruise altitude for ranges of 3,500 *nm.*, 1,200 *nm.*, and 850 *nm.*

39,000'. This value approximates the goal set by NASA N+1[102] study, confirming that the power plant technology level selected for Levant is capable of satisfying the market's needs.

A payload-range chart was also constructed for Levant and is presented in Fig. 73. Assumptions made for this analysis are presented in Table 18.

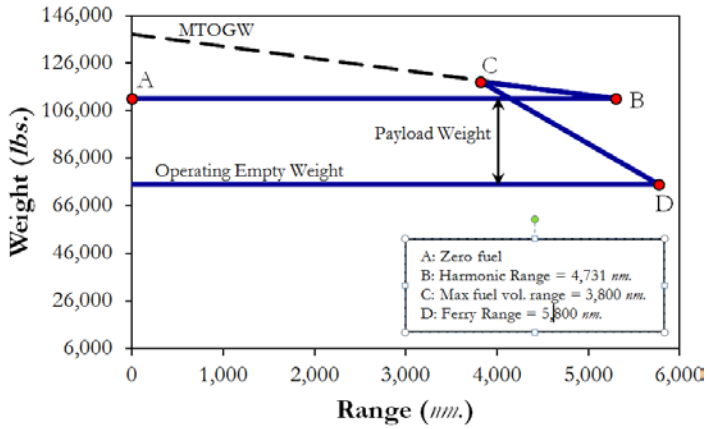

Figure 73. Payload-Range chart

Table 18 Assumptions for payload range curve

T_{avail}	9,800 *lbs.*
α	2°
Mach	0.8
$C_{L_{opt,MaxR}}$	0.52
ICA	39,000'
C_{D_0}	0.019
TSFC	0.46 *lb./hr.-lb.*

11.5 Landing Trajectories

The method presented by ESDU Data Item 84040[103] was used to estimate the landing distance for the aircraft computed assuming a Maximum Landing Weight (MLW) of 114,996 *lbs.* MLW is defined by the RFP as the maximum zero-fuel weight (110,390 *lbs.*), plus fuel reserve for the longest range and highest payload for the aircraft (3,572 *lbs.*). The ground effects are taken into account in this analysis, for which the results are presented in detail in Table 19. Figure 74 presents the results of the simulation of the landing trajectory of the aircraft.

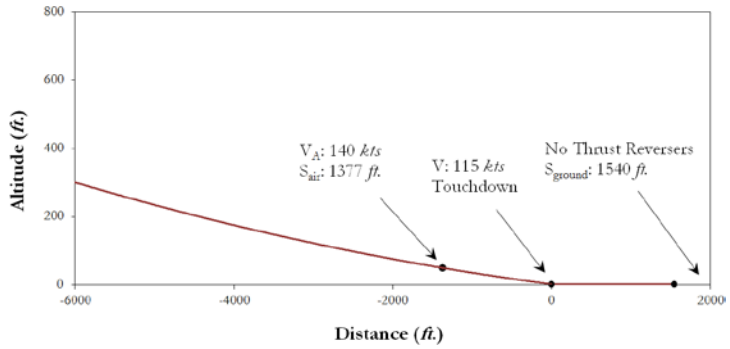

Figure 74. Landing Trajectory for MLW of 114,996 *lbs.*

Table 19. Landing performance

Δ_n	0.1
$\bar{\gamma}$	0.06
V_{S_L}	108 *kts.*
V_A	140 *kts.*
S_{air}	1,377'
S_{LG}	1,540'
S_L	2,917'

11.6 One Engine Inoperative Conditions

Considering that the engines of Levant are installed on the wings away from the fuselage centerline, analysis was performed to insure that the design rudder is capable of maintaining the control of the aircraft at all flight conditions. The method presented by *Roskam*[104] was used to compute the maximum controllable speed in OEI conditions, as well as the necessary rudder deflection to cancel the induced yawing moment due the inoperative engine. The analysis was repeated for takeoff, climb, and cruise conditions. The result of which can be seen in Table 20.

Table 20 OEI performance

Flight Condition	Takeoff	Climb	Cruise
Altitude (*ft.*)	0	15,000	39,000
Minimum Controllable Speed (*kts.*)	137	396	384
Rudder Deflection (°)	40	27	18

From this analysis it was found that the present rudder control surface is capable of safely controlling the aircraft at maximum thrust available with one engine inoperative at all flight conditions. Also, it was determined that a double-hinged rudder control surface with a maximum deflection of 45° will be necessary for aircraft to possess sufficient OEI controllability, considering that double-hinged rudders produce a higher yawing moment coefficient.

12. Ground Operations

12.1 Compatibility with Airport Infrastructure

The design philosophy of Levant dictated that in order to ensure the commercial success of the aircraft, the buyers should not need to modify their present day airport infrastructure to accommodate Levant. To be compatible with present day gates and hangers in use by airlines to support Boeing 737 and Airbus A320 aircraft, it was decided that Levant, as a viable replacement, should be able to have the same wingspan on the ground as the aforementioned aircraft. Therefore, a folding wing mechanism was employed to reduce the span of the wing during ground operations and docking. Figure 75 presents Levant during ground operations.

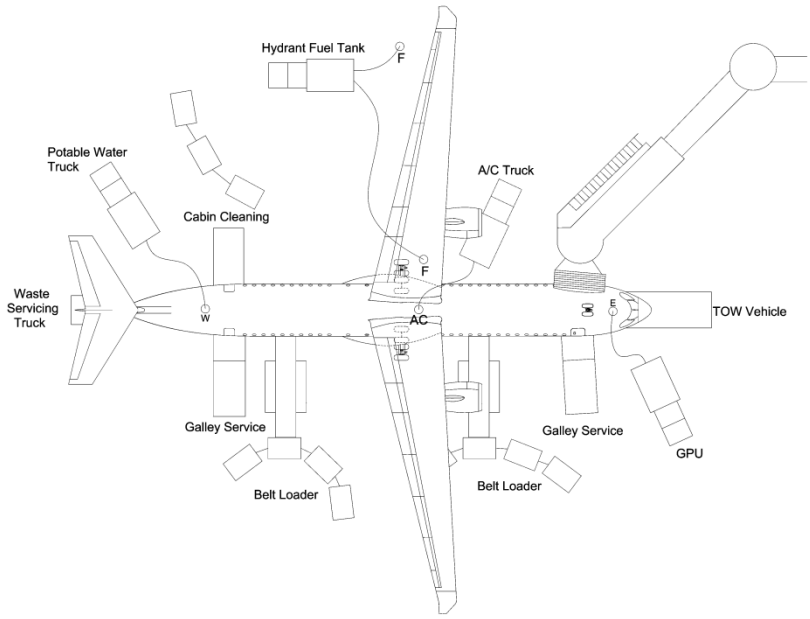

Fig. 75 Ground operation compatibility for Levant

Considering that the wingspan of the aircraft is smaller than 150', which is the standard runway width for medium and large airports, Levant is considered to be compatible with the majority of present day operating civilian runways and will not require any capital modifications to the runways worldwide.

Using the dimensions presented by *Roskam* for ground operational vehicles commonly utilized worldwide, a study was performed to ensure the compatibility of the configuration with

ground support vehicles. It was concluded that Levant with folded outboard wings is fully compatible with airport ground support systems worldwide and will not require a modification in ground operational procedures. Despite the fact that Levant uses an all-electric architecture, the ground power socket of Levant is compatible with the generic 150 V_{AC} ground power units available in airports.

As previously discussed in Sec. 10.1, Ibis utilizes HRJ biofuels. Although it is derived from a different source than traditional jet fuel, it does not require a new set of refueling/defueling ground support equipment because HRJ has the exact physical properties of regular aviation fuel. The HRJ biofuel proposed for Ibis is to be delivered to the consumers operation-ready, therefore eliminating the likelihood of blending mistakes made by the ground crew at the airport, which may result in engine operation complications.

13. Cost Analysis

13.1 Flight Path Optimization

Multiple parametric studies were performed in order to optimize the mission profile presented in Sec. 3.2. Given that the aircraft is expected to perform transport missions in a variety of ranges, a parametric study was performed to optimize cruise Mach number and initial altitude for both the 1,200 *nm.* nominal and 3,500 *nm.* maximum design ranges. In order to model the DOC of the aircraft as a function of the mission variables, such as average block speed and initial cruise altitude, the financial model provided by *Roskam*[105] for the estimation of research, technology, development, evaluation, acquisition, and operating costs was programmed into a dynamic spreadsheet. Methods presented in Sec. 10.2 with regard to the estimation of an environmental tax were also added to take into account the effects of flight path parameters on the DOC of Levant. Considering the previously mentioned results for the engine optimization, the DOC and the corresponding aircraft unit cost were computed for a range of Mach numbers and initial cruise altitudes. The result of these analyses is shown in Figs. 76 and 77.

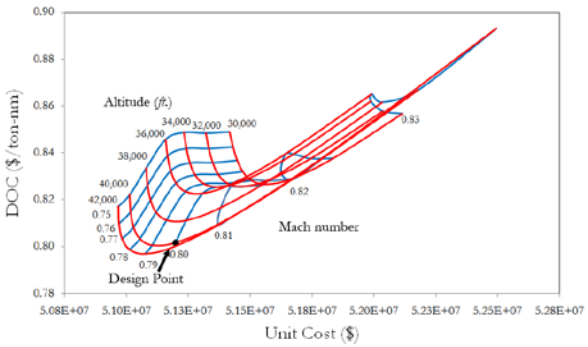

Fig. 76 DOC vs. unit cost for various initial cruise altitudes and Mach numbers, at a range of 3,500 *nm.* for a production run of 500 aircraft.

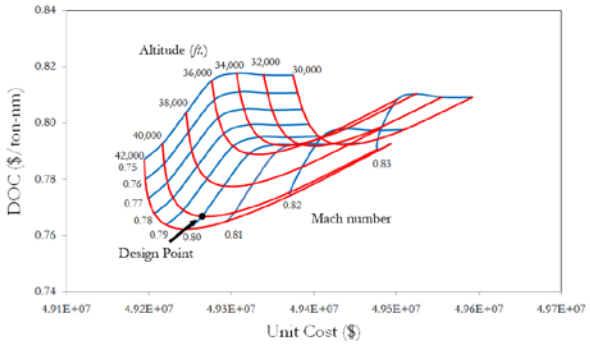

Fig. 77 DOC vs. unit cost for various initial cruise altitudes and Mach numbers, at a range of 1,200 *nm.* for a production run of 500 aircraft..

The analysis indicates that the DOC for maximum range missions rapidly declines as the aircraft starts to fly at higher altitudes and a Mach number in the neighborhood of 0.79. In the 1,200 *nm.* nominal range case, the DOC does not reduce as rapidly as the aircraft flies at higher altitudes. Instead of a Mach number of 0.79, the DOC would be minimized at a Mach number of 0.8 to 0.81. The analysis also indicates that the unit cost of Levant for a production run of 500 aircraft will be

impacted slightly by the chosen flight path parameters. This is due to the impact of the design Mach number and altitude on the structural weight of the aircraft, which in turn impacts the unit cost of the plane.

UACC recommends that Levant should be flown at a Mach number of 0.81, while flying missions near the nominal range of 1,200 *nm*. The results of the analysis presented in Figs. 76 and 77 indicate that the reductions in DOC due to increasing ICA are minimal above an altitude of 39,000'. Therefore, UACC recommends an ICA of 39,000' for Levant; however, higher cruise altitudes, if allowed by Air Traffic Control (ATC), will still improve the DOC of the aircraft. While flying missions near the maximum range of 3,500 *nm*., the aircraft will incur less cost and cause less environmental impact if it is operated at a lower Mach number of approximately of 0.79 and the highest altitude allowed by the ATC. Moreover, given its small fuel consumption achieved via the utilization of advanced propulsion and aerodynamic concepts, Levant will have an operating cost well below the commercial fleets it will replace.

13.2 Flyaway Cost Breakdown

Given the emphasis by the RFP placed on the competitiveness of flyaway and operating costs, attention was paid to the financial drivers in various stages of the design. *Roskam*'s[106] method was used to estimate the development and acquisition cost. The research and development includes the costs of engineering and design, development and support, prototypes and testing operations, and program financing. It was assumed that the research and technology development of the project will yield a 5% return over a period of three years, while the financing cost will be 7% of the total research and development cost of the project. Acquisition cost includes the costs associated with engineering and design for the manufacturing phase, production program, and test operations, as well as 15% finance fees and a 12% depreciation of invested capital. Sensitivity analysis was performed to assess the effect of variation of the difficulties factors defined by *Roskam* on the final

flyaway cost to estimate an uncertainty of the cost figures. The analysis was repeated for two production runs of 500 and 1,500 aircraft, the results of which can be seen in Table 21.

Table 21 R&D, acquisition and flyaway cost breakdown for Levant, assuming production runs of 500 and 1,500 aircraft

Cost Item	500 Production Run Cost (10^6 $)-2019 U.S. Dollar	1,500 Production Run Cost (10^6 $)-2019 U.S. Dollar
Research & Development Phase:		
Engineering & Design	225	225
Development, Support, & Testing	76	76
Prototype Aircraft	1,334	1,334
Test Operations	55	55
Finance Cost	338	338
R & D subtotal	*2,028*	*2,028*
Profit	225	225
Total	**2,253**	**2,253**
Acquisition Phase:		
Engineering & Design	275	514
Production Program	15,923	41,215
Test Operations	46	139
Finance Cost	2,867	7,388
Manufacturing Sub-Total	*19,111*	*49,256*
Profit	1,912	4,926
Total	**21,023**	**54,182**
Flyaway Cost per plane:		
Worst Case Scenario	52.9	38.1
Best Case Scenario	46.6	32.5
Uncertainty	±3.15	±2.80

To investigate the effects of the size of manufacturing on fly-away cost, analysis was performed for a large range of production runs. Figure 78 presents the results of this analysis assuming the highest values for all difficulty factors in *Roskam*'s method (i.e. the worst case scenario). For the purpose of comparison, the market price of the aircraft was also computed for a 20 year production run, assuming an average production rate of 220 planes per year.

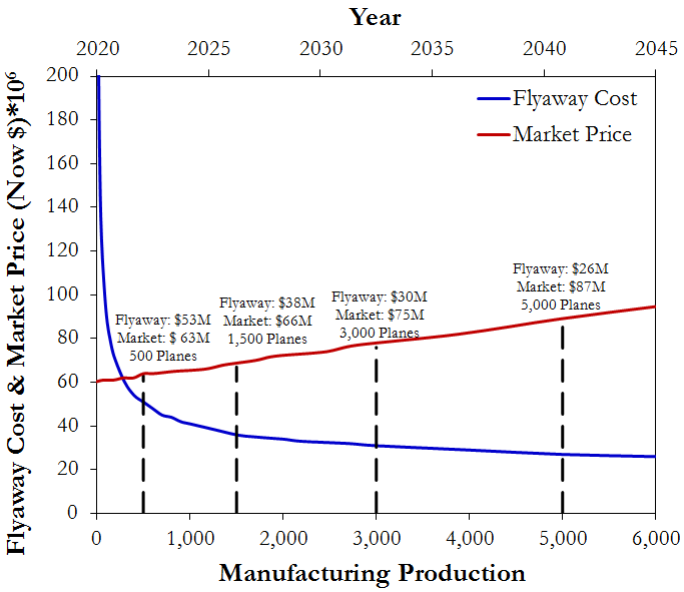

Fig. 78 Flyaway cost & market price vs. manufacturing production

13.3 Operating Cost Breakdown & Competitive Analysis

As requested by the RFP, the operation and maintenance costs of Levant were computed to assess its viability against current in-service aircraft. *Roskam*'s[107] method was used to perform DOC estimation for both biofuels and conventional JP-10 jet fuel. The cost of regular fuel was obtained by consulting the fuel cost projections obtained from the U.S. Energy Information Administration interactive web portal [108]. This portal presents projections for the cost of energy and main forms of fossil fuels assuming different economic scenarios, modeling the observed trends in energy supply and demand cycles. Reviewing these projections, it was determined that in 2020, an average jet fuel cost of 2.98 *$/gal.* will represent the middle ground between the worst and best economic scenarios. A study by E4tech Company[109] suggests that biofuels are cost comparable at present, but their demand will greatly exceed the production volume if they become commercially available. This study also indicates that the cost of HRJ related biofuels could be as low as 1.20 *$/gal.* Moreover, the maximum cost for HRJ related biofuels is considered to be dictated by the cost of jet fuel (which can be as high as 2.98 *$/gal*) to preserve competitiveness in the energy market. Furthermore, the study suggests that HRJ related biofuels will be available commercially by 2018, implying that by EIS these biofuels will be substantially cheaper than conventional aviation fuel. Concluding from this study, UACC chose a cost of 2.09 *$/gal.* for HRJ related biofuels. The environmental tax model presented in Sec 10.2 was implemented to account for the benefits incurred by utilization of lower carbon footprint biofuels and flying at higher altitudes.

DOC analyses were performed for Levant using both conventional aviation fuel and HRJ related biofuels. Similar cost estimations were performed on the Boeing 737 and Airbus A320, assuming comparable utilization times. Table 22 (on the following page) presents the results of DOC comparison analyses for a production run of 500 aircraft.

Table 22 Results of DOC comparison analysis for Airbus A320-200, Boeing 737-800, Levant with conventional jet fuel, and Levant with HRJ related biofuels

Cost Item	Airbus A320-200	Boeing 737-800	Levant (Jet Fuel)	Levant (Biofuels)	Average Change from Today's Competitors (Jet Fuel, Biofuel)
Annual Utilization (*nm.*)	1,865,256	1,891,081	1,807,932	1,807,932	-------
Crew (*$/nm.*)	0.96	0.95	0.61	0.61	-36%, -36%
Fuel, Oil, & Env. Tax (*$/nm*)	4.53	3.85	2.91	1.07	-31%, -74%
Insurance (*$/nm.*)	0.15	0.15	0.57	0.57	+280%, +280%
Maintenance (*$/nm.*)	2.96	2.84	3.33	3.56	+15%, +23%
Depreciation (*$/nm.*)	4.93	4.68	2.33	2.34	-52%, -51%
Landing & Navigation Fees ($)	0.40	0.36	0.38	0.38	-------
Total DOC[*] (*$/nm*)	**15.03**	**13.85**	**10.13**	**7.92**	**-30%, -45 %**

From this analysis, it was concluded that Levant will present extreme reductions in DOC thanks to reductions in TSFC (~35%) and an increase in cruise L/D (~25%). It is also shown that the DOC of Levant could be reduced by as much as 4% as a consequence of using biofuels. It should be noted that this analysis is only valid for the 2020 market, and this difference will increase as oil prices rise and HRJ related biofuels become more available economically.

[*] Including the Financing Cost with a rate of 7 percent.

14. Future Recommendations

To improve the certainty of the analysis pertaining to the viability of NLF wings (i.e. to identify the location of transition to turbulence on the upper and lower surface with more accuracy), UACC would like to suggest the utilization of CFD tools with more diverse control over turbulence parameters, as well as superior hardware compatibility allowing for cluster computing. At present, the accuracy of the results presented in this proposal is limited by the maximum computing power accessible by the team. Although some of the analyses presented in this volume have required CPU times well above 40 hours, UACC realizes that, given the relatively low number of fluid cell elements (~1.7 million), these results have to be more accurate to provide applicable transition predictions. There is also potential for research and development into cleaning procedures (on ground or in flight) to ensure the cleanliness of the wing surfaces. Such measures may be critical to the maintenance of laminar flow on the surfaces of the aircraft, although arguments for and against the level of cleanliness has been presented in various sources of literature[110,111]. More modern propulsion elements, such as recuperated and intercooled engine core concepts, may also be utilized to increase the efficiency of the engines beyond the presented performance in this proposal. Other concepts such as inlet water injection may also be utilized to effectively reduce NOx emission levels. As discussed in Sec. 5.1, the unique engine integration of Levant allows for further expansions of payload capacity with no need to redesign the empennage or wing structure, making Levant capable of future expansions as the market may demand.

15. References

[1] *Roskam, Jan.*, Airplane Design, Part I through VIII , DAR Corporation, 2003.

[2] *Heinemann, E., Raussa, R. and Van Every, K.,* Aircraft Design, The Nautical and Aviation Publication Co., 1985.

[3] *Eppinger, Steven D.* and *Ulrich, Karl T.*, Product Design and Development, Second Edition, Irwin McGraw-Hill, Boston, 2000.

[4] *Redeker, G.* and *Wichmann, G.* "Forward Sweep – A Favorable Concept for a Laminar Flow Wing." Journal of Aircraft, Vol. 28 № 2, 1991.

[5] "Engineering Science Data Unit", Series 3. *Volumes on Aerodynamics,* items 91014. "Maximum Lift of Wings with Trailing-Edge Flaps at Low Speeds". *IHS* Inc., 1995.

[6] *Edi, Prasetyo, Fielding, J.P.* Civil-Transport Wing Design Concepts. Journal of Aircraft Vol. 43, № 4. July-August 2006.

[7] "Engineering Science Data Unit", Series 3. *Volumes on Aerodynamics,* items 77028 Amendment F. "Geometric Characteristics of Typical Bodies". IHS Inc., July 1990.

[8] Pratt & Whitney Technical Brochure titled Pure Power PW1000g. Dec. 2008.

[9] *Redeker*, *G.*, *Horstmann, K.H.*, *Köster*, *H.*, and *Quast A.* Investigations on High Reynolds Number Laminar Flow Airfoils. Journal of Aircraft Vol. 25 № 7. July 1988.

[10] *Lehner*, *Stephan* and *Crossley*, *William*. Hybrid Optimization for a Combinatorial Aircraft Design Problem. Proceedings of 9th AIAA Aviation Technology, Integration, and Operations Conference. 21-23 September 2009

[11] *Holmes, B.J.* Observations and Implications of Natural Laminar Flow on Practical Airplane Surfaces. Journal of Aircraft Vol. 20 №. 12. December 1983.

[12] *Roskam*, *Jan.* Airplane Design Part VI Sec. 4.2 p. 23-43. DAR Corporation. 1990.

[13] Appendix to Request for Proposal Document for Team Aircraft Design Competition. AIAA. 2008-2009.

[14] "Engineering Science Data Unit". *Volumes on Performance,* item 73018. "Introduction to Estimation of Range and Endurance".

[15] "Engineering Science Data Unit". *Volumes on Performance,* item 73019. "Approximate Methods for Estimation of Cruise, Range, and Endurance".

[16] "Engineering Science Data Unit". *Volumes on Performance,* items 74018. "Lost Range, Fuel, and Time Due to Climb and Descent".

[17] *Roskam*, *Jan.* Airplane Design, Part V Ch. 2 p. 3-17. DAR Corporation. 1999.

[18] *Godston*, *J.*, and *Reynolds*, *C.* Propulsion System Integration Configurations for Future Prop-Fan Powered Aircraft. Proceedings of AIAA/SAE/ASME 19th Joint Propulsion Conference. Seattle Washington. June 27-29. 1983.

[19] *Roskam*, *Jan.* Airplane Design Part I Sec. 341 p. 118-187. DAR Corporation. 1987.

[20] *Roskam*, *Jan.* Airplane Design Part II Fig. 12.7 p.286. DAR Corporation. 1997.

[21] "Engineering Science Data Unit". *Volumes on Performance,* item 73019. "Approximate Methods for Estimation of Cruise Range and Endurance: Aeroplanes with Turbo-Jet and Turbo-Fan Engines." Amendment C. May 1982.

[22] *Roskam*, *Jan.* Airplane Design Part I Sec. 3.2 p 94. DAR Corporation 1997.

[23] "Engineering Science Data Unit". *Volumes on Aerodynamics,* item 95021. "Wing Lift Coefficient Increment at Zero Angle of Attack"

[24] "Engineering Science Data Unit". *Volumes on Transonic Aerodynamics,* item 74013. "A Method For Estimating Drag-rise Mach Number at Zero Incidence of Smooth or Bumpy Non-Ducted Axisymmetric Bodies Without or With Fins", Aug 1974.

[25] "Engineering Science Data Unit". *Volumes on Transonic Aerodynamics,* item 83017. "The Wave Drag Coefficient of Spherically Blunted Secant Ogive Forebodies of Fineness Ratio 1.0, 1.5, and 2.0 at Zero Incidence in Transonic Flow." Amendment A. October 1992.

[26] *Dodbele*, *Simha*. Design Optimization of Natural Laminar Flow Bodies in Compressible Flow. Journal of Aircraft. Vol. 29 № 3. May-June 1992.

[27] *Edi, Prasetyo, Fielding, J.P.* Civil-Transport Wing Design Concepts. Journal of Aircraft Vol. 43, № 4. July-August 2006.

[28] *Lee*, *Jae-Moon*, *Schrage*, *Daniel* and *Mavris*, *Dimitri.* Development of Subsonic Transports with Natural Laminar Flow Wings. AIAA Journal 98-0406. 1997.

[29] *Lehner*, *Stephan* and *Crossley*, *William*. Hybrid Optimization for a Combinatorial Aircraft Design Problem. Proceedings of 9th AIAA Aviation Technology, Integration, and Operations Conference. 21-23 September 2009.

[30] *Huenecke*, *Klaus*. Modern Combat Aircraft Design. p. 47 fig. 4-14. Airlife Publishing Ltd. England. 1987.

[31] *Lehner*, *S*., and *Crossley*, *W*. "Combinatorial Optimization to Include Greener Technologies in a Short-to-Medium Range Commercial Aircraft." ICAS 2008-4.10.2, ICAS 2008 Congress including the 8th AIAA 2008 ATIO Conference. Anchorage, AK. September 15-18, 2008.

[32] McDonnell Douglas Aero Methods Manual TP-68, 1982. The compressibility drag model was derived by Mark Page. Weight relations and propulsion models originated from "Fundamentals of Flight" by Shevell, 1989.

[33] *Roskam*, *Jan*. citing *Torenbeek*, *E*. Synthesis of Subsonic Airplane Design. Appendix G, p. 533. 1981.

[34] *Roskam*, *Jan*. Airplane Design. Part VI. DAR Corporation. 1990. All Sections relevant to Class II drag polar analysis for commercial jets were used.

[35] *Torenbeek*, *E*. Synthesis of Subsonic Airplane Design. Chapters pertaining to low speed aerodynamic predictions. 1981.

[36] *Roskam*, *Jan*. Airplane Design. Part VI. DAR Corporation. 1990. All sections presenting a model for relationships between drag and Mach number.

[37] *Morgan*. Turbojet Fundamentals. Douglas Aircraft Company, Inc. Santa Monica, CA. 1956.

[38]*McKay, Bruce.ds*, *C*. Next Generation Propulsion & Air Vehicle Considerations.Proceedings of AIAA/SAE/ASME 19th Joint Propulsion Conference. Denver Colorado. August 2-5. 2009.

[39] *A. Bonaccorsi*, *P. Giuri, and F. Pierotti*, Discontinuities, Convergence and Survival of Inefficient Trajectories in Aeroengine Selection. Economics and Management Laboratory, Santa Anna School of Advanced Studies, Pisa, Italy, Sep. 2001.

[40] *Garber, Edwin J.,* Overview of NASA PTA Open fan Flight test Program, NASA Technical Note № 2-25536, 1988.

[40] New Short Range Project intending to replace the A320 series by 2018.

[41] *Robert Wall, Michael A. Taverna, and Guy Noris,* "Push or Pull: Airbus & Boeing Vision Split on Open-Rotor Applications", Aviation Weekly, May 4th 2009.

[42] *F. Holste, W. Neise*, "Noise Source Identification in a Open fan Modeled by Means of Acoustic Near Field Meassurements", Journal of Sound and Vibration №203(4), 1997.

[43] *Garber, Edwin J.,* Overview of NASA PTA Open fan Flight test Program, P-365. NASA Technical Note № 2-25536, 1988.

[44] Douglass Barie, and Guy Noris, "Sound and Vision", Aviation Weekly, Oct. 13, 2008.

[45] *Robert Wall, Michael A. Taverna, and Guy Noris,* "Push or Pull: Airbus & Boeing Vision Split on Open-Rotor Applications", Aviation Weekly, May 4th 2009.

[46] Committee of Aeronautical Technologies, Aeronautics and Space Engineering Board, Commission on Engineering and Technical Systems, National Research Council of Aeronautical Technology for the Twenty-First Century National Academy Press, Washington, D.C. 1992.

[47] *Emily Schwartz, and Ilan M. Kroo,* Aircraft Design: Trading Cost and Climate Impact, presented at the 47th AIAA aerospace Science meeting, Jan. 5-9 2009, Stanford University

[48] Pratt & Whitney Technical Brochure titled Pure Power PW1000g. Dec. 2008.

[49] *Schwartz, Emily and Kroo , Ilan M.* Aircraft Design: Trading Cost and Climate Impact. Proceedings at the 47th AIAA Aerospace Science meeting, Stanford University Jan. 5-9, 2009.

[50] *J. Seddon E. L. Goldsmith,* "Intake Aerodynamics", AIAA Education Series, Reston, VA, 2007.

[51] *Collie, Wallis V*., et al. Advanced Propulsion System Design and Integration For a Turbojet Powered Unmanned Aerial Vehicle. Proceedings of the 41st Aerospace Science Meeting and Exhibit. Reno, Nevada. January 6-9. 2003.

[52] Committee of Aeronautical Technologies, Aeronautics and Space Engineering Board, Commission on Engineering and Technical Systems, National Research Council of Aeronautical Technology for the Twenty-First Century National Academy Press, Washington, D.C. 1992.

[53] *Schwartz, Emily and Kroo , Ilan M.* Aircraft Design: Trading Cost and Climate Impact. Proceedings at the 47th AIAA Aerospace Science meeting, Stanford University Jan. 5-9, 2009.

[54] *Moir*, *Ian* and *Seabridge, Allan.* Aircraft Systems: Mechanical, Electrical , and Avionics Subsystems Integration Third Edtion. 2008.

[55] *Srimoolanathan*, *Balaji*. Aircraft Electrical Power Systems-Charged with Opportunities. Frost & Sullivan. p.2. 2008.

[56] *Moir*, *Ian* and *Seabridge, Allan.* Aircraft Systems: Mechanical, Electrical , and Avionics Subsystems Integration Third Edtion. 2008.

[57] *Moir*, *Ian* and *Seabridge, Allan.* Aircraft Systems: Mechanical, Electrical , and Avionics Subsystems Integration Third Edtion. 2008.

[58] *Ensign*, *Thomas*. Peformance and Weight Impact of Electrial Environmental Control System and More Electric on Citation CJ2. Proceeedings of the 45th AIAA Aerospace Sciences Meeting and Exhibit. January 8-11, 2007.

[59] *Sinnett*, *Mike*. 787 No-Bleed Systems: Saving Fuel and Enhancing Operational Efficiencies. Boeing Aeromagazine. Iss. 28 Quarter 4. 2007.
[60] *Cronin*, *Michael J.* All-Electric vs Conventional Aircraft: The Production/Operational Aspects. Lockheed-California Co. June, 1983.
[61] *Garrison*, *Michael* and *Steffan*, *Scot*. Two-Fault Tolerant Electric Actuation Systems for Space Applications. Proceeding of the 42nd AIAA/ASME/SAE/ASEE Joint Propulsion Conference and Exhibit. July 9-12, 2006.
[62] "Engineering Science Data Unit". *Volumes on Aircraft Performance,* item 83042. "Estimation of Spray Patterns Generated from the Sides of Aircraft Tires Running in Water or Slush." Amendment A. April, 1998.
[63] *Moir*, *Ian* and *Seabridge, Allan.* Aircraft Systems: Mechanical, Electrical , and Avionics Subsystems Integration Third Edtion. 2008.
[64] *Heimbold, R.L., Cronin, M.J., and Howison, W*. Study of the Application of Advanced Electrical/Electronic Technologies to Conventional Aircraft. NASA/JSC/Lockheed NAS-9-15863, July 1979.
[65] *Howison, W.W*. and *Cronin, M.J.* Electronic/Electric Technology Benefits Study. NASA-LRC/Lockheed NAS-16199. Jan. 1982.
[66] *Cronin*, *Michael J.* All-Electric vs Conventional Aircraft: The Production/Operational Aspects. Lockheed-California Co. June, 1983.
[67] Roskam, Jan. Airplane Design Part V. Section 5. 1999.
[68] *Raman Raj et al*. The effects of Advanced Materials on Airframe Operating and Support Costs. The RAND Corporation, Santa Monica, CA. 2003.
[69] Advanced Aircraft Analysis help file on Structure. DAR Corporation. Keyword Libove's Axis. Wichita, Kansas. 2009.
[70] "Engineering Science Data Unit". *Volumes on Aerodynamics,* item 83040. "Method for the Rapid Estimation of Spanwise Loading of Wings with Camber and Twist in Subsonic Attached Flow". Amendment C. July 1995.
[71] *Noll, T. E., Eastep, F. E.,* and *Calico, R. A.* Active Suppression of Aeroelastic Instabilities on a Forward-Swept Wing. Journal of Aircraft. Vol. 21№ . March 1984.
[72] *Harris, G.* "Flutter Criteria for Preliminary Design," LTV Aerospace Corporation, Voughts Aeronautics and Missile Division, Engineering report 2-53450/3R-467 under Bureau of Naval Weapons Contract NOW 61-1072C, September 1963.
[73] *Liebeck, R. H., Page, M.A., Rawdon, Blaine K., Scott, Paul W., and Wright Robert A.*, "Concepts for Advanced Subsonic Transports," NASA CR-4628, McDonnell Douglas Corporation, Long Beach, CA, September 1994.
[74] *Griffen, Kenneth E.* and *Eastep, Franklin E.* Active Control of Forward-Swept Wing with Divergence and Flutter Aeroelastic Instabilities. Journal of Aircraft. Vol. 19 № 10. October 1982.
[75] Per suggestion of Mr. Blaine Rawdon, Technical Fellow, Boeing Commercial Aircraft.
[76] *Roskam*, *Jan.* Airplane Flight Dynamics and Automated Flight Controls. Part I Sec. 4.2.2. p. 205. 2003
[77] Per suggestion of Mr. Mark Page, Chief Scientist, Swift Engineering.
[78] Military Specification MIL-F-8785 B Flying Qualities of Piloted Airplanes; 1969: Air Force Flight Dynamics Laboratory, WP AFB, Dayton, Ohio.
[79] *Roskam, J.* Airplane Flight Dynamics and Automatic Flight Controls, Part I, DAR Corporation, 2003, p. 186.
[80] *Roskam, J.* Airplane Flight Dynamics and Automatic Flight Controls, Part I, DAR Corporation, 2003, p. 143.
[81] Military Specification MIL-F-8785 B Flying Qualities of Piloted Airplanes; 1969: Air Force Flight Dynamics Laboratory, WP AFB, Dayton, Ohio.
[82] *Roskam, J.* Airplane Flight Dynamica and Automatic Flight Controls, Part I, DAR Corporation, 2003, p. 205.
[83] *Hoak. D.E.,*"USAF Stability and Control DATCOM, Write Paterson AFB, OH.
[84] *J. Roskam,* Airplane Flight Dynamics and Automatic Flight Controls Part I, Section 5.2.4 & 5.2.5 PP 329-337 DAR Corp. 2003.
[85] International Air Transport Association Report on Alternative Fuels. p. 1. 2009.
[86] International Air Transport Association Report on Alternative Fuels. p. 34. 2009.
[87] Air Traffic Action Group. Beginner's Guide to Aviation Biofuels. p.6. May 2009.
[88] E4tech. Review of the Potential for Biofuels in Aviation for the Committee on Climate Change. P. 37. August 2009.
[89] E4tech. Review of the Potential for Biofuels in Aviation for the Committee on Climate Change. P. 51. August 2009.
[90] E4tech. Review of the Potential for Biofuels in Aviation for the Committee on Climate Change. P. 60. August 2009.
[91] Air Traffic Action Group. Beginner's Guide to Aviation Biofuels. p.10. May 2009.

[92] International Air Transport Association Report on Alternative Fuels. p. 42. 2009.
[93] Univeristy of Virginia. Algae: Biofuel or the Future? Science Daily June 2, 2010.
[94] E4tech. Review of the Potential for Biofuels in Aviation for the Committee on Climate Change. P. 59. August 2009.
[95] International Air Transport Association Report on Alternative Fuels. p. 35. 2009.
[96] International Air Transport Association Report on Alternative Fuels. p. 50. 2009.
[97] *Schwartz, Emily* and *Kroo , Ilan M.* Aircraft Design: Trading Cost and Climate Impact. Proceedings at the 47th AIAA Aerospace Science meeting, Stanford University Jan. 5-9, 2009.
[98] *Banke, Jim.* Shhhh! Keep It Down, Please. NASA news topics on aeronautics. http://www.nasa.gov/topics/aeronautics/features/aircraft_noise.html. Retrieved May 2010.
[99] "Engineering Science Data Unit". *Volumes on Performance,* item 85029. "Calculation of Ground Performance in Takeoff and Landing". Amendment A. March 2006.
[100] "Engineering Science Data Unit". *Volumes on Aerodynamics,* item 71007. "Low Speed Normal Force and Itching Moment of Slender Wings in Ground Effects". June 1971.
[101] *Roskam*, *Jan.* Airplane Design Part VII Sec. 5.2 p. 117-123. DAR Corporation. 1991.
[102] *Berton, Jeffrey J.* and *Envia, Edmane.* An Analytical Assessment of NASA's N+1 Subsonic Fixed Wing Project Noise Goal. Proceedings of the 15th AIAA/CEAS Aeroacoustics (30th AIAA Aeroacoustics) Conference. May 11-13, 2009.
[103] Engineering Science Data Unit". *Volumes on Performance,* item 84040. "First Approximation for Landing Field Length for Civil Transport Airplanes (50 ft, 15.24 m screen)". December 1984.
[104] *Roskam*, *Jan.* Aircraft Design Part II Sec. 11.3. p. 267-268. DAR Corporation. 1997.
[105] *Roskam Jan.*, Airplane Design Part VIII ; Section 5.2.4; DAR Corporation. 1990.
[106] *Roskam Jan.*, Airplane Design Part VIII ; Section 4.2 P 50-54; 1999.
[107] *Roskam*, *Jan.* Airplane Design Part VIII. DAR Corporation 1990.
[108] U.S. Energy Information Administration, independent statistics and analysis. Annual Energy Outlook. May 11, 2010.
[109] E4tech. Review of the Potential for Biofuels in Aviation for the Committee on Climate Change. P. 76. August 2009.
[110] *Holmes*, *B.J.* and *Obara*, *C.J.* Observations and Implications of Natural Laminar Flow on Practical Airplane Surfaces. AIAA Journal of Aircraft. Vol 20 № 12. December 1983.
[111] *Hermanspann*, *Fred.* Rain Effects on Natural Laminar Flow Airfoils. Proceedings of the AIAA 34th Aerospace Sciences Meeting and Exhibit. Jan 15-18, 1996.

University of Southern California Advanced Commercial Concepts	Phillip Adkins Aero Acoustics	Todd Erickson Propulsion	Darin Gaytan Aero Performance	Sina Golshany Lead Designer	Kieth Holmlund High Speed Aero
Levant	Kristina Larson Management	Devin Lewis Payload	Chris Nsavu Structures	John Roehrick Weight	Michael Zarem Systems

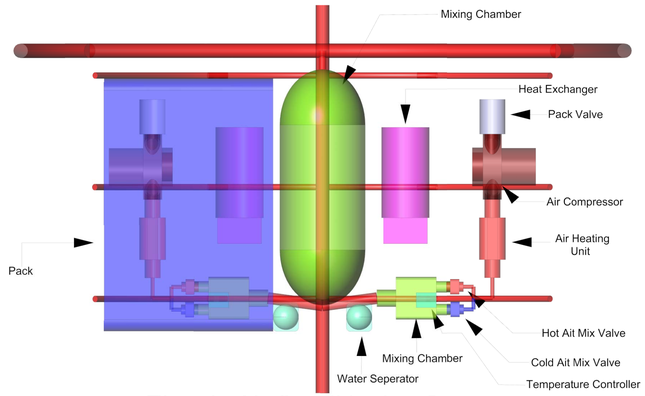

Electric Air Conditioning System

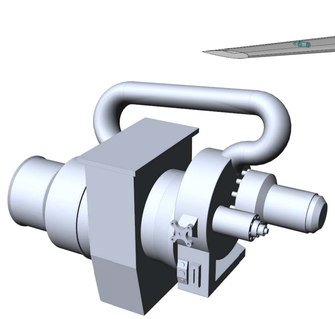

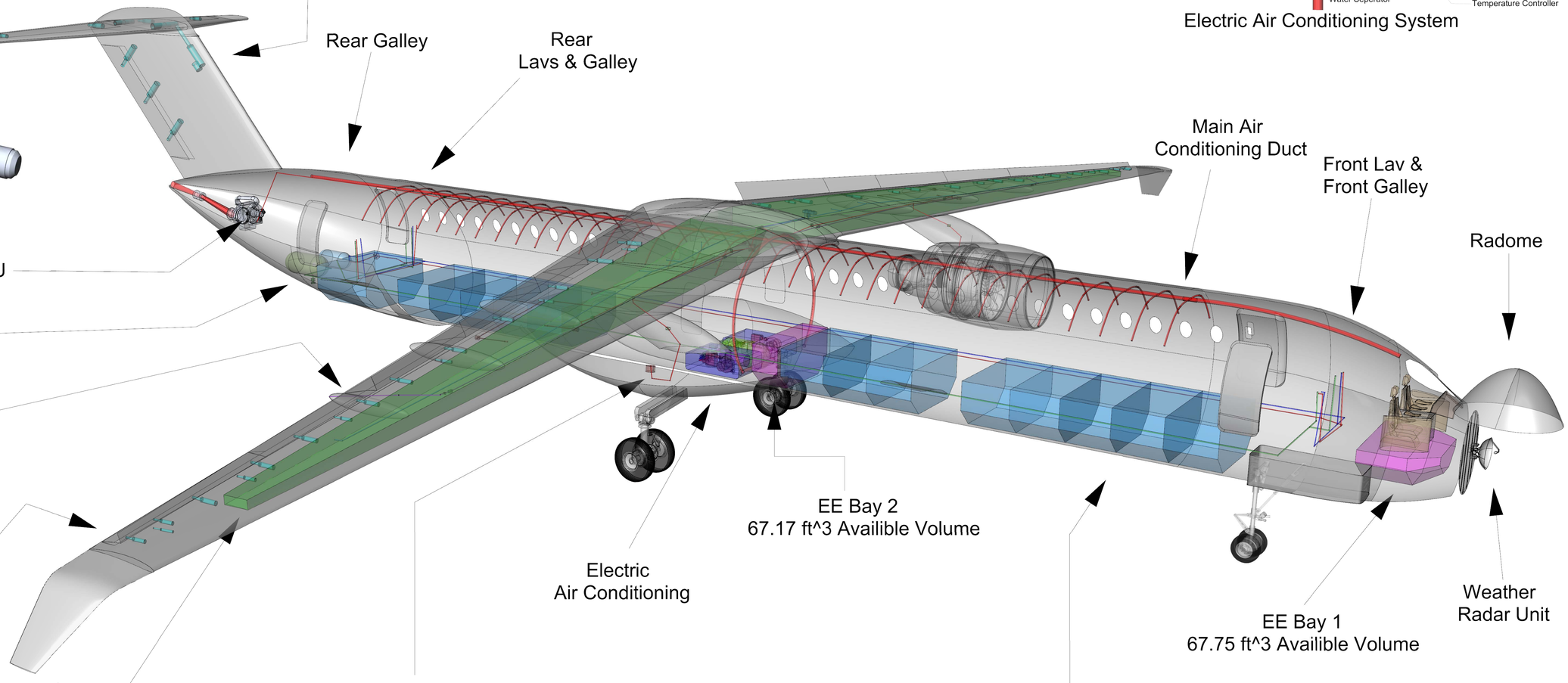

Systems Cutaway	SY - 1.0 10 JUNE 2010

University of Southern California
Advanced Commercial Concepts

Levant

Phillip Adkins Aero Acoustics	Todd Erickson Propulsion	Darin Gaytan Aero Performance	Sina Golshany Lead Designer	Kieth Holmlund High Speed Aero
Kristina Larson Management	Devin Lewis Payload	Chris Nsavu Structures	John Roehrick Weight	Michael Zarem Systems

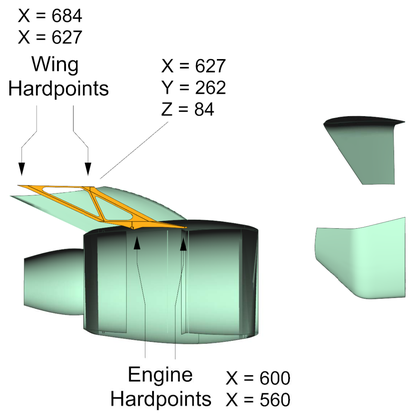

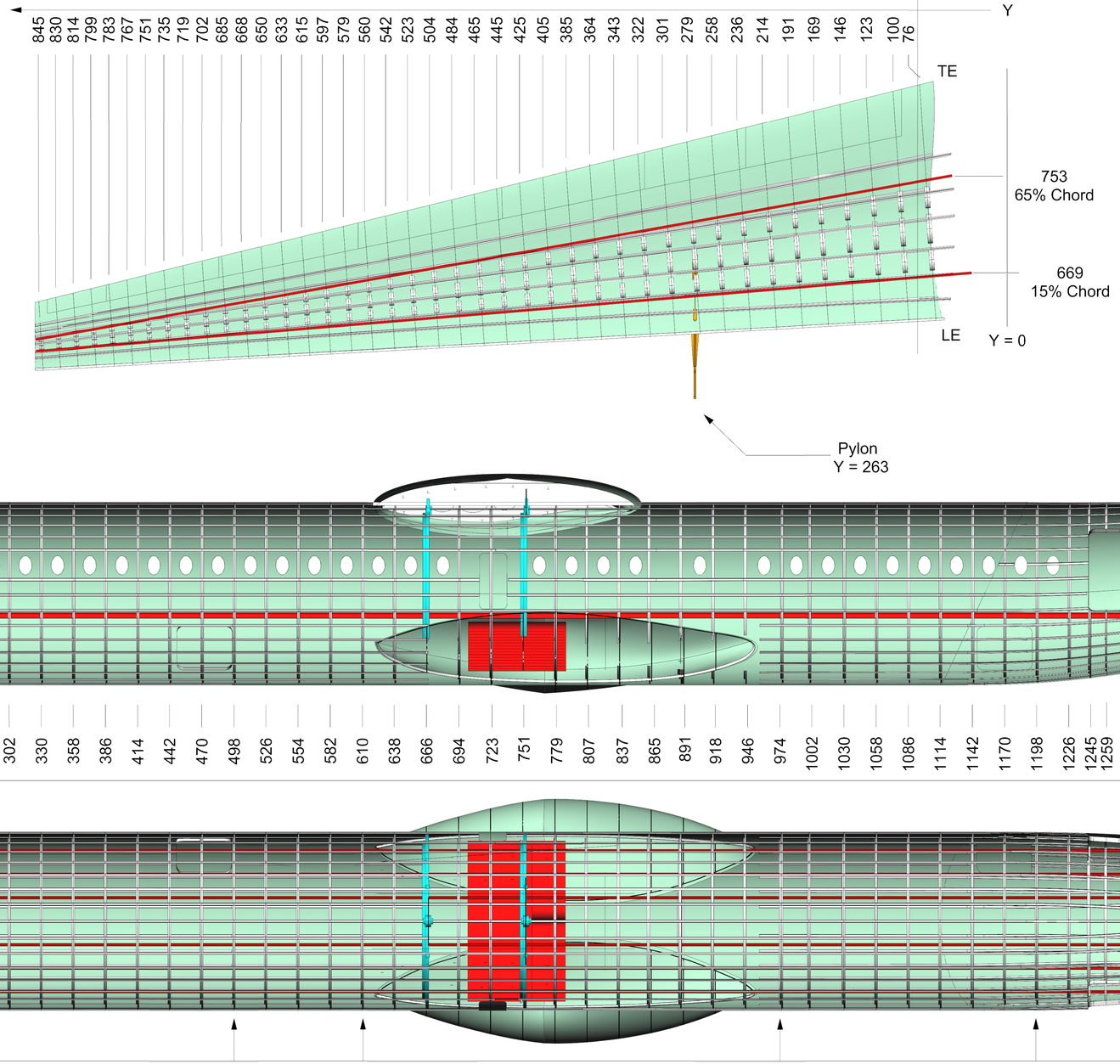

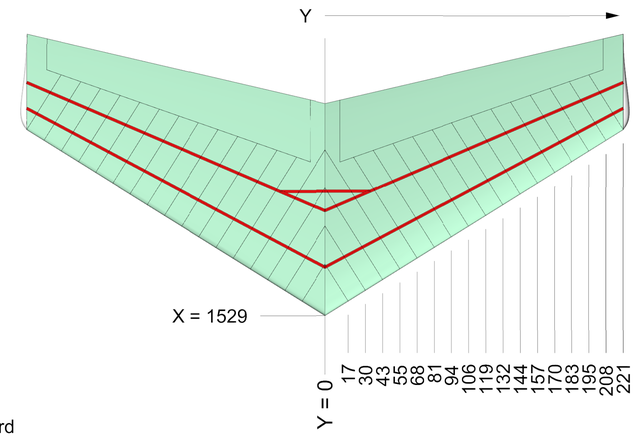

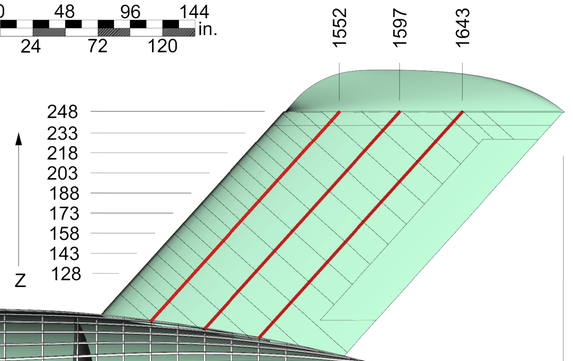

Structural Layout

S - 1.0

10 JUNE 2010

University of Southern California
Advanced Commercial Concepts

Levant

Phillip Adkins Aero Acoustics	Todd Erickson Propulsion	Darin Gaytan Aero Performance	Sina Golshany Lead Designer	Kieth Holmlund High Speed Aero
Kristina Larson Management	Devin Lewis Payload	Chris Nsavu Structures	John Roehrick Weight	Michael Zarem Systems

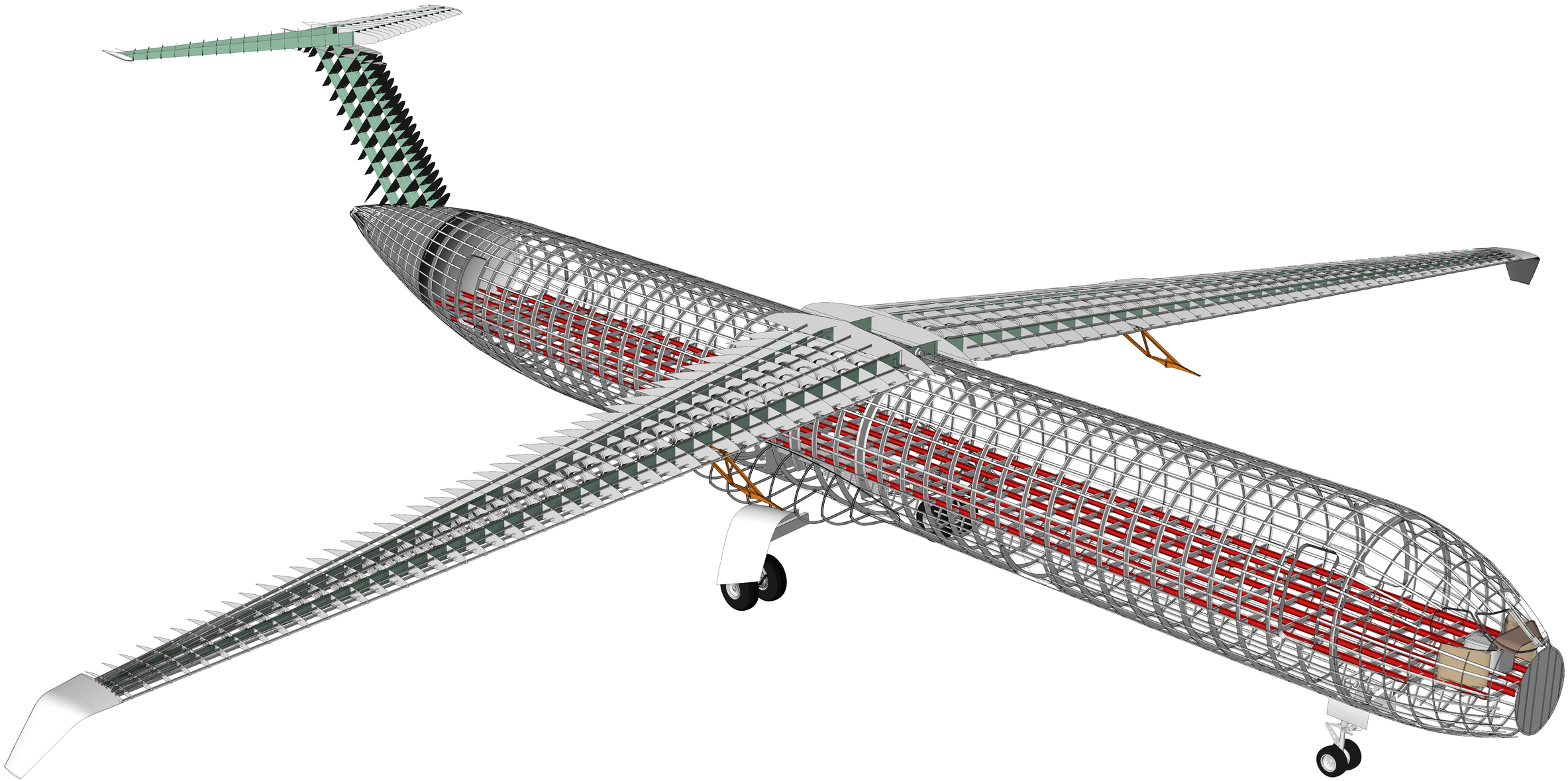

Structural Isometric

S - 2.0
10 JUNE 2010

University of Southern California
Advanced Commercial Concepts

Levant

Phillip Adkins Aero Acoustics	Todd Erickson Propulsion
Darin Gaytan Aero Performance	Sina Golshany Lead Designer
Kieth Holmlund High Speed Aero	Kristina Larson Management
Devin Lewis Payload	Chris Nsavu Structures
John Roehrick Weight	Michael Zarem Systems

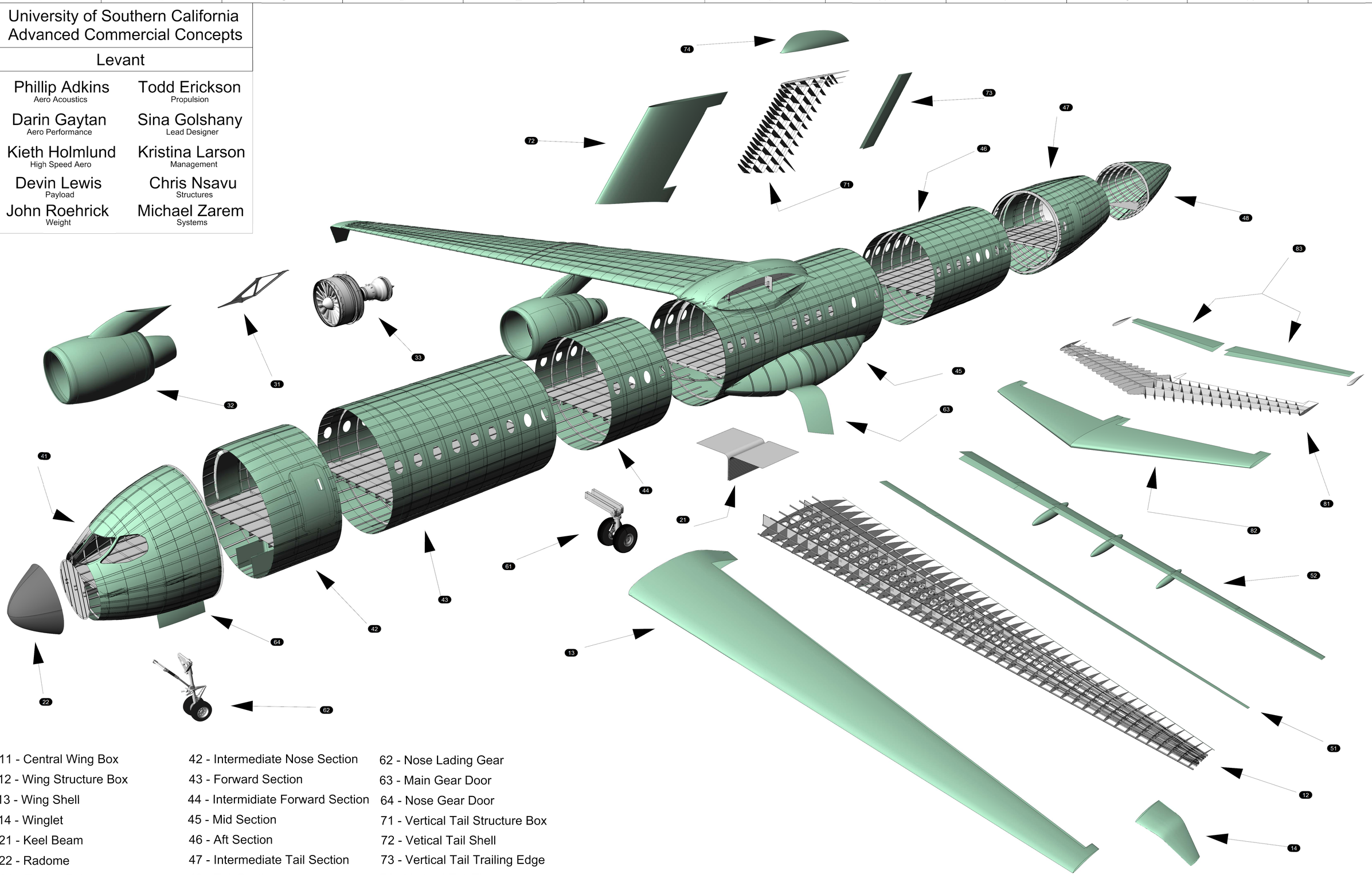

11 - Central Wing Box	42 - Intermediate Nose Section	62 - Nose Lading Gear
12 - Wing Structure Box	43 - Forward Section	63 - Main Gear Door
13 - Wing Shell	44 - Intermidiate Forward Section	64 - Nose Gear Door
14 - Winglet	45 - Mid Section	71 - Vertical Tail Structure Box
21 - Keel Beam	46 - Aft Section	72 - Vetical Tail Shell
22 - Radome	47 - Intermediate Tail Section	73 - Vertical Tail Trailing Edge
31 - Engine Pylon	48 - Tail Section	74 - Vertical Tail Tip
32 - Engine Nacelle	51 - Spoilers	81 - Horizontal Tail Structure Box
33 - Built-Up Engine	52 - Wing Trailing Edge	82 - Horizontal Tail Shell
41 - Nose Section	61 - Main Landing Gear	83 - Horizontal Tail Trailing Edge

Manufacturing Breakdown

M - 1.0

University of Southern California
Advanced Commercial Concepts

Levant

Phillip Adkins — Aero Acoustics
Todd Erickson — Propulsion
Darin Gaytan — Aero Performance
Sina Golshany — Lead Designer
Kieth Holmlund — High Speed Aero
Kristina Larson — Management
Devin Lewis — Payload
Chris Nsavu — Structures
John Roehrick — Weight
Michael Zarem — Systems

Potable Water System

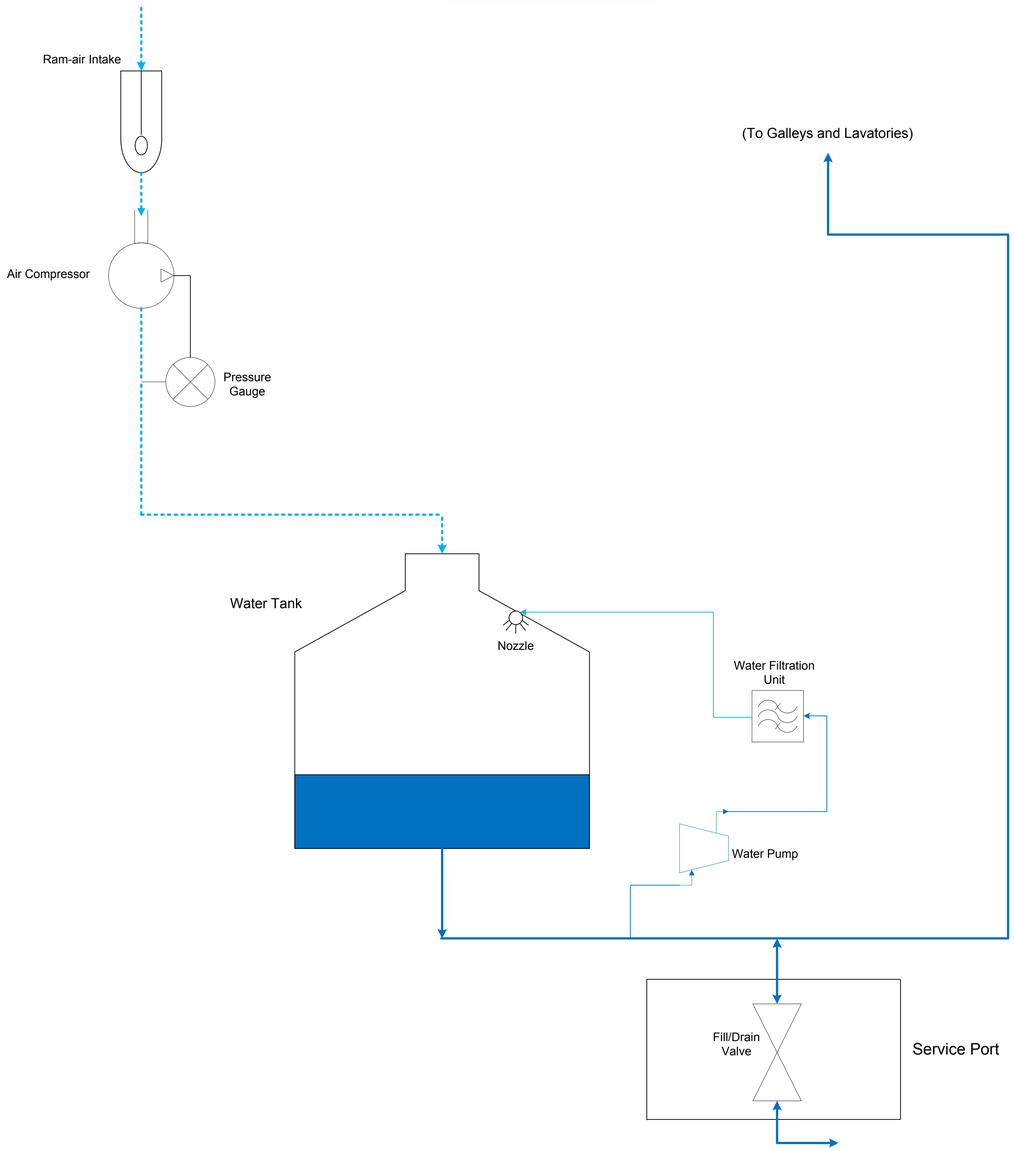

Waste System

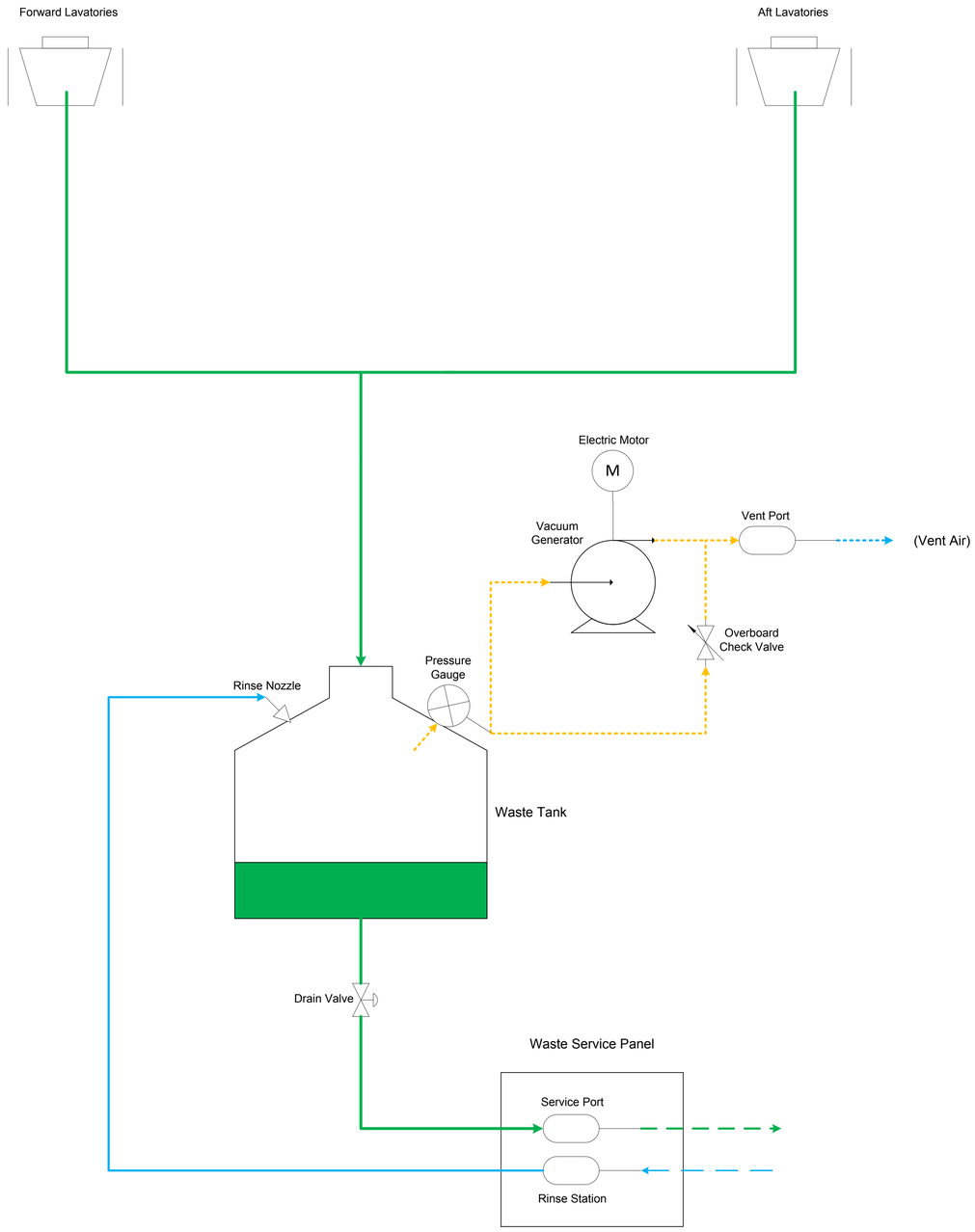

Potable Water and Waste Systems Schematic

SY – 6.0
10 JUNE 2010

University of Southern California
Advanced Commercial Concepts

Levant

Phillip Adkins — Aero Acoustics
Todd Erickson — Propulsion
Darin Gaytan — Aero Performance
Sina Golshany — Lead Designer
Kieth Holmlund — High Speed Aero
Kristina Larson — Management
Devin Lewis — Payload
Chris Nsavu — Structures
John Roehrick — Weight
Michael Zarem — Systems

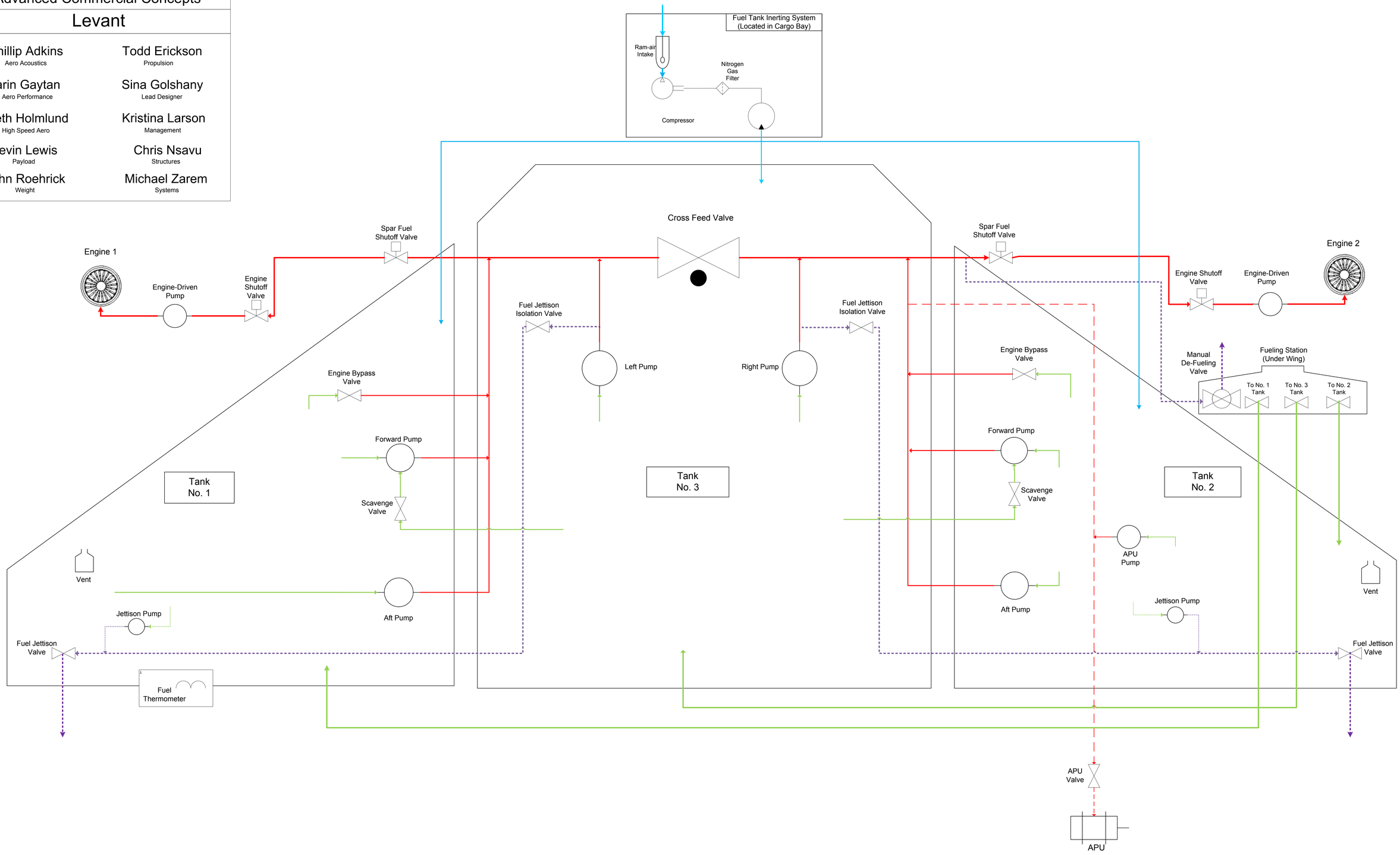

Fuel System Schematic

SY – 5.0

10 JUNE 2010

University of Southern California
Advanced Commercial Concepts

Levant

Phillip Adkins — Aero Acoustics
Todd Erickson — Propulsion
Darin Gaytan — Aero Performance
Sina Golshany — Lead Designer
Kieth Holmlund — High Speed Aero
Kristina Larson — Management
Devin Lewis — Payload
Chris Nsavu — Structures
John Roehrick — Weight
Michael Zarem — Systems

Legend:

PFCC -- Primary Flight Control Computer

FEU -- Flap Electronics Unit

ACE -- Actuator Control Electronics

AFDC -- Autopilot & Flight Director Computer

Note:
Colors schemes are used to differentiate between separate, but similar or redundant sub-systems. Due to the vast number of sub-systems represented in this diagram, some colors are used for more than one sub-system but do not indicate a direct relationship.

Flaperon Actuators (x2 per surface)

Low-Speed

High-Speed

← Spoiler Actuators

← Flap Actuators

Spoiler Actuators →

Flap Actuators →

M

FEU 1

FEU 2

Flap Electronics Units: These computers control the flap position based on flight deck inputs.

Flaperons: Surface control is dictated by PFCCs, which communicate with the FEUs when surface is acting as a flap.

The Airplane Information Management Computers and System: Collects information from all aircraft systems including air data and inputs data into PFCCs and the displays in the flight deck.

Airplane Information Management Computers

Pilot Inputs

Flight Deck

Control Surface Feel Feedback

Control Surface Feel: Provides tactile feedback to pilot.

Primary Flight Control Computers (PFCC): These computers turn the pilot inputs into efficient commands for the flight control surfaces.

PFCC 1

PFCC 2

PFCC 3

AFDC 1

AFDC 2

AFDC 3

System Buses: The "pipelines" through which the system information travels.

1
2
3

Autopilot & Flight Director Computer (AFDC): These computers receive inputs from the attitude components and send commands to the control surfaces when autopilot is activated.

Flight Control Data Buses: These are the main "pipelines" through which the flight system information travels.

1
2
3

ACE 1

ACE 2

ACE 3

ACE 4

Actuator Control Electronics (ACE): These computers calculate which flight control surface to move in order to accomplish the task given by the PFCC (or AFDC).

Tailplane Horizontal Stabilizer Actuators

Elevator Actuators (x2 per surface)

Rudder Actuators: While only 1 actuator is needed to move the rudder in flight, there are 3 for redundancy.

Flight Control System Schematic

SY – 4.0

10 JUNE 2010

University of Southern California
Advanced Commercial Concepts

Levant

Phillip Adkins Aero Acoustics	Todd Erickson Propulsion
Darin Gaytan Aero Performance	Sina Golshany Lead Designer
Kieth Holmlund High Speed Aero	Kristina Larson Management
Devin Lewis Payload	Chris Nsavu Structures
John Roehrick Weight	Michael Zarem Systems

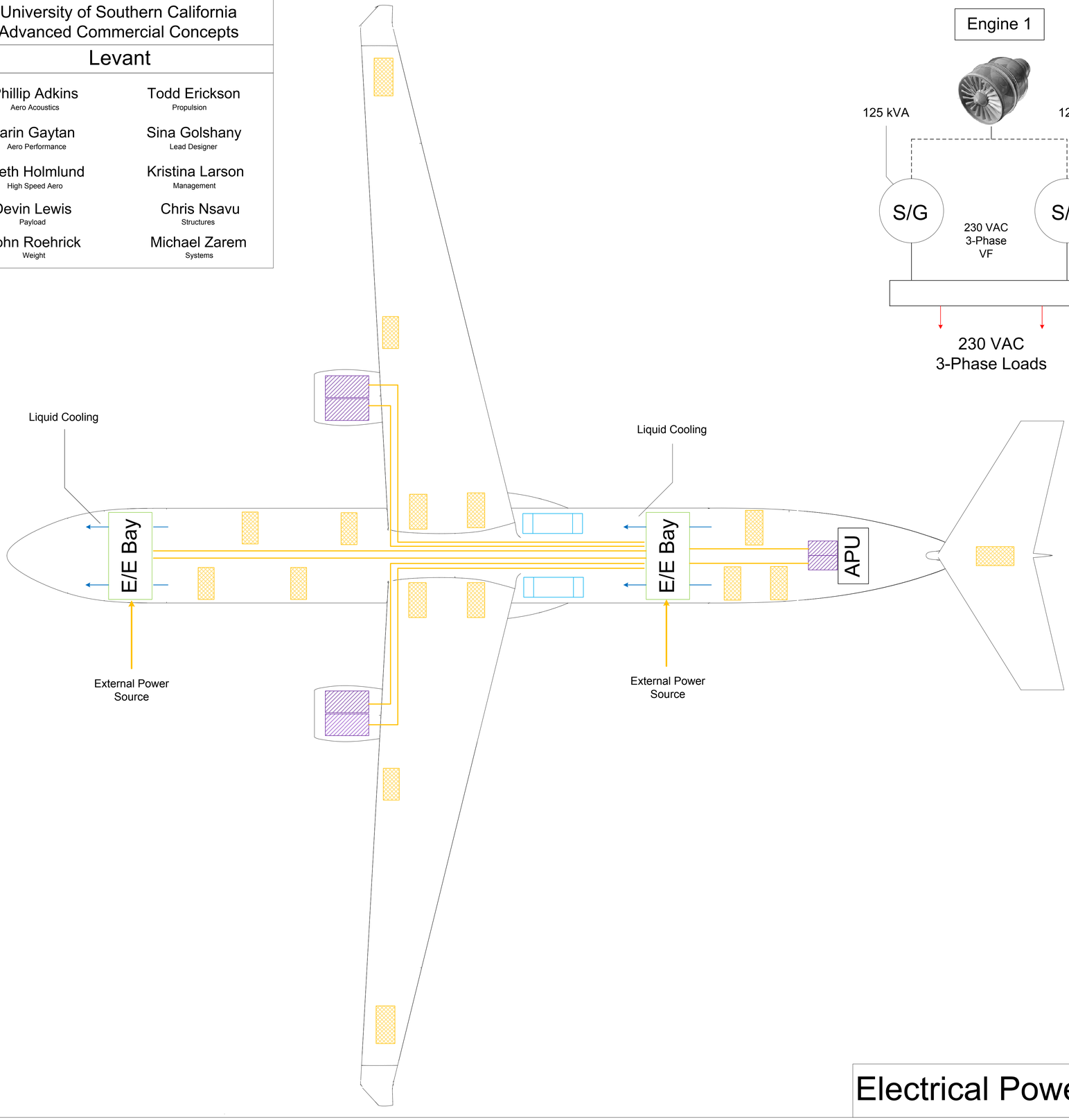

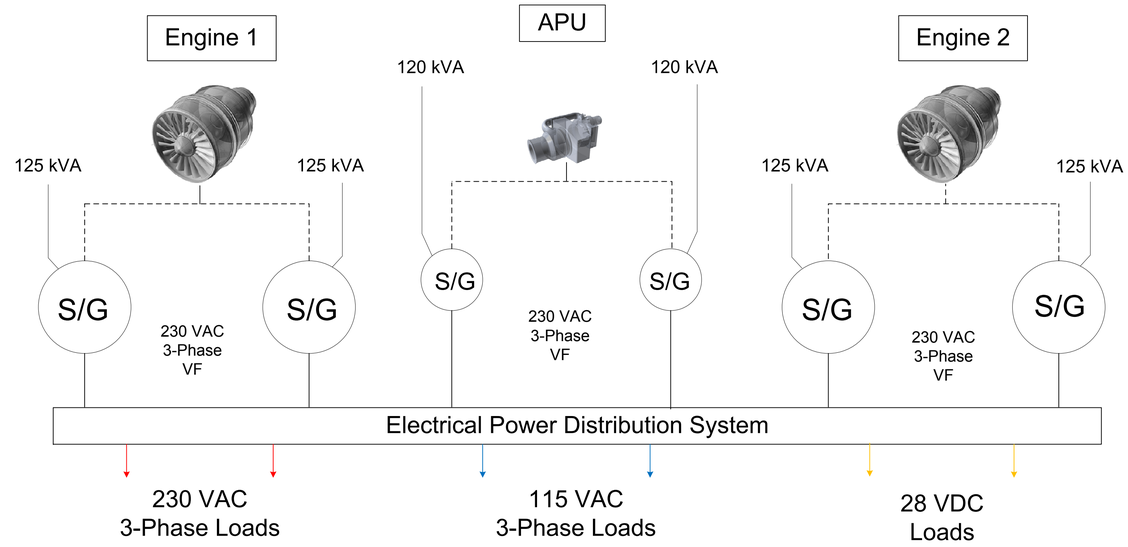

Legend:

- -- Starter/Generator
- -- Remote Power Management Unit
- APU -- Auxiliary Power Unit
- -- Environmental Control System
- E/E Bay -- Electrical/Electronics Bay
- S/G -- Starter/Generator

Electrical Power Distribution System Schematic

SY – 3.0

10 JUNE 2010

University of Southern California
Advanced Commercial Concepts

Levant

Phillip Adkins — Aero Acoustics
Todd Erickson — Propulsion
Darin Gaytan — Aero Performance
Sina Golshany — Lead Designer
Kieth Holmlund — High Speed Aero
Kristina Larson — Management
Devin Lewis — Payload
Chris Nsavu — Structures
John Roehrick — Weight
Michael Zarem — Systems

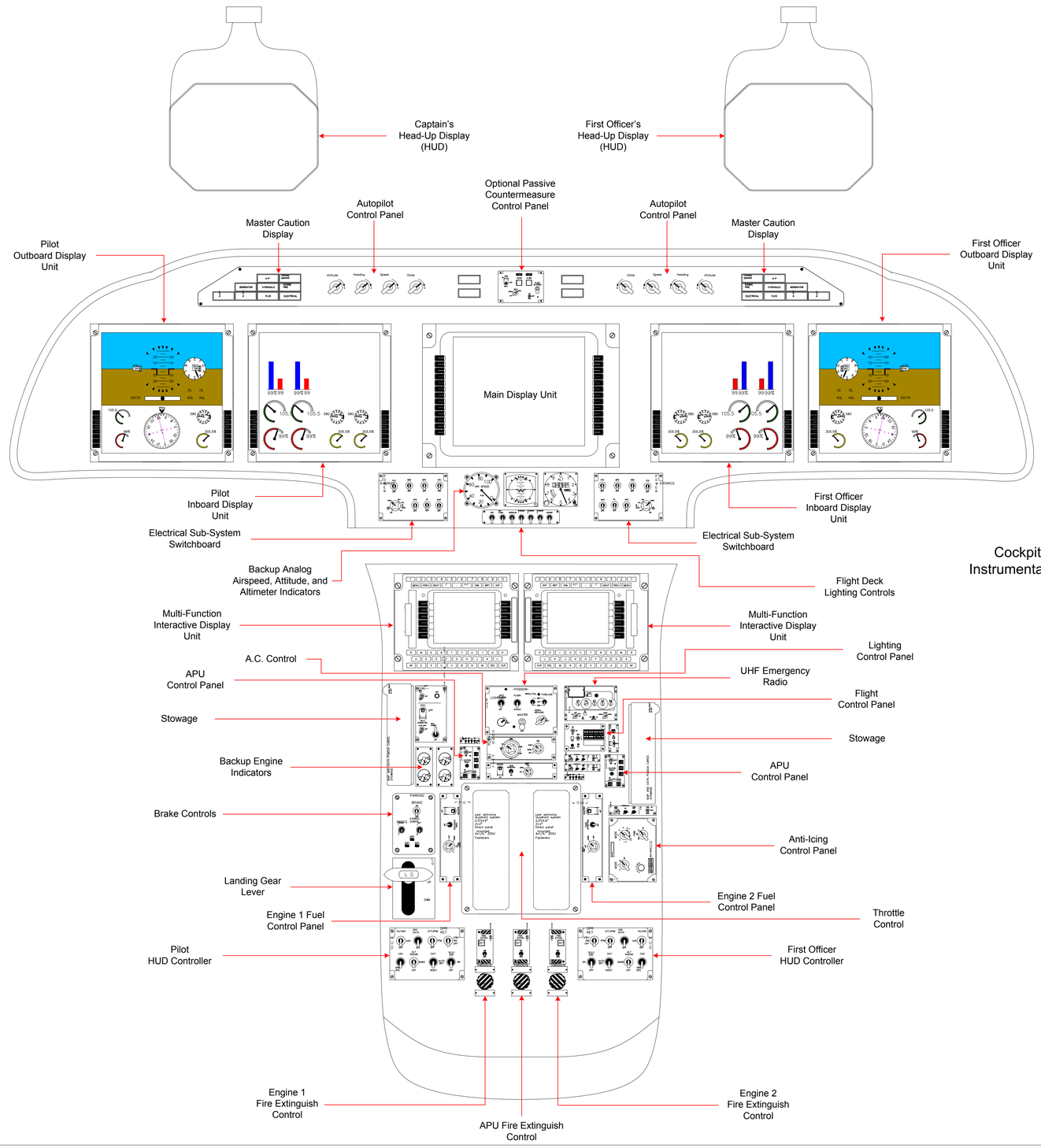

Aircraft Information Management Computer (AIMC):
Main avionics and computation tasks are performed by these computers

Data Localizing Unit (DLU):
Gather analog, digital, and serial data from remote avionics and aircraft system sensors.

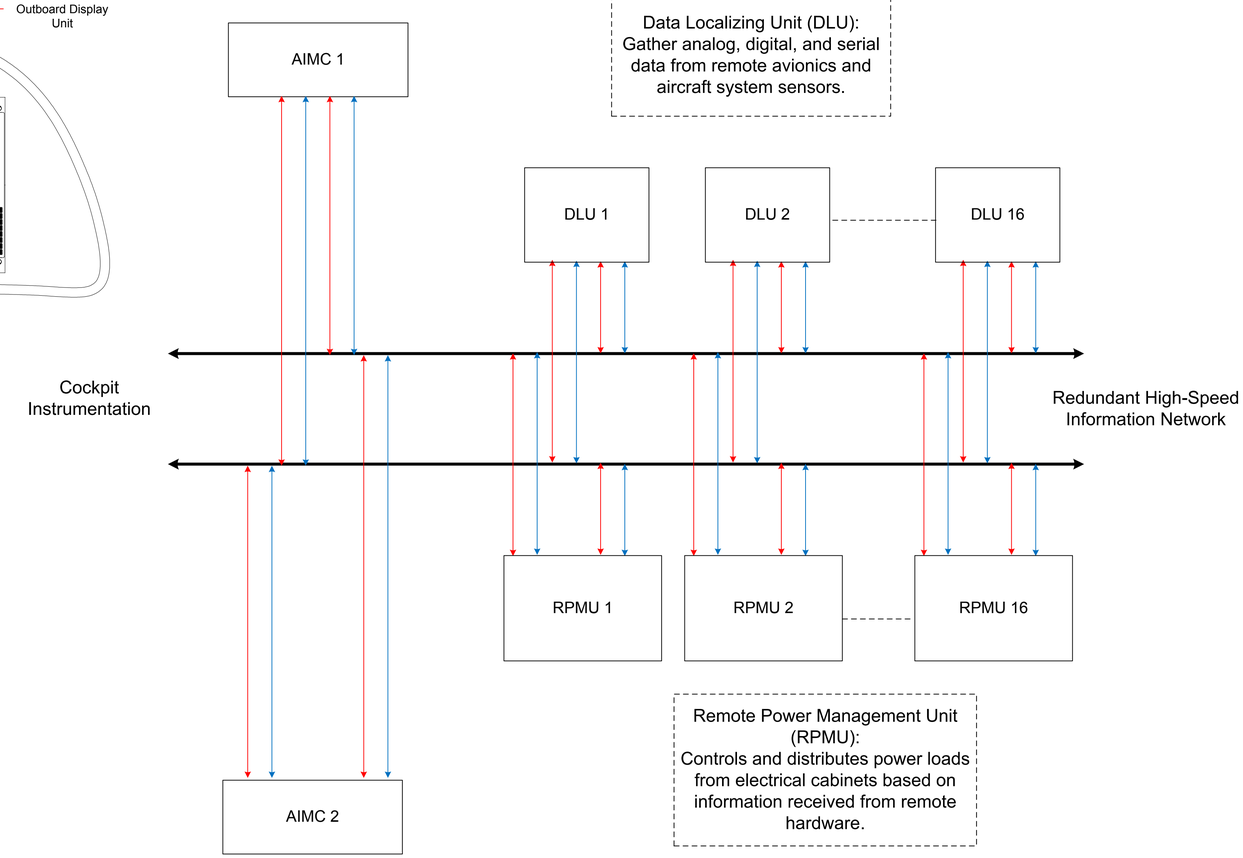

Remote Power Management Unit (RPMU):
Controls and distributes power loads from electrical cabinets based on information received from remote hardware.

Avionics System Schematic

SY – 7.0

10 JUNE 2010

University of Southern California
Advanced Commercial Concepts

Levant

Phillip Adkins — Aero Acoustics
Todd Erickson — Propulsion
Darin Gaytan — Aero Performance
Sina Golshany — Lead Designer
Kieth Holmlund — High Speed Aero
Kristina Larson — Management
Devin Lewis — Payload
Chris Nsavu — Structures
John Roehrick — Weight
Michael Zarem — Systems

Environmental Control System

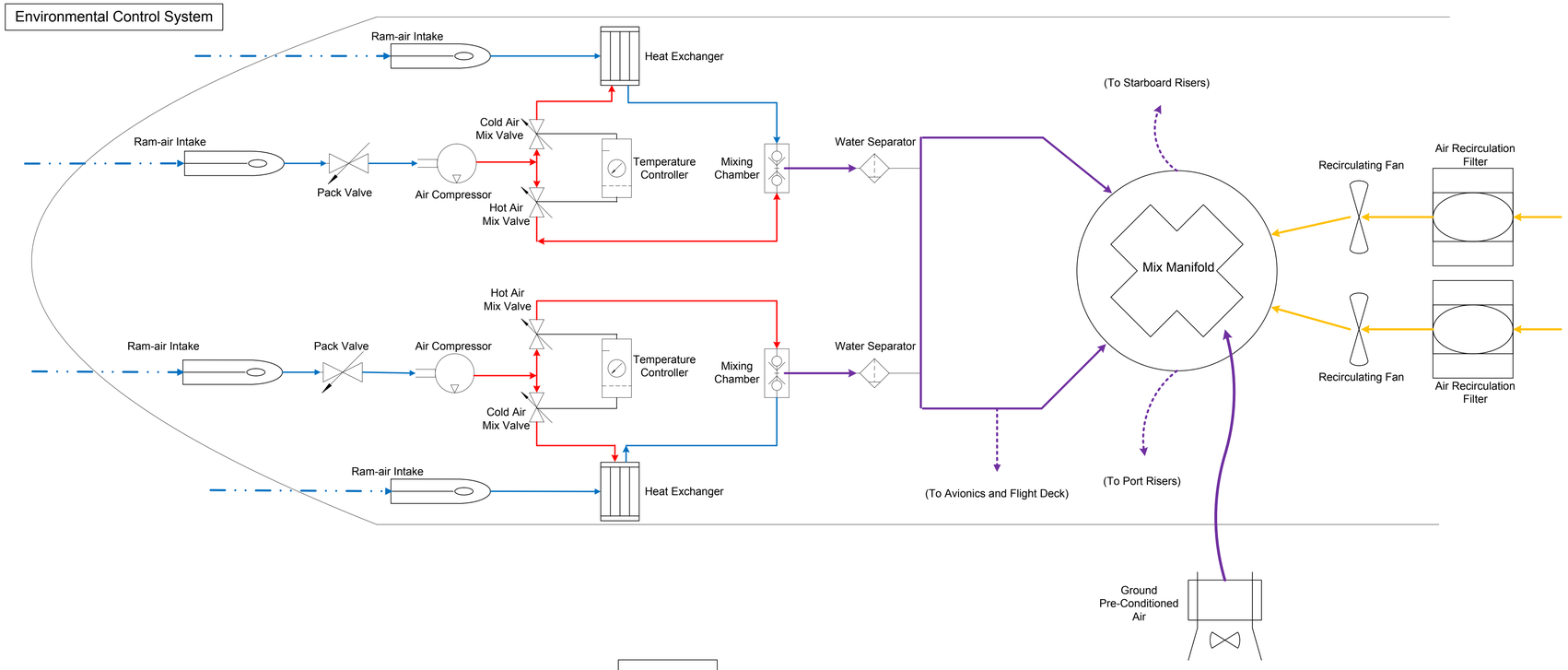

Galley and Lavatory Air Extraction

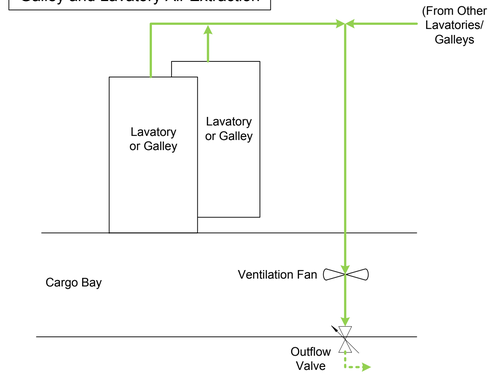

Airflow

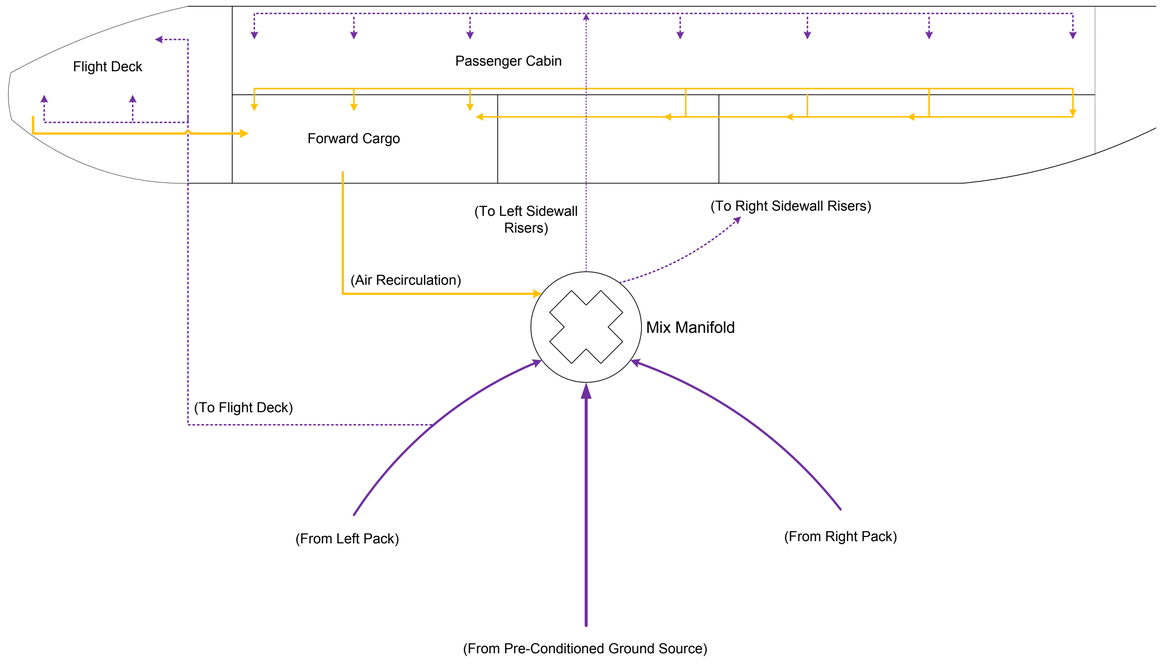

Flight Deck Equipment Cooling

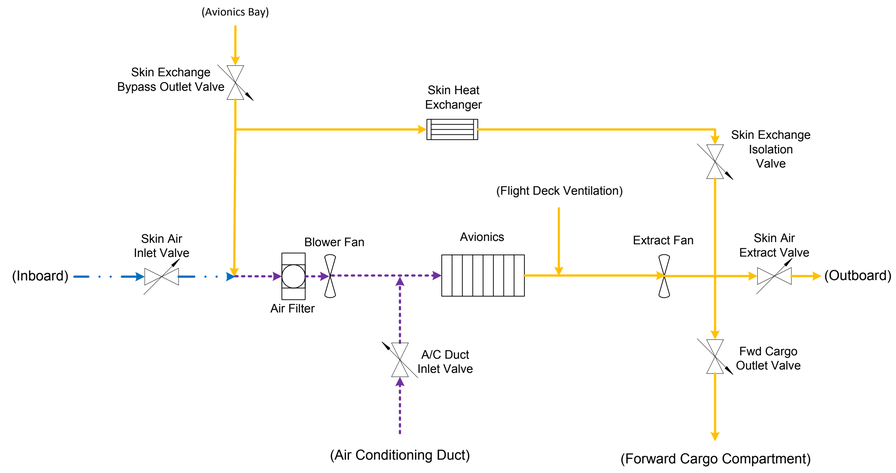

Air Conditioning System Schematic

SY – 2.0
10 JUNE 2010

University of Southern California
Advanced Commercial Concepts

Levant

Phillip Adkins Aero Acoustics	Todd Erickson Propulsion	Darin Gaytan Aero Performance	Sina Golshany Lead Designer	Kieth Holmlund High Speed Aero
Kristina Larson Management	Devin Lewis Payload	Chris Nsavu Structures	John Roehrick Weight	Michael Zarem Systems

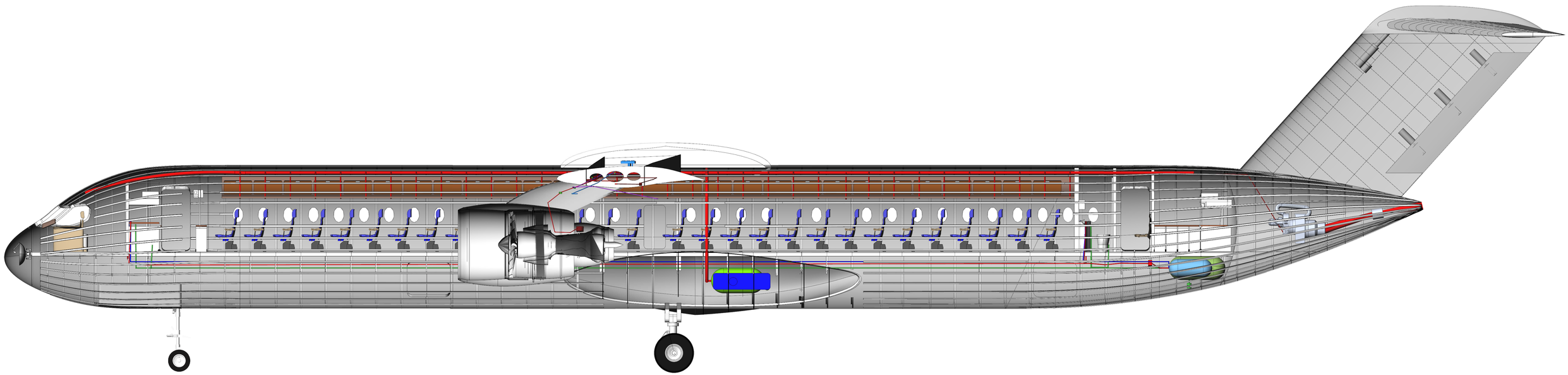

Inboard Profile

IB - 1.0

10 JUNE 2010

University of Southern California
Advanced Commercial Concepts

Levant

Phillip Adkins — Aero Acoustics
Todd Erickson — Propulsion
Darin Gaytan — Aero Performance
Sina Golshany — Lead Designer
Kieth Holmlund — High Speed Aero
Kristina Larson — Management
Devin Lewis — Payload
Chris Nsavu — Structures
John Roehrick — Weight
Michael Zarem — Systems

	Wing	Horizontal Tail	Vertical Tail
Area	1530 ft.^2	342 ft.^2	310 ft.^2
AR	14.1	3.9	1.1
Taper	0.28	0.45	1
C/4 Sweep	5.9 deg.	36 deg.	35 deg.
LE Sweep	8.1 deg.	18.7 deg.	35 deg.
Dihedral	3 deg.	-3 deg.	N/A
Root t/c	11 %	9 %	10 %
Tip t/c	9.5 %	9 %	10 %
Twist	-4 deg.	0 deg.	0 deg.

Valuesiin this table were obtained from trapizoidal simplifications and do not match the geometry shown.

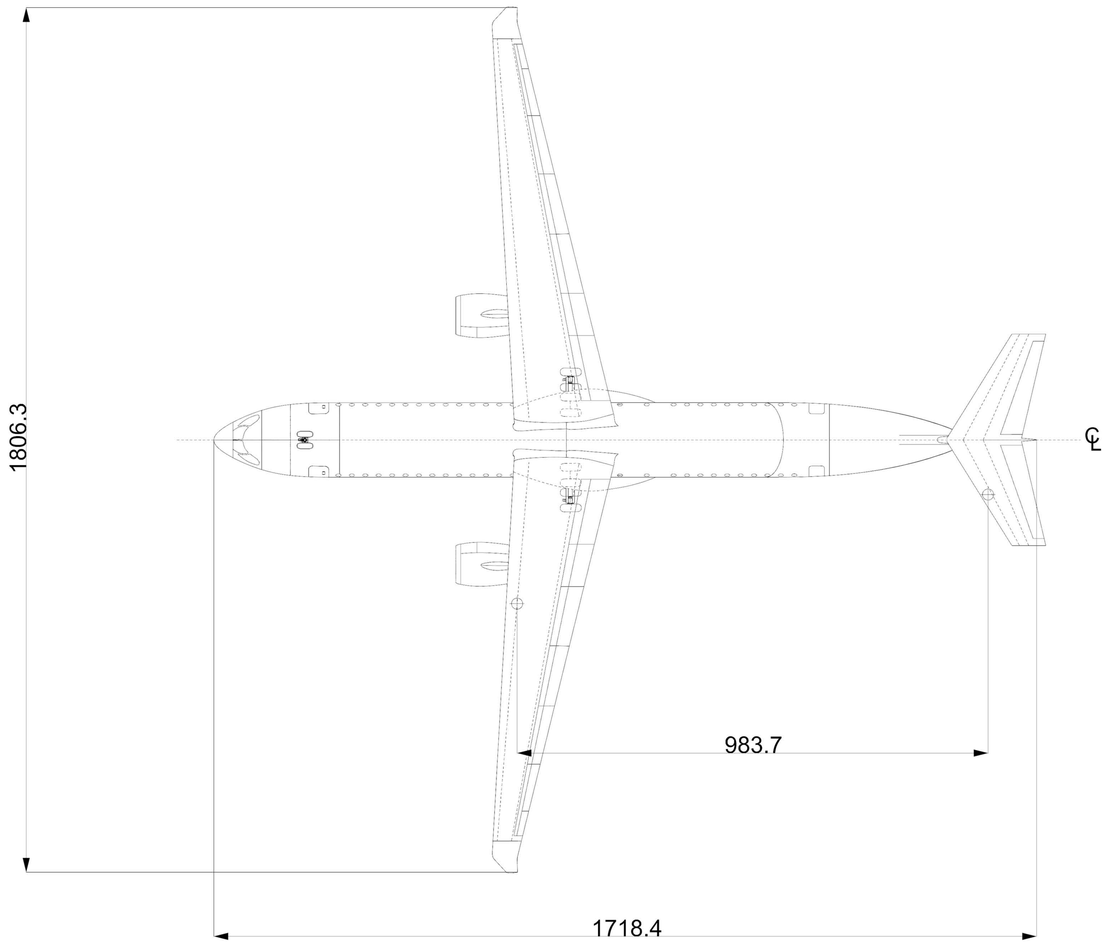

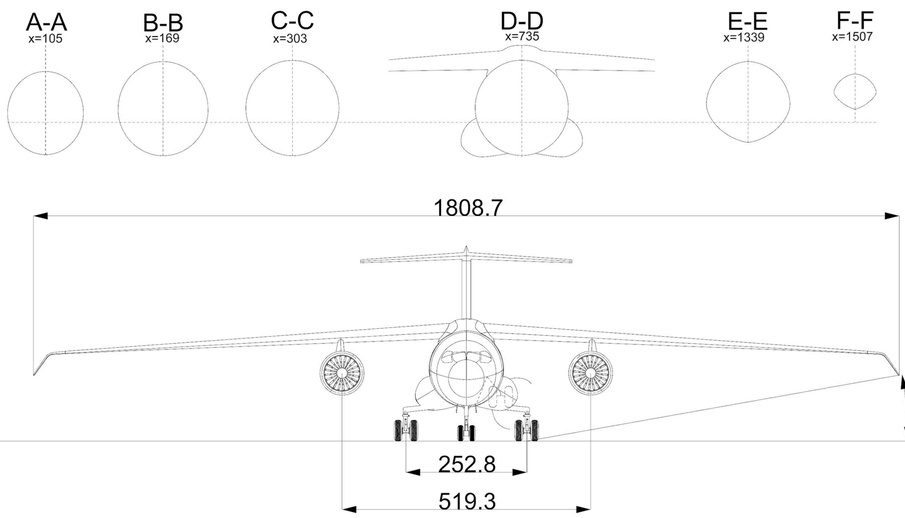

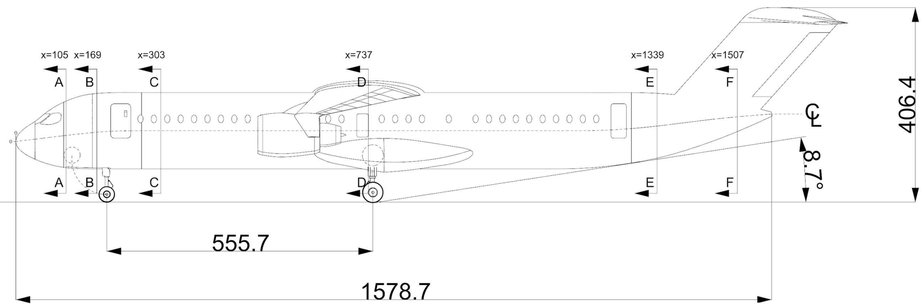

Three View

C - 1.0

10 JUNE 2010